

**Physical Study of Geobag Stability for Erosion Protection Applications in  
Rivers**

by

Kendra White

A thesis submitted in partial fulfillment of the requirements for the degree of

Master of Science

in

Water Resources Engineering

Department of Civil and Environmental Engineering

University of Alberta

© Kendra White, 2022

## Abstract

Geobags, or geotextile sand filled containers, have emerged as a cost-effective solution to providing large scale erosion protection for riverbanks and riverbeds in Bangladesh, China, and India. Geobags are currently designed using a formula intended for rock-based riprap that does not consider the flexibility and deformability of geobags. Diving explorations in the Brahmaputra River indicate that the geobags are oversized. The limited knowledge on the impact of geobag characteristics and bed configurations on the stability of geobag revetment structures in river applications provides an opportunity to improve the design formulas for geobags. In riverbed sediment studies, stability is often characterized by a critical Shields parameter. To date, there is only one study that has estimated a critical Shields parameter for geobags. Critical Shields parameters rely on critical bed shear stress estimates and are inherently statistical; more data is therefore required. Bed shear stress is challenging to measure directly, especially in complex field conditions, and therefore is often estimated indirectly. There are limited studies that evaluate the applicability of various bed shear stress estimation methods for complex flow conditions, such as flow around geobags.

This study aimed to address these knowledge gaps and improve our understanding of the stability of geobags used in river erosion protection structures. Laboratory experiments were conducted to facilitate this study. First, various bed shear stress estimation methods were compared for a single geobag placed on a rough bed. It was found that the turbulent kinetic energy method, using newly calibrated proportionality constants, provided the best estimates for bed shear stress. Second, the stability of a single geobag with varying fill ratios, bag materials and shapes were studied for both a flat and sloped bed. The results determined that fill ratio was a critical factor in geobag stability, where geobags with higher fill ratios and more flexible bag materials were most

stable. A shape factor was proposed which improves the correlation between the critical Shields parameter and boundary Reynolds number when applied to the critical Shields parameters. Third, the stability of a scaled geobag revetment structure, made up of uniform geobags, was evaluated for both a flat and sloped bed. Different geobag sizes and fill ratios were tested and critical Shields parameters were estimated for each bed configuration. The critical Shields parameters ranged between 0.09 and 0.22. Geobags with lower mass and higher fill ratios tended to be more stable than geobags with higher mass and lower fill ratios. Pre-existing design formulas were modified to include the angle of flexibility and geobag fill ratio to improve their applicability for geobags. A modified Pilarczyk formula was recommended for geobags because it includes a critical Shields parameter and provides more reasonable bag sizes for extremely large flow depths, compared to the modified U.S. Army Corps of Engineers formula.

## Preface

Chapter 2 is taken from White, K.; She, Y.; Zhang, W., Submitted for publishing in the Journal of Geotextiles and Geomembranes. A Comparison of Shear Stress Estimation Methods for a Single Geobag on Rough Bed.

Chapter 3 is to be submitted for publication: White, K.; She, Y.; Zhang, W., Characterization of a Single Geobag on a Rough Bed: A Study on Incipient Motion.

Chapter 4 is to be submitted for publication: White, K.; She, Y.; Zhang, W., Evaluation of Geobag Design Formulas and Stability for Erosion Protection Structures in Rivers: Physical Model Study.

All work presented in this thesis is my own work.

## Acknowledgements

I would like to thank my supervisors Dr. She and Dr. Zhang for their constant guidance throughout my research work. I am grateful for their support and flexibility during the dynamic times of the pandemic. I would also like to thank Angela Thompson, Knut Oberhagemann and Ken Christison for their feedback and support. I appreciate them answering my questions and ensuring that I had the materials to perform my experiments. I am grateful to Northwest Hydraulic Consultants Ltd for providing financial and technical support, as well as the laboratory space and equipment. I would also like to extend my gratitude to the Natural Sciences and Engineering Research Council of Canada for providing financial support for this research. I extend my gratitude to Perry Fedun for constructing experiment apparatus and ensuring I had the laboratory instrumentation and equipment to perform my experiments. Finally, I would like to thank my family for their love and support throughout my graduate studies.

# Table of Contents

List of Symbols .....	xiii
1 Introduction.....	1
1.1 Geobags for River Erosion Protection Applications .....	1
1.2 Geobags in Revetment Structures in Bangladesh .....	2
1.3 Geobag Design Methodologies .....	5
1.4 Knowledge Gaps .....	8
1.5 Objectives.....	10
2 A Comparison of Shear Stress Estimation Methods for a Single Geobag on a Rough Bed. 11	
2.1 Introduction .....	11
2.1.1 Literature Review.....	12
2.1.1.1 Energy Grade Line (EGL) Method.....	12
2.1.1.2 Method of Universal Law of the Wall.....	13
2.1.1.3 Preston and Patel Methods .....	14
2.1.1.4 Reynolds Stress Method .....	15
2.1.1.5 Turbulent Kinetic Energy (TKE) Method .....	16
2.1.1.6 Other Methods .....	17
2.1.1.7 Comparisons among Methods .....	17
2.2 Methodology .....	18
2.3 Results and Discussion.....	23
2.3.1 TKE Proportionality Constants.....	23
2.3.2 Method Comparison - Smooth Bed Shear Stress.....	27
2.3.3 Method Comparison - Rough Bed Shear Stress .....	28
2.3.4 Method Comparison - Dimensionless Rough Bed Shear Stress .....	31
2.3.5 Sources of Errors.....	36
2.4 Conclusions .....	37
2.5 References .....	39
3 Effects of Bag Characteristics on Incipient Motion of a Single Geobag.....	43
3.1 Introduction .....	43
3.2 Methodology .....	47
3.2.1 Experimental Set-Up.....	47
3.2.2 Geobag Characteristics .....	48

3.2.3	Experimental Procedure.....	51
3.3	Results .....	55
3.3.1	Incipient Motion.....	55
3.3.2	Critical Bed Shear Stresses .....	57
3.3.3	Contour Analysis .....	58
3.3.4	Critical Shields Parameter.....	60
3.4	Discussion .....	62
3.4.1	Fill Ratio .....	62
3.4.2	Bag Material.....	63
3.4.3	Geobag Shapes.....	66
3.4.4	Bed Configuration.....	68
3.4.5	Shape Factor of Geobag.....	69
3.5	Conclusion.....	74
3.6	References .....	76
4	Evaluation of Geobag Design Formulas and Stability for Erosion Protection Structures in Rivers: Physical Model Study.....	79
4.1	Introduction .....	79
4.2	Methodology .....	85
4.2.1	Geobag Characteristics .....	85
4.2.2	Experimental Set-Up.....	87
4.2.3	Experiment Procedure.....	89
4.3	Results and Discussion.....	92
4.3.1	Incipient Motion.....	92
4.3.2	Critical Shields Parameter.....	100
4.3.3	USACE Design Formula.....	106
4.3.4	Pilarczyk Design Formula.....	109
4.3.5	Applications in the Brahmaputra River .....	111
4.4	Conclusion.....	115
4.5	References .....	117
5	Conclusions and Future Research.....	120
	References.....	125

## List of Tables

Table 1-1: Geobag Element Projects .....	4
Table 2-1: Summary of experimental conditions.....	19
Table 2-2: Summary of the estimated proportionality constants, $C_1$ and $C_2$ , for TKE and TKE $w'$ methods .....	24
Table 2-3: Summary of the results of the local bed shear stress estimation methods .....	39
Table 3-1: Summary of characteristics of the six geobags studied.....	51
Table 3-2: Summary of single bag experiment series for the flat bed .....	54
Table 3-3: Summary of single bag experiment series for 1V:2H slope bed.....	54
Table 4-1: Summary of geobags used in the experiments.....	85
Table 4-2: Summary of experiment series .....	86
Table 4-3: Velocity set-points for each experiment series.....	90
Table 4-4: Summary of critical Shields parameters for all bags from the flat bed experiments. The dash (–) means that no test was performed.....	101
Table 4-5: Summary of critical Shields parameters for all bags from the 1V:2H bed experiments. The dash (–) means that no test was performed.....	101
Table 4-6: Application of design formulas to a prototype 125 kg geobag. ....	112
Table 4-7: Summary of recommended design formulas, observed critical velocities and design velocities for the prototype scale .....	115

## List of Figures

Figure 1-1: Map of the Brahmaputra and Meghna catchment basins (GISGeography 2022) .....	2
Figure 1-2: Schematic of geobag revetment structure (Oberhagemann and Hossain 2011) .....	3
Figure 2-1: Experimental set-up and measurement locations for the single geobag tests, in (a-c) side view and (d) plan view. In (a), the measurement heights correspond to the distance above the bag; (b) shows the cement-filled bag used in Series 2 – 4, and (c) shows the sand-filled bag in Series 7.....	20
Figure 2-2: Comparison between time-averaged velocity data collected from the Pitot-Tube and ADV.....	22
Figure 2-3: Comparison of the shear stress estimated from the TKE methods and the Reynolds stress, at all measurement heights from the bed in Series 2, 3 and 4, employing proportionality constants $C_1 = 0.19$ and $C_2 = 0.90$ in (a), (c) and (e), and the proportionality constants $C_1 = 0.30$ and $C_2 = 1.60$ in (b), (d) and (f). .....	26
Figure 2-4: Shear stress estimations from each method on the smooth bed with (a) $Fr = 0.29$ , and (b) $Fr = 0.44$ . .....	27
Figure 2-5: Contour plots for Series 2 on the rough bed, including (a) bed topography, and the local bed shear stress estimated by (b) Reynolds stress method via extrapolation, (c) TKE method, (d) TKE $w'$ method, (e) universal law of the wall method, and (f) the Patel method. ...	30
Figure 2-6: Contour plots of the streamwise (a) turbulence intensity, (b) velocity distribution for Series 2.....	31
Figure 2-7: Comparison of dimensionless shear stress values for the cement-filled geobag at all Froude numbers (series 2, 3, 4), employing the a) universal law of the wall, b) extrapolated Reynold's stress, c) single near-bed point Reynold's stress, d) TKE, e) TKE $w'$ , and f) Patel methods. ....	32
Figure 2-8: Comparison of dimensionless shear stress values for the sand-filled geobag at all Froude numbers (series 5, 6, 7), employing the a) universal law of the wall, b) extrapolated Reynold's stress, c) single near-bed point Reynold's stress, d) TKE, e) TKE $w'$ , and f) Patel methods. ....	33
Figure 3-1: Schematic of the (a) sideview of the flat-bed configuration, (b) the cross-sectional view of the 1V:2H slope-bed configuration, and (c) the plan view of the measurement locations. Flow is going into the page for the cross-section view in (b). .....	48

Figure 3-2: Comparison of the dimensionless angle of flexibility and mass between scaled and prototype geobags. The points circled in red correspond to the geobags used in this study, all other points are from Thompson et al. (2020a) and NHC (2010).....	50
Figure 3-3: Relationship between the dimensionless angle of flexibility and the fill ratio. ....	50
Figure 3-4: Comparison of the average failure velocity for each series. ....	56
Figure 3-5: Summary of the local critical bed shear stresses estimated at measurement location (a) B-M, (b) C-M, and (c) D-M, for all experiment series.....	58
Figure 3-6: Contours of the local bed shear stress and near-bed streamwise velocity for (a-b) Series 5b (flat bed, even initial shape), and (c-d) Series 11b (1V:2H sloped bed, even initial shape), at an average flow velocity of 0.50 m/s. The square points represent the measurement locations, and the rectangle represents the geobag. ....	60
Figure 3-7: Relationship between the critical Shields parameter and boundary Reynolds number for all series. The dashed line represents the line of best fit ( $y = x^2$ ), and the two solid lines represent the upper and lower bounds ( $\pm 30\%$ ). ....	62
Figure 3-8: Sideview photos of geotextile geobags at their highest velocity set-points before failure for flat bed configurations (a, c, e) and 1V:2H slope bed configurations (b, d, f), for (a) Series 3a (G3 upstream heavy), (b) Series 9a (G3, upstream heavy), (c) Series 3b (G3 even), (d) Series 9b (G3 even), (e) Series 2c (G2 downstream heavy), (f) Series 8c (G2 downstream heavy). Flow is from left to right. ....	64
Figure 3-9: Sideview photos of cloth geobags at their highest velocity set points before failure for flat bed configurations (a, c, e) and 1V:2H slope bed configurations (b, d, f), for (a) Series 5a (C2, upstream heavy), (b) Series 11a (C2, upstream heavy), (c) Series 6b (C3, even), (d) Series 12b (C3, even), (e) Series 5c (C2, downstream heavy), (f) Series 11c (C2, downstream heavy), and at velocity set point 0.50 m/s for (g) Series 5b and (h) Series 11b. Flow is from left to right. ....	65
Figure 3-10: Geobag shape change between the last two velocity set-points for Series 6a (C3, upstream heavy) at (a) velocity set point of 0.87 m/s, (b) velocity set point of 0.97 m/s.....	67
Figure 3-11: Rectangular prism containing an irregularly shaped object, i.e., a geobag.....	70
Figure 3-12: Relationship between the critical depth-averaged velocity with the shape factor, <i>SFG</i> , for all experiment series. ....	71

Figure 3-13: Relationship between the critical depth-averaged velocity with the shape factor, slope factor and relative depth, for all experiment series. ....	72
Figure 3-14: Relationship between critical Shields parameter and boundary Reynolds number, with an applied shape factor. The dashed line represents the line of best fit ( $y = x^2$ ). ....	74
Figure 4-1: Comparison of the dimensionless angle of flexibility and mass between scaled and prototype geobags. The points circled in red correspond to the geobags used in this study. ....	86
Figure 4-2: Schematic of experimental set-up of (a) sideview of the flat bed, (b) cross-sectional view of the 1V:2H sloped bed. ....	89
Figure 4-3: Cumulative percentage of failed bags from each series.....	93
Figure 4-4: Photos of the test-section before and after velocity set-point 1.51 m/s (prototype velocity 4.0 m/s) and the corresponding contours of the differential bed elevations, $z$ , for (a) Series 5 and (b) Series 1. Circled geobags in (b) represent geobags which shifted in place yet did not fail. ....	96
Figure 4-5: Contours of the differential bed elevations, $z$ , between two velocity set-points (a) 1.70 m/s and 1.89 m/s for Series 4, (b) 1.13 m/s and 1.32 m/s for Series 10, and their corresponding orthographic projection photos. Geobags that moved are circled in red. ....	98
Figure 4-6: Comparison of incipient motion between this study and Thompson et al. (2020a) for (a) geobag B with a 66% fill ratio (250 kg prototype size), and (b) geobag A with an 84% fill ratio (125 kg prototype size). ....	100
Figure 4-7: Shield parameters of the stable and unstable conditions for (a) flat bed series, and (b) 1V:2H series.....	102
Figure 4-8: Comparison of Shields parameters between this study and the results from Thompson et al. (2020b) for the flat bed configuration. ....	104
Figure 4-9: Relationship between Shields parameter, corrected for the shape factor, with the boundary Reynolds number for unstable conditions. ....	105
Figure 4-10: Relationship between critical Shields parameter, corrected with a modified shape factor ( $SFG = FR3.3\phi2.6$ ), and the boundary Reynolds number for unstable conditions. ....	106
Figure 4-11: Application of the (a) original USACE formula, and (b) modified USACE formula with for the flat bed case.....	108
Figure 4-12: Application of the (a) original USACE formula, and (b) modified USACE formula with for the 1V:2H slope bed case.....	109

Figure 4-13: Application of the Pilarczyk formula on the results from this study, with a Shields parameter of 0.09. The slope of fitted line is the inverse of the Shields parameter..... 110

Figure 4-14: Application of the modified Pilarczyk formula on the results from this study, with a Shields parameter of 0.10. .... 111

## List of Symbols

Symbol	Description [units]
$a$	= width of rectangular prism [m]
$b$	= height of rectangular prism [m]
$B$	= channel width [m]
$c$	= length of rectangular prism [m]
$C_1$	= proportionality constant for TKE method [dimensionless]
$C_2$	= proportionality constant for TKE $w'$ method [dimensionless]
$C_S$	= stability coefficient [dimensionless]
$C_T$	= thickness coefficient [dimensionless]
$C_V$	= vertical velocity distribution coefficient [dimensionless]
$d$	= external diameter of Pitot-Tube [m]
$D$	= characteristic diameter [m]
$D_{30}$	= rock diameter, by which 30% is finer [m]
$D_k$	= effective diameter [m]
$d_n$	= characteristic diameter, taken as the cube root of the particle's volume [m]
$f_w$	= friction factor of the sidewall [dimensionless]
$g$	= acceleration of gravity [ $\text{m/s}^2$ ]
$h$	= flow depth [m]
$k$	= von Karman constant [dimensionless]
$K_h$	= depth parameter [dimensionless]
$K_s$	= slope factor [dimensionless]
$K_T$	= turbulence factor [dimensionless]
$m^*$	= dimensionless mass [dimensionless]
$\phi$	= dimensionless angle of flexibility [dimensionless]
$\varphi$	= stability parameter [dimensionless]
$\theta$	= angle of revetment slope to the horizontal [degrees]
$\vartheta$	= angle of repose of the element [degrees]
$\rho$	= fluid density [ $\text{kg/m}^3$ ]
$\rho_s$	= density of particle or element [ $\text{kg/m}^3$ ]

---

$\Delta p_p$	= dynamic pressure [Pa]
$R$	= hydraulic radius [m]
$R_b$	= hydraulic radius of the bed [m]
$R_w$	= hydraulic radius of the sidewall [m]
$Re$	= Reynolds number [dimensionless]
$S_f$	= water surface slope [%]
$\tau_b$	= local bed shear stress [Pa]
$\bar{\tau}_b$	= average bed shear stress [Pa]
$\overline{\tau}_{b,R}$	= averaged bed shear stress over a rough channel [Pa]
$\overline{\tau}_{b,S}$	= average bed shear stress over a smooth channel [Pa]
$\tau_{cr}$	= critical bed shear stress [Pa]
$\tau_o$	= total shear stress [Pa]
$u$	= velocity in streamwise direction, measured at some distance from the bed [m/s]
$U$	= depth-averaged velocity [m/s]
$u^*$	= local bed shear velocity [m/s]
$u_{cr}^*$	= critical shear velocity [m/s]
$u'$	= velocity fluctuation in streamwise direction [m/s]
$\nu$	= kinematic viscosity [m <sup>2</sup> /s]
$V$	= average flow velocity [m/s]
$v'$	= velocity fluctuation in transverse direction [m/s]
$\forall$	= volume [m <sup>3</sup> ]
$w'$	= velocity fluctuation in vertical direction [m/s]
$\gamma$	= specific weight of water [N/m <sup>3</sup> ]
$\psi$	= Shields parameter [dimensionless]
$z$	= measured height from the bed [m]
$z_o$	= roughness height [m]

---

# 1 Introduction

## 1.1 Geobags for River Erosion Protection Applications

Significant river erosion can pose a threat to infrastructure, human life, and economic development, prompting many locations around the World to construct river erosion protection structures. River erosion protection structures can be built using various materials including riprap, cement blocks, and geobags. Geobags, or geotextile containers filled with sand, have recently emerged as a cost-efficient and effective protection element for applications in erosion protection or revetment structures in rivers. They have successfully been employed in revetment structures along the Brahmaputra River in Bangladesh and India, and the Changjiang/Yangtze River in China (Oberhagemann and Hossain 2011; Thompson et al. 2020a; Zhu et al. 2004; Yang et al. 2008). Geobags were selected as the primary construction element in these rivers for the following reasons: they are relatively low-cost, materials are easily accessible, and they provide effective, long-term protection.

Yang et al. (2008) evaluated different dike constructions for a dike failure in the Yangtze River in 1996. They found that only dikes built without geobags resulted in failure. Zhu et al. (2004) researched the settling distance of geobags in the installation phase in the Changjiang River, where geobags are dropped off barges into the deep river to form the revetment structure. Their results showed that 60% of geobags settled with the long side parallel to flow and that settling distance could be described with a log-normal function. The method of dropping geobags off barges has been suggested to result in better stability compared to placing the geobags (Thompson et al. 2020a). Geobags have also been explored as primary elements for scour protection for bridge abutments in the United States (Korkut et al. 2007). Korkut et al. (2007) evaluated construction criteria for effective scour prevention and recommended placing geobags below bed level for optimal protection.

## 1.2 Geobags in Revetment Structures in Bangladesh

Every year, up to two-thirds of Bangladesh is flooded by the Jamuna (lower-Brahmaputra) and Meghna catchment basins which consist of four major rivers: the Brahmaputra, Ganges, Padma and Meghna rivers (ADB 2020). This inundation is exacerbated by climate-change and severe weather events, which negatively impact riverbank and bed stability. In some locations along the rivers, lateral riverbank erosion rates can reach 1 km per year and vertical scour depths can exceed 70 m. The continued loss of land impacts the economic development of Bangladesh, keeps residents in poverty, while putting them at risk for displacement. To address these issues, projects have been implemented to improve the riverbank stability through the construction of erosion protection structures. (Oberhagemann and Hossain 2011; ADB 2020)

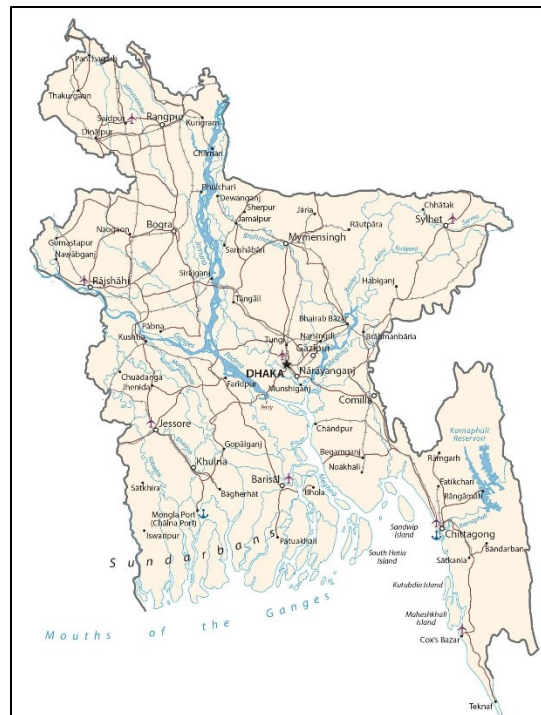


Figure 1-1: Map of the Brahmaputra and Meghna catchment basins (GISGeography 2022)

The erosion protection structures, or revetment structures, are primarily constructed using geobags. Geobags are geotextile bags filled with dredged sand sourced directly from the river

delta. Typically, rock-based riprap is used in fluvial erosion protection structures; however, sources are lacking in the region and transportation of quarried rock would significantly increase the costs of such projects. Cement-blocks have been used as an alternative material in Bangladesh, though this material is costly and unsuitable for emergency protection as it takes time to manufacture (Oberhagemann and Hossain 2011).

To consider the rivers' rapidly changing morphology, geobag revetment structures are constructed in a phased approach. Initially, geobags are dumped along the shoreline and shallow section of the riverbank in a massive heap, which self-launches into deeper water. This 'falling apron' enables better protection against toe scouring and typically launches to a geotechnically stable slope of 1V:2H (V = vertical, H = horizontal). The falling apron is a key component to the geobag revetment structure design as sections of the rivers are too deep to allow for direct placement of the geobags. Additional layers of geobags are dumped from a barge in subsequently deeper sections to ensure long term protection. A schematic of a typical geobag revetment structure, as constructed using the phased approach, is shown in Figure 1-2.

(Oberhagemann and Hossain 2011)

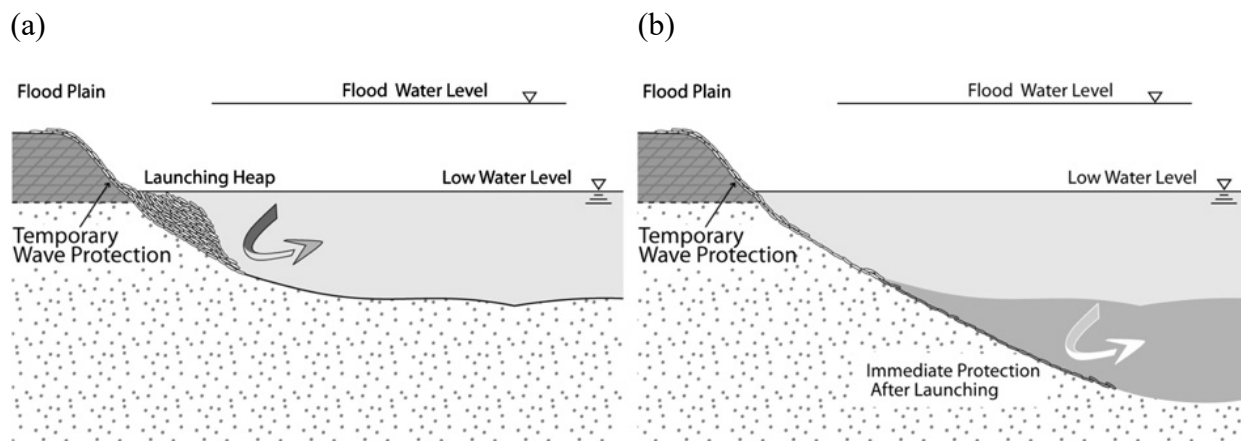


Figure 1-2: Schematic of the geobag revetment structure phased approach construction method: (a) initial mass geobag dump on the shoreline, and (b) post self-launch of the geobag heap. (Oberhagemann and Hossain 2011)

Geobag revetments constructed in Bangladesh and neighboring Assam, India, consist of various geobag sizes, depending on the design methodology and river hydraulic loading. In 2002, at the Meghna-Padma confluence, four different sizes of geobags were used in a graded manner which resulted in variable thickness and coverage. The two smaller geobag sizes, weighing 11 kg and 36 kg respectively, were unstable at hydraulic loads caused by the river's current. To simplify the construction process and ensure consistent surface area coverage and revetment stability, it was recommended to use one geobag size for the structure that weighed 78 kg or larger; however, up to two sizes may be used concurrently. Common sizes are categorized by mass and detailed in Table 1-1 (Oberhagemann and Hossain 2011).

The size of the geobag elements is selected to ensure a stable revetment structure against the maximum hydraulic loading at the relevant location. In the Dibrugarh, Palasbari project in Assam, India, the 125 kg sized geobag was selected as the primary element for a hydraulic loading corresponding to a maximum current velocity of 3 m/s (ADB 2009). The Padma Bridge project employed the 800 kg sized geobags as the primary element for the revetment structure, for a maximum velocity of 5.1 m/s (ADB 2010). This project also used 126 kg sized geobags as a filter element (ADB 2020). In more recent projects along the lower Jamuna and upper Padma reaches, both 126 kg and 250 kg sized geobags have been used (ADB 2014).

Table 1-1: Geobag Element Projects

Geobag Mass	Geobag Length x Width	Relevant Projects
78 kg	0.83 m x 0.60 m	Meghna-Padma Confluence, 2002 (ADB 2002)
126 kg	1.03 m x 0.70 m	Meghna-Padma Confluence, 2002 (ADB 2002) Padma Bridge, 2010 (ADB 2020) Dibrugarh, Palasbari, 2011 (ADB 2010) Lower Jamuna, Upper Padma, 2017 (ADB 2014)
250 kg	1.25 m x 1.00 m	Lower Jamuna, Upper Padma, 2017 (ADB 2014)
800 kg	2.10 m x 1.50 m	Padma Bridge, 2010 (ADB 2020)

### 1.3 Geobag Design Methodologies

Diving explorations of revetment structures in the Brahmaputra River suggest that geobags may be oversized for the subjected hydraulic loading (Oberhagemann and Hossain 2011). Optimizing the size of the geobag elements would not only reduce costs for materials, but also improve the efficiency of the labor-intensive construction, as larger sized geobags take longer to fill and move. As the need for geobag revetment structures is growing, there is motivation to refine the hydraulic design of geobag erosion protection structures.

Methods of sizing geobag elements require information on the conditions at which geobags become unstable and undergo incipient motion. Incipient motion is broadly defined as the point when the element begins to move (Shields 1936), or when the acting lift, drag and inertia forces exceed the contact, submerged weight, and cohesion forces of the element (Pilarczyk 1991).

Shields (1936) defined a dimensionless parameter, named the Shields parameter, to characterize the inherently statistical incipient motion of sediment based on a critical bed shear stress. Shields (1936) demonstrated that in rough, turbulent flows (Reynolds number  $> 1000$ ), the critical Shield's parameter is constant. Knowledge of this threshold parameter may be useful in sizing elements for revetment structures, as bed shear stresses more accurately describe the forces acting on the bed. However, there is limited data on critical bed shear stresses and Shields parameters for geobag elements. Therefore, current design methodologies typically rely on a critical depth-averaged velocity which is a notably less accurate indicator of incipient motion.

The U.S. Army Corps of Engineers (USACE) developed a design formula (see Eq. 1-1) using Maynard's data (Maynard 1988) for erosion protection structures built with rock-based riprap (USACE 1994).

$$D_{30} = S_F C_S C_V C_T y \left[ \left( \frac{\rho_w}{\rho_s - \rho_w} \right)^{0.5} \left( \frac{V_{cr}}{\sqrt{K_s g y}} \right) \right]^{2.5} \quad \text{Eq. 1-1}$$

Where,  $D_{30}$  is the rock size by which 30% is finer by weight [m],  $S_F$  is a safety factor,  $C_S$  is a stability coefficient,  $C_V$  is the vertical velocity distribution coefficient,  $C_T$  is the thickness coefficient,  $y$  is the flow depth [m],  $\rho_w$  is the density of water [kg/m<sup>3</sup>],  $\rho_s$  is the density of the sediment or element [kg/m<sup>3</sup>],  $g$  is the acceleration due to gravity [m/s<sup>2</sup>],  $V_{cr}$  is the depth-averaged velocity at incipient motion [m/s], and  $K_s$  is the side slope correction factor ( $= \sqrt{1 - \left( \frac{\sin^2 \theta}{\sin^2 \vartheta} \right)}$ ); where,  $\theta$  is the angle of the slope to the horizontal, and  $\vartheta$  is the angle of repose of the elements which is typically between 30° and 40° for sand-filled systems (Pilarczyk 1991)).

The USACE formula employs the depth-averaged velocity at which elements undergo incipient motion to estimate the appropriate size and gradation for the structure. The size of elements is sensitive to the depth-averaged velocity, where a 10% change in velocity results in a 30% change in size and almost 100% change in gradation (USACE 1994). Although the USACE formula is based on experimental data for rocks, it has also been considered for geobag applications (Neill et al. 2008; NHC 2010; Thompson et al. 2020a). The 250 kg geobags used in the lower-Jamuna have been sized using a modified USACE formula (Bangladesh Water Development Board 2010). Limitations to this design methodology include: its inability to account for the flexibility and deformability of geobags; the assumption that equal depth-averaged velocities at different locations experience the same bed shear stresses; and the relationship between design size and flow depth which results in unreasonably small design sizes for sections of the Brahmaputra River where the flow depth is extremely deep (~70 m).

An alternative design formula was proposed by Pilarczyk (1990) and presented by Bezuijen and Vastenburger (2013):

$$\left(\frac{\rho_s - \rho_w}{\rho_w}\right) D_k \geq 0.035 \frac{\varphi K_T K_h V_{cr}^2}{\psi K_S 2g} \quad \text{Eq. 1-2}$$

Where,  $D_k$  is the effective diameter of the element [m],  $\varphi$  is the stability parameter,  $\psi$  is the Shields parameter ( $\psi = \frac{\tau_{cr}}{(\rho_s - \rho_w)gD}$ , where  $\tau_{cr}$  is the critical shear stress at incipient motion [Pa], and  $D$  is the characteristic size of the element),  $K_T$  is the turbulence factor,  $K_h$  is the depth factor,  $K_S$  is the slope factor, and  $V_{cr}$  is the depth-averaged velocity at incipient motion [m/s].

The Pilarczyk design formula employs the critical depth-averaged velocity at incipient motion and a critical Shields parameter. Bezuijen and Vastenburger (2013) suggest using a Shields parameter of 0.035 for small geobags (< 0.3 m<sup>3</sup>) and a Shields parameter of 0.05 for larger geobags. These Shields parameters correspond to the empirical values for riprap and loose, placed blocks, respectively, which may not be applicable to geobags. Further, the Pilarczyk formula does not account for the flexibility and deformability of geobags.

Recio and Oumeraci (2009) derived two geobag stability formulas for geobag failure under coastal wave-loading. They incorporated an empirically determined deformation factor for a unique geobag, which does not account for variations in flexibility, dimensions and slope, or the impact of deformation on the coefficients of drag, inertia and lift (Recio and Oumeraci 2009). It is also noteworthy that hydraulic loading in coastal applications is different than in fluvial applications, such that their formulas may not be suitable for riverbank revetment structures.

Other studies have developed computer models to analyze geobag stability in fluvial applications which seek to improve the design process (Akter et al. 2013; Thompson et al. 2020b). Akter et al. (2013) coupled a discrete element model (DEM) with a numerical model to characterize the lift and drag forces acting on the geobag revetment structure, which they validated with depth-averaged velocity and visual observation of failing geobags. They did not propose a design

formula for sizing geobags and focused on revetment structures with geobags placed side-by-side. In the field, the geobags are dumped rather than placed, which impacts their stability (Thompson et al. 2020a). Thompson et al. (2020b) developed a computational fluid dynamics (CFD) model to study the hydraulic forces acting on geobags on a flat slope. Their model was validated with velocity profile data and the average total shear stress estimated via the energy slope method (Chow 1959) to provide an initial estimate of a critical Shields parameter of 0.09 for geobag elements. It would be beneficial to validate such models with known local bed shear stresses to enable higher accuracy.

#### 1.4 Knowledge Gaps

Studies on geobag application and stability have largely focused on coastal applications (e.g., Grune et al. 2007; Hornsey et al. 2010; Moreira et al. 2016; Recio and Oumeraci 2009). With geobags being considered a reliable and cost-effective alternative to riprap in river erosion protection structures, there have recently been more studies focused on fluvial applications (e.g., Korkut et al. 2007; Neill et al. 2008; NHC 2010; Akter et al. 2013; Thompson et al. 2020a; Thompson et al. 2020b; Khajenoori et al. 2021). However, there remain questions that still need to be answered about geobag stability in rivers, as well as opportunities to improve design methodologies for geobag sizing, as evidenced by diving explorations of existing revetment structures.

Previously, Thompson et al. (2020a; 2020b) studied the incipient motion of geobags and developed an initial understanding of shear stress as an indicator of incipient motion. There are limited studies that have attempted to estimate critical bed shear stresses for geobags in fluvial applications. Previous studies (i.e., Akter et al. 2013; Thompson et al. 2020b) have estimated bed shear stresses through computer models that were validated with depth-averaged velocity (Akter

et al. 2013), velocity profiles and an average bed shear stress estimated from the energy slope (Thompson et al. 2020b). There have been no studies, to the authors knowledge, that have investigated the suitability of different bed shear stress estimation methods for geobag applications in physical models. Furthermore, there are limited studies that perform a comprehensive comparison among bed shear stress estimation methods in complex flow conditions (Biron et al. 2004; Zhang et al. 2020). Chapter 2 seeks to address these limitations such that a suitable bed shear stress estimation method may be used in subsequent geobag stability studies.

Thompson et al. (2020a) suggested that geobag stability was a function of the sand filling ratio, which is consistent with the literature (i.e, Pilarczyk 2000; Grune et al. 2007); however, the influence of this parameter has not been independently studied in fluvial applications. Gogus and Defne (2005) determined that incipient motion, characterized through a critical Shields parameter, was a function of particle shape and relative roughness, in their study of large solitary particles. To the authors knowledge there have been no studies in fluvial applications that assess the geobag stability as a function of the different geobag characteristics (i.e., bag material, fill ratio, geobag shape) and bed configurations (i.e., bed side slope, relative roughness). Gaps have also been identified in the current design methodologies which rely on depth-averaged velocity, a variable which does not adequately describe the hydraulic forces acting on the bed. Furthermore, the design methodologies do not consider the unique geobag characteristics such as flexibility and deformability. Both Chapter 3 and 4 focus on filling these gaps and applying the results to pre-existing design formulas.

Finally, Thompson et al. (2020b) provided an initial estimation of a critical Shields parameters for geobags. Incipient motion is an inherently statistical problem, and as such, more study is

required to determine a range of critical Shields parameters with higher degree of confidence. Chapter 4 seeks to improve the confidence in critical Shields parameters for geobags.

## 1.5 Objectives

The objective of this thesis was to improve the applicability of current design formulas for geobags as well as our understanding of the critical Shields parameters for geobags. Incipient motion of geobags was studied under a variety of conditions to determine the relative importance of the geobag mass, flexibility, fill ratio, and shape on its stability. Critical bed shear stresses, critical Shields parameters and critical depth-averaged velocities were also estimated to characterize the incipient motion of geobags.

The studies presented in this thesis have employed scaled physical models to analyze the incipient motion of geobags. Chapter 2 presents a comparison of shear stress estimation methods to determine their suitability in the application of geobags on a rough bed under current loading. Chapter 3 presents the results of the laboratory experiments of incipient motion of a single geobag. The fill ratio, bag material, initial geobag shape, and bed side slope were varied to examine their impact on incipient motion of the single bag, and a shape factor is introduced. Chapter 4 presents the results of the laboratory experiments of the incipient motion of a geobag revetment structure, where the influence of geobag size and fill ratio were evaluated. A range of critical Shields parameters is presented, and pre-existing design formulas modified to improve their applicability for geobags.

## 2 A Comparison of Shear Stress Estimation Methods for a Single Geobag on a Rough Bed

### 2.1 Introduction

Sand-filled geotextile bags (geobags) have been utilized in river erosion protection structures for their advantages over riprap due to lower cost and the combined protection-filtering capability (e.g., Thompson et al. 2020a; Zhu et al. 2004). Currently, geobag erosion protection or revetment structures are designed with consideration to the critical depth-averaged-velocity, rather than the critical shear stress, for stability (Bezuijen and Vastenburger 2013; Oberhagemann et al. 2006). This may be one of the main reasons for oversizing the geobag elements, thus increasing the cost and labor required for such structures (Bezuijen and Vastenburger 2013; Thompson et al. 2020a). To improve the design, Akter et al. (2013) and Thompson et al. (2020b) modelled the incipient motion of geobags using a discrete element model (DEM) and computational fluid dynamics (CFD) model, respectively. Their models were validated with data from laboratory flume experiments, including depth-averaged velocity (Akter et al. 2013), as well as the average total shear stress estimated by the energy grade line (EGL) method over the test section and velocity profiles (Thompson et al. 2020b). Validation using locally measured shear stresses would provide higher confidence for such models, which in turn would improve design capabilities of geobag revetment structures. However, it is widely known that measuring local bed shear stress directly can be challenging and highly dependent on methods (Ackerman and Hoover 2001; Biron et al. 2004; Dietrich and Whiting 1989).

There are several bed shear stress estimation methods in the literature that may be applicable for geobags, but comprehensive comparisons among these methods are rather limited (Biron et al. 2004; Zhang et al. 2020). Biron et al. (2004) and Zhang et al. (2020) compared estimation methods under complex flow fields in fluvial applications, reaching different conclusions as to which

method is most applicable. The objective of this study is to conduct a detailed comparison and determine the most appropriate method(s) for practical use of geobags under open-channel flow conditions. The following shear stress estimation methods were evaluated: energy grade line (EGL), universal law of the wall, the Patel method, the Reynolds stress and the turbulent kinetic energy (TKE) methods. The comparison was based on laboratory open-channel experiments first on a smooth bare channel bed for direct comparisons with other studies, and then on a single geobag lying on a rough bed, under different flow conditions.

### 2.1.1 Literature Review

A brief review is provided for seven bed shear stress estimation methods reported in the literature.

#### 2.1.1.1 Energy Grade Line (EGL) Method

The EGL method (Eq. 2-1) determines the average total shear stress in a channel (Chow 1959). This method is sensitive to flow depth measurements over a short reach and is heavily influenced by bed-channel geometry and irregularity (Hoover and Ackerman 2004).

$$\tau_o = \gamma R S_f \quad \text{Eq. 2-1}$$

where  $\tau_o$  is the average total shear stress of the bed and banks,  $\gamma$  is the specific weight of water,  $S_f$  is the slope of the EGL and  $R$  is the hydraulic radius.

In narrow channels, the average bed shear stress is estimated by applying a correction for sidewall effect. For smooth beds, Guo and Julien (2005) devised an implicit method (Eq. 2-2) to estimate the average bed shear stress, correcting for the sidewalls, secondary currents and varying eddy viscosity in turbulent flows:

$$\overline{\tau_{b,S}} = \gamma h S_f \left[ \frac{4}{\pi} \tan^{-1} \left( \exp \left( -\frac{\pi h}{B} \right) \right) + \frac{\pi h}{4B} \exp \left( -\frac{h}{B} \right) \right] \quad \text{Eq. 2-2}$$

where  $\overline{\tau_{b,S}}$  is the average smooth bed shear stress,  $h$  is the flow depth and  $B$  is the channel width. For rough beds, Guo (2015; 2017) developed an alternative implicit method (Eq. 2-3) based on the Einstein-Johnson procedure:

$$\overline{\tau_{b,R}} = \gamma R_b S_f \quad \text{Eq. 2-3}$$

where  $\overline{\tau_{b,R}}$  is the average rough bed shear stress and  $R_b$  is the hydraulic radius of the bed ( $= \frac{A_b}{b}$ , where  $A_b$  is the flow cross-sectional subarea of the bed).

#### 2.1.1.2 Method of Universal Law of the Wall

The method of universal law of the wall is commonly used to estimate the local bed shear velocity as it only requires the time-averaged velocity data to fit the velocity profile to a logarithmic profile (Schlichting and Gersten 2000):

$$\frac{u}{u^*} = \frac{1}{k} \ln \left( \frac{z}{z_o} \right) \quad \text{Eq. 2-4}$$

where  $u$  is the measured velocity at height  $z$  from the bed,  $u^*$  is the local bed shear velocity,  $k$  is the von Karman constant ( $\approx 0.40$ ), and  $z_o$  is the roughness height.  $u^*$  is determined via linear regression of  $u$  vs.  $\ln(z)$ . The local bed shear stress is then calculated from  $u^*$  (Schlichting and Gersten 2000):

$$\tau_b = \rho u^{*2} \quad \text{Eq. 2-5}$$

where  $\rho$  is the fluid density.

The logarithmic profile described by the universal law of the wall occurs in the roughness region of flow (occupying the bottom 20% of the flow depth) and is expected to deviate slightly in the outer region of flow (Nezu and Nakagawa 1993). Fitting velocity data from the roughness flow region to a logarithmic profile is a process that Wilcock (1996) deemed imprecise as it is sensitive

to the shape of the velocity profile. In complex flow fields the velocity profile may not follow a logarithmic relationship (Biron et al. 2004).

### 2.1.1.3 Preston and Patel Methods

The Preston and Patel methods employ a Preston-Static or Pitot-Tube to estimate the local bed shear stress using an empirical relationship based on a non-dimensional function (Eq. 2-6), assuming the law of the wall holds true in the roughness layer (Preston 1954; Patel 1965).

$$\frac{\tau_b d^2}{4\rho v^2} = \text{fn}\left(\frac{\Delta p d^2}{4\rho v^2}\right) \quad \text{Eq. 2-6}$$

where  $d$  is the external diameter of the Pitot-Tube,  $v$  is the kinematic viscosity,  $\text{fn}$  is an empirically derived function, and  $\Delta p$  is the dynamic pressure measured by a Pitot-Tube or a Preston Static-Tube on the surface of the bed.

Patel (1965) expanded Preston's method by developing three empirical relationships (Eq. 2-7a- c) for laminar, transitional and turbulent flow conditions within a tube.

$$y^* = 0.50x^* + 0.0037 \quad \frac{u^* d}{2v} < 5.6 \text{ and } y^* < 1.5 \quad \text{Eq. 2-7 a}$$

$$y^* = 0.8287 - 0.1381x^* + 0.1437x^{*2} - 0.0060x^{*3} \quad 5.6 < \frac{u^* d}{2v} < 55 \text{ and } 1.5 < y^* < 3.5 \quad \text{Eq. 2-7 b}$$

$$x^* = y^* + 2\log(1.95y^* + 4.10) \quad 55 < \frac{u^* d}{2v} < 800 \text{ and } 3.5 < y^* < 5.3 \quad \text{Eq. 2-7 c}$$

where  $x^* = \log\left(\frac{\Delta p d^2}{4\rho v^2}\right)$ , representing the non-dimensional variable of the Preston relationship from Eq. 2-6, and  $y^* = \log\left(\frac{\tau_b d^2}{4\rho v^2}\right)$ .

Both Preston (1954) and Patel (1965) collected their experimental data from wind-tunnel experiments on a smooth surface. Their methods are sensitive to the angle of the Pitot-Tube to the approaching flow streamline, which presents a potential source of error in turbulent flow conditions where the flow streamline may separate (Ackerman and Hoover 2001). It should also

be noted that the Patel method relies on a single measurement of  $\Delta p$  on the surface of the bed, which has a larger potential error compared to using regression techniques with larger data sets (Wilcock 1996). Ackerman and Hoover (2001) employed the Patel method to estimate local bed shear stress in three different streams and determined that this relatively inexpensive and simple method is suitable for the field measurement of local bed shear stress where the flow is fully developed and unidirectional.

#### 2.1.1.4 Reynolds Stress Method

The Reynolds stress method is a relationship derived from the hydrodynamic equations for turbulent flow (Schlichting and Gersten 2000).

$$\tau_b = -\rho \langle u'w' \rangle \quad \text{Eq. 2-8}$$

where  $u'$  is the velocity fluctuation in the stream-wise direction and  $w'$  is the velocity fluctuation in the vertical direction. The Reynolds stress is sensitive to non-uniform flow conditions, due to assumptions made in the derivation, though it does not depend on the universal law of the wall assumption (Nezu and Nakagawa 1993).

A Reynolds stress profile is developed by measuring the velocity fluctuations at various flow depths and calculating shear stress at each depth. The linear portion of the profile is extrapolated to the bed to determine the local bed shear stress  $\tau_b$ . Alternatively, a near-bed Reynolds stress is calculated (with Eq. 2-8) at a single point. Biron et al. (2004) suggested the Reynolds stress at a non-dimensional height of 0.1 best described the bed shear stress to avoid measuring in the viscous sub-layer, where the non-dimensional height was the ratio of the distance from the bed of the measurement location to the entire flow depth. However, Zhang et al. (2020) pointed out Biron et al. (2004)'s method did not always capture the local bed shear stress and suggest re-estimating this height for complex flow fields.

### 2.1.1.5 Turbulent Kinetic Energy (TKE) Method

The TKE method is similar to the Reynolds stress method and requires measurement of the velocity fluctuations (Soulsby 1983).

$$\tau_b = C_1 \frac{\rho}{2} (\langle u'^2 \rangle + \langle v'^2 \rangle + \langle w'^2 \rangle) \quad \text{Eq. 2-9}$$

where  $C_1$  is a proportionality constant, and  $v'$  is the velocity fluctuation in the transverse direction. If an Acoustic Doppler Velocimeter (ADV) is used for measuring turbulent velocities, due to the ADV sensor geometry, velocity fluctuations measured in the vertical direction,  $w'$ , have the lowest instrument noise (Nikora and Goring 1998). Consequently, studies such as Kim et al. (2000), Biron et al. (2004) and Zhang et al. (2020) analyzed the TKE method using only  $w'$ , i.e., the TKE  $w'$  method:

$$\tau_b = C_2 \rho (\langle w'^2 \rangle) \quad \text{Eq. 2-10}$$

where  $C_2$  is a proportionality constant.

Soulsby (1983) reported  $C_1 = 0.18 - 0.20$  based on tidal data from the Irish Sea, Start Bay and Weymouth Bay, UK. Kim et al. (2000) reported  $C_1 = 0.19$  and  $C_2 = 0.90$  for oceanic applications with tidal effects. The TKE method was related to the shear stress calculated from the Reynolds stress method to estimate  $C_1$  in both studies, and to estimate  $C_2$  in Kim et al. (2000). For fluvial studies such as the present study, it is necessary to examine the suitability of the proportionality constants,  $C_1$  and  $C_2$ , as most reported values in the literature are from oceanic studies (Biron et al. 2004; Kim et al. 2000; Soulsby 1983; Zhang et al. 2020).

Both Biron et al. (2004) and Zhang et al. (2020) studied fluvial applications. In Biron et al. (2004) the open-channel flume was straight and in Zhang et al. (2020) the laboratory flume had a 60° bend. Biron et al. (2004) did not estimate new proportionality constants but based on their results one can perform a comparison between their TKE, TKE  $w'$  results and their Reynolds stress values

to determine new proportionality constants. Based on their results,  $C_1$  should increase by 112.0% ( $C_1 = 0.40$ ) and  $C_2$  by 78.5% ( $C_2 = 1.61$ ) from the constants estimated by Kim et al. (2000). Zhang et al. (2020) estimated new proportionality constants of  $C_1 = 0.23$  and  $C_2 = 0.44$  by the same methodology as Kim et al. (2000), for complex flow around a groyne in a 60° river bend.

#### 2.1.1.6 Other Methods

In addition to the methods above, the drag method and power-law approximation method have been used in the literature (White 1999; Biron et al. 2004). The drag method estimates the local bed shear stress by way of a drag coefficient and the depth-averaged velocity. The drag coefficient is difficult to independently estimate as it is not a constant; however, it may be estimated using the local bed shear stress calculated by another method, such as the Reynolds stress via extrapolation method (Biron et al. 2004). The power-law approximation method estimates the average bed shear stress and was empirically derived for turbulent flow over a flat plate (White 1999). This method employs the depth-average velocity and the downstream distance from the beginning of the study reach and is suitable for low turbulent Reynolds numbers ( $10^4 - 10^5$ ) (White 1999).

#### 2.1.1.7 Comparisons among Methods

Under the smooth bed conditions in a laboratory flume (0.2 m × 2.0 m, with 0.1 m water depth), Ackerman and Hoover (2001) determined that the local bed shear stress estimated from the Patel method compared well to the power-law approximation method, where the Patel method estimated higher values by 8% on average. They also reported that the universal law of the wall method estimated higher values by 39% on average than the power-law approximation. They attributed the differences to the sensitivity to the shape of the velocity profile, detailed by Wilcock (1996).

Biron et al. (2004) compared the methods in both smooth bed and complex flow conditions in a laboratory flume (0.4 m × 4.0 m, with flow depth of 9.5 cm). The complex flow condition was

created by placing two deflectors along opposite sidewalls over a sand bed. Biron et al. (2004) found that the universal law of the wall method estimated values at least 1.4 times higher than other methods (i.e., the Reynolds stress via extrapolation and Reynolds stress single point methods, the TKE, TKE  $w'$  and drag methods described above) over a smooth bed condition, which they attributed to the boundary layer not being fully developed at the measurement location. In the complex flow condition, Biron et al. (2004) determined that the TKE method most accurately described the expected local bed shear stresses around the deflectors and scour zones because the trends of the local bed shear stress estimates matched the trends of the turbulence intensity and mean near-bed streamwise velocities.

Recently, Zhang et al. (2020) compared methods under complex flow conditions for a groyne placed in a 60° bend in a flume, as stated earlier. Zhang et al. (2020) determined that the TKE  $w'$  method, estimated with their proportionality constant  $C_2 = 0.44$ , best described the expected local bed shear stresses compared to the TKE method.

The studies above are for fluvial applications and thus relevant to this study, though some comparisons have also been reported for coastal applications in Kim et al. (2000). From the literature, there is no clear agreement on which shear stress estimation method is most suitable for complex flow conditions in fluvial applications. There is also a need to validate the proportionality constants used in TKE methods for fluvial applications. This study seeks to address these gaps for complex flow conditions around a single geobag on a rough bed.

## 2.2 Methodology

The experiments in this study were conducted in a 1.2 m wide and 25 m long recirculating flume in the T. Blench Hydraulics Laboratory at the University of Alberta. The sidewall is glass and the

bed is fiberglass. The flow depth,  $h$ , was maintained at 0.30 m and the bed slope was set to 0%.

Flow depths were measured with a point gauge with an accuracy of +/- 0.5 mm.

The shear stress estimation methods were first compared for a smooth bed with no geobag at two Froude numbers of  $Fr = 0.29$  and  $Fr = 0.44$  (Series 1a and 1b, Table 2-1) and then for a rough bed with a single geobag filled with cement or sand at three Froude numbers of  $Fr = 0.29$ ,  $Fr = 0.44$  and  $Fr = 0.57$  (Series 2 to 7, Table 2-1). The Froude numbers for Series 2 to 7 were selected based on the flume's pump capacity, such that the highest Froude number corresponds to the highest achievable flow rate. The additional Froude numbers were for comparison purposes.

Table 2-1: Summary of experimental conditions

Series	Bed Substrate	Bag Field Scale (kg)	Bag Material	Fill Material	Flow w (L/s)	Mean Velocity (m/s)	Froude Number
1a	Plexiglass	No bag	No bag	No bag	180	0.50	0.29
1b	Plexiglass	No bag	No bag	No bag	270	0.75	0.44
2	Pea gravel	250	150g/m <sup>2</sup> geotextile	Cement	180	0.50	0.29
3	Pea gravel	250	150g/m <sup>2</sup> geotextile	Cement	270	0.75	0.44
4	Pea gravel	250	150g/m <sup>2</sup> geotextile	Cement	350	0.97	0.57
5	Pea gravel	250	150g/m <sup>2</sup> geotextile	Sand	180	0.50	0.29
6	Pea gravel	250	150g/m <sup>2</sup> geotextile	Sand	270	0.75	0.44
7	Pea gravel	250	150g/m <sup>2</sup> geotextile	Sand	350	0.97	0.57

The test section was located between 10 m and 15 m downstream of the flume head tank, where the flow was fully developed based on velocity profiles from the ADV. For the smooth bed experiments, the test section was 10 m downstream of the head tank. The entire bed was made of fiberglass, with a Manning's  $n$  of 0.0092. For the rough bed experiments, a 2 m long pea-gravel bed substrate (same width as the flume) was placed on the flume at 13 m downstream of the head tank. The Manning's  $n = 0.014$  for the rough bed, and the flow was fully developed 0.50 m downstream of the beginning of the rough bed from ADV measurements. The experimental set-up for the rough bed with a single geobag is shown in Figure 2-1.

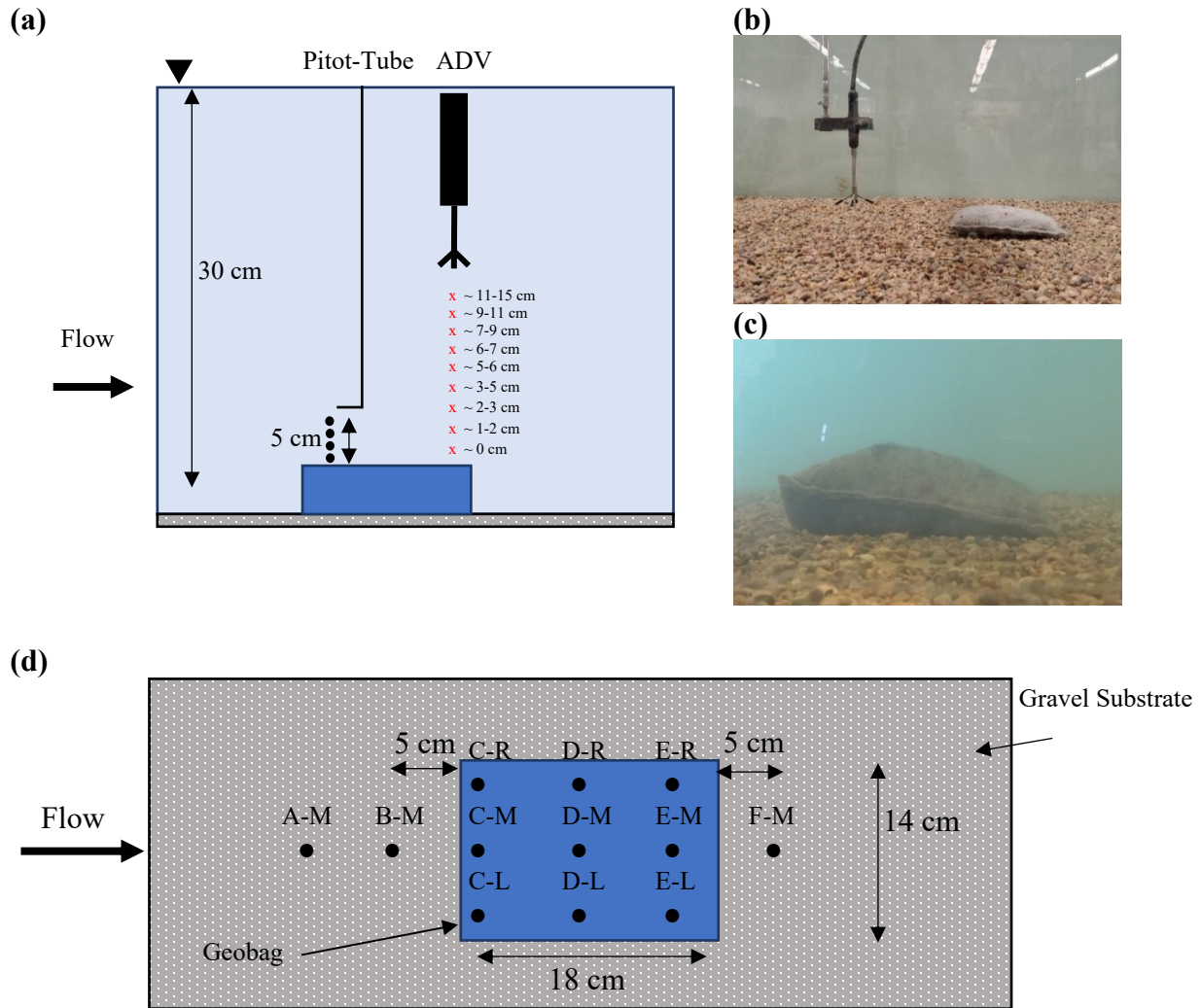


Figure 2-1: Experimental set-up and measurement locations for the single geobag tests, in (a-c) side view and (d) plan view. In (a), the measurement heights correspond to the distance above the bag; (b) shows the cement-filled bag used in Series 2 – 4, and (c) shows the sand-filled bag in Series 7.

The geobag size and mass were scaled using a 1:7 Froude scale based on the prototype geobags used in the Brahmaputra River, Bangladesh. The geobags used in the experiments were 14 cm wide  $\times$  18 cm long. The geobag filled with cement was filled completely to create a shape that roughly mimicked the natural shape of a sand-filled geobag at high Froude numbers. The geobag filled with sand was filled to 66% by mass to represent a standard 250 kg geobag prototype. The surface elevation for the cement filled geobag was captured with an intel RealSense Depth

Camera (Model: D435, Resolution 1280 x 800), that measured a total of 62,882 points within a 15 cm by 30 cm grid. The shape of the sand-filled bag changed at higher Froude numbers, because the sand shifted downstream in the bag and created a crest near the center cross-section of the bag, as shown in Figure 2-1c.

For the smooth bed series (Series 1a and 1b), the measurements were taken directly at and above the bed. For the rough bed series, the measurements were taken at and above the geobag, as well as upstream and downstream of it. Specifically, for Series 2, 5 and 8, the velocity profile, turbulence intensities and near-bed dynamic pressures were measured at all measurement locations shown in Figure 2-1 (locations A-M to F-M, inclusive). For the remaining series, they were measured at locations along the geobag centerline (B-M, C-M, D-M, E-M and F-M) and two additional locations above the bag at the center cross-section (D-R and D-L).

Velocity profiles and turbulence intensities were measured at 10 depths, ranging from approximately 0 cm from the bed or bag to half of the water depth at intervals of 2-3 cm, with a Vectrino ADV (P 21363-1). The ADV measured three-dimensional velocities at each point at a 100 Hz sampling rate for 5 minutes. The raw ADV data was filtered for an average correlation (CORR) greater than 70% and an average signal-to-noise ratio (SNR) greater than 15 dB, as recommended by the manufacturer (Nortek 2018). Phase-space thresholding was applied for despiking the ADV data as per Nikora and Goring (2000). The near-bed dynamic pressure was measured with a Pitot-Tube in the streamwise direction at 2-5 depths, ranging from 0 cm to 5 cm from the surface of the bed or bag. The Pitot-tube was outfitted with four-static pressure taps and one total pressure tap, with an external tube diameter of 3.125 mm. The Pitot-Tube was regularly purged in these experiments to prevent any blockage. Since the flow was turbulent, the angle of the Pitot-Tube was at  $0^\circ$  to the approaching flow assuming the flow streamline was straight in the

flume. The accuracy of the Pitot-Tube instrument is 0.001 inches of water column (= 0.022 m/s). The dynamic pressure measured from the Pitot-Tube was converted to velocity for a comparison to the time-average velocity measured with the ADV for various flow rates (see Figure 2-2). At higher velocity ranges ( $\geq 0.40$  m/s), there was reasonably good and consistent agreement ( $< 5\%$  difference) between the streamwise velocities measured by the ADV and Pitot-Tube, suggesting the reliability of both instruments. At the lower velocity of 0.20 m/s, although the difference was 22%, the actual difference is only 0.04 m/s, which is still satisfying.

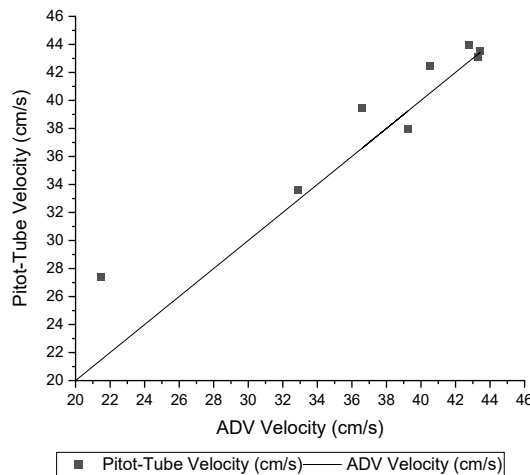


Figure 2-2: Comparison between time-averaged velocity data collected from the Pitot-Tube and ADV.

Five methods (EGL, universal law of the wall, Patel method, Reynolds stress and TKE method) were used to calculate bed shear stress in this study, which are described in the literature review. The drag method was not employed in this study as the coefficient of drag is variable and difficult to estimate (Biron et al. 2004). The power law approximation was also not employed, as it is not suitable for rough beds with protruding elements (White 1999). In the EGL method, the flow depths were measured at both ends of the 25-meter flume with a point gauge, accurate to the nearest 1 mm, to calculate the water surface slope. For the experiments of the geobag on a

rough bed, as only 8% of the flume bed was rough, a composite average bed shear stress was used (Eq. 2-11):

$$\bar{\tau}_b = 0.08(\overline{\tau_{b,R}}) + 0.92(\overline{\tau_{b,S}}) \quad \text{Eq. 2-11}$$

The flume was considered wide enough ( $B/h = 4$ ) to assume the average bed shear stress was approximately the same as the average total shear stress (Guo 2015). Therefore, the average total shear stress,  $\tau_o$  (Eq. 2-1), was compared to the average bed shear stress,  $\bar{\tau}_b$ . Although the primary goal of this study is to estimate the local bed shear stress, the average total shear stress and the average bed shear stress values may be used as a benchmark for comparison purposes.

In the universal law of the wall method, the time-averaged velocity data collected from the ADV were fit to a logarithmic profile to estimate the local bed shear stress. In the Patel method, the near-bed dynamic pressure data measured with the Pitot-Tube was used. In all experiment series, the Patel relationship for transitional flow (Eq. 2-7b) was employed because the  $y^*$  variable consistently ranged from 1.5 to 3.5 and the Pitot-Tube Reynolds number ranged from 5.6 to 55. In the Reynolds stress method, the instantaneous velocity data collected by the ADV were used to determine the velocity fluctuations in each direction. Both methods of linear extrapolation and measuring a single point at a non-dimensional height of 0.1 (Biron et al. 2004) were employed and compared. In the TKE and TKE  $w'$  methods, the velocity fluctuations were also used. The shear stress values at all measurement heights were compared between the TKE (or TKE  $w'$ ) and Reynolds stress methods to estimate new proportionality constants in Eq. 2-9 and Eq. 2-10.

## 2.3 Results and Discussion

### 2.3.1 TKE Proportionality Constants

Using the proportionality constants from Kim et al. (2000) (i.e.,  $C_1 = 0.19$  and  $C_2 = 0.90$ ; see Table 2-2), the shear stress estimated from both TKE methods were compared to the Reynolds

stress method, shown in Figure 2-3 for Series 2 – 4. The  $R^2$  values of linear fittings ranged from 0.62 to 0.95 with slopes,  $m$ , ranging from 0.37 to 0.67. For Series 5 - 7 (figure not shown), the  $R^2$  values ranged from 0.62 to 0.94 and the slopes ranged from 0.46 to 0.75. Ideally, the slopes should be closer to 1. These results are similar to those of Biron et al. (2004) who suggested this is a reasonably good fit when using the proportionality constants from Kim et al. (2000).

However, at shear stress values higher than 1 Pa both the TKE and TKE  $w'$  methods tend to estimate lower shear stress values compared to the Reynolds stress method in all the experiment series. For Series 1a and 1b (figure not shown), the estimates from the TKE and TKE  $w'$  methods are more comparable to the Reynolds stress estimates (TKE has an average  $R^2 = 0.71$ , with average slope  $m = 1.3$ ; TKE  $w'$  has an average  $R^2 = 0.82$ , with average slope  $m = 0.81$ ).

This may be due to the low shear stress values ( $< 0.70$  Pa) observed in the simple flow conditions over a smooth bed.

Table 2-2: Summary of the estimated proportionality constants,  $C_1$  and  $C_2$ , for TKE and TKE  $w'$  methods.

Study	$C_1$	$C_2$
Soulsby (1983)	0.18 – 0.20	–
Kim et al. (2000)	0.19	0.90
Biron et al. (2004)*	0.40	1.61
Zhang et al. (2020)	0.23	0.44
This study	0.30	1.60

\* $C_1$  and  $C_2$  were estimated based on the results of Biron et al. (2004), as they were not estimated in the original study.

As both TKE methods generate lower shear stress values compared to the Reynolds stress method in Series 2 - 7, new proportionality constants were estimated using the method in Kim et al. (2000) and Zhang et al. (2020). For Series 1a and 1b, the new proportionality constants were not estimated simply because there were not enough data in the smooth bed series. The new proportionality constants are  $C_1 = 0.30$  and  $C_2 = 1.60$ , which is an increase of 61.5% and

77.4% from the values ( $C_1 = 0.19$  and  $C_2 = 0.90$ ) of Kim et al. (2000), respectively. These results are comparable to those of Biron et al. (2004), and the  $C_1$  result is comparable to that of Zhang et al. (2020) (Table 2-2). However, the  $C_2$  result is greatly different to the value ( $C_2 = 0.44$ ) of Zhang et al. (2020). This may be caused by the difference in the experimental set-up: in Zhang et al. (2020) the flume had a  $60^\circ$  bend while in this study and Biron et al. (2004), the flume was straight. Channel bends tend to incur secondary flows, resulting in higher vertical velocity fluctuations, compared to straight channels (Chow 1959). Furthermore, the flow is more complex in Zhang et al. (2020)'s study due to the presence of a groyne structure in the bend.

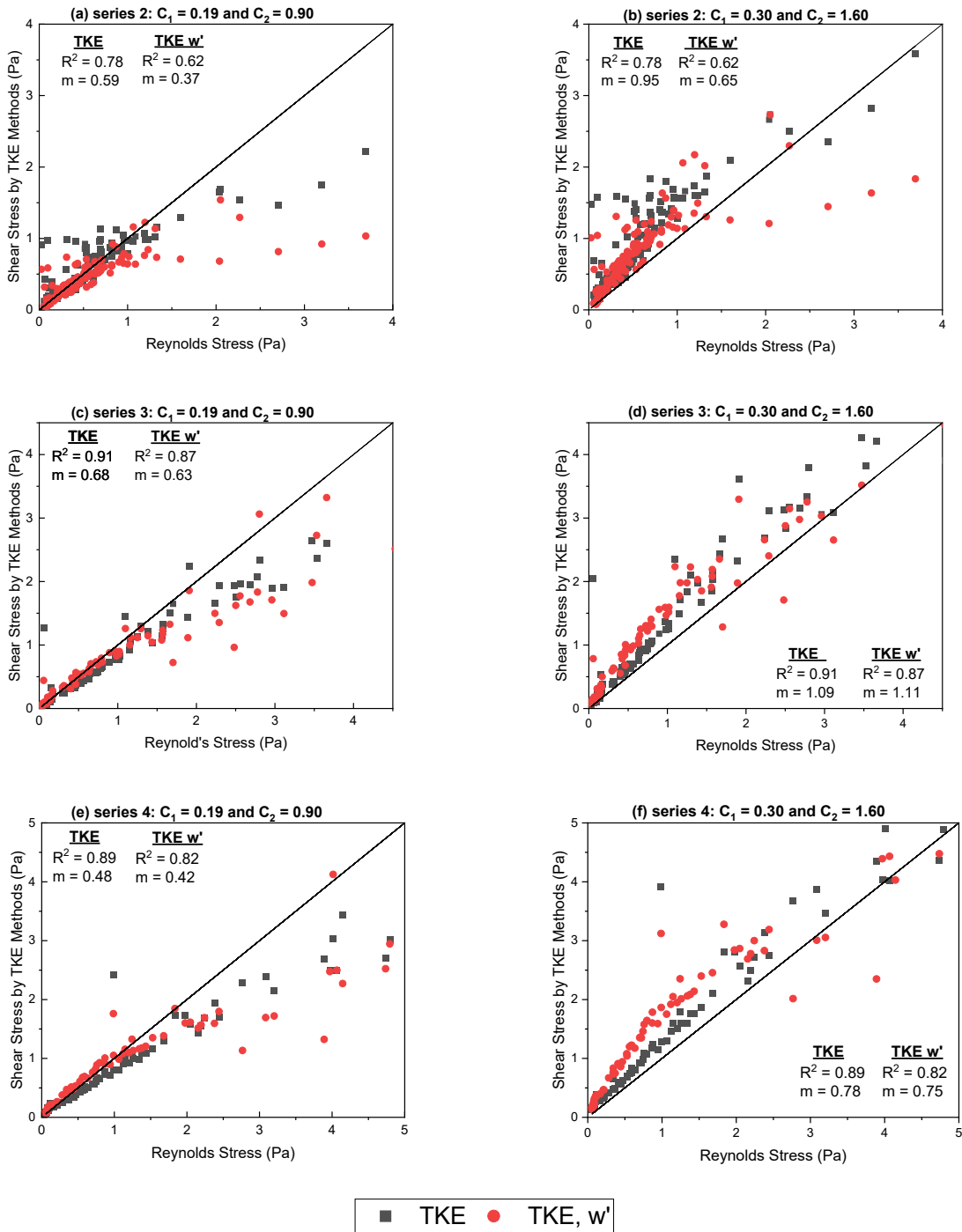


Figure 2-3: Comparison of the shear stress estimated from the TKE methods and the Reynolds stress, at all measurement heights from the bed in Series 2, 3 and 4, employing proportionality constants  $C_1 = 0.19$  and  $C_2 = 0.90$  in (a), (c) and (e), and the proportionality constants  $C_1 = 0.30$  and  $C_2 = 1.60$  in (b), (d) and (f).

### 2.3.2 Method Comparison - Smooth Bed Shear Stress

The results of local bed shear stress, the average bed shear stress and the average total shear stress with the various methods over the smooth bed are compared in Figure 2-4. The EGL average bed shear stress (from Eq. 2-11) estimated a slightly higher value than the EGL average total shear stress (Eq. 2-1), by 3.7% and 2.9% at  $Fr = 0.29$  and  $0.44$ , respectively. Consequently, the average total shear stress may be considered an adequate estimation of the average bed shear stress in this study.

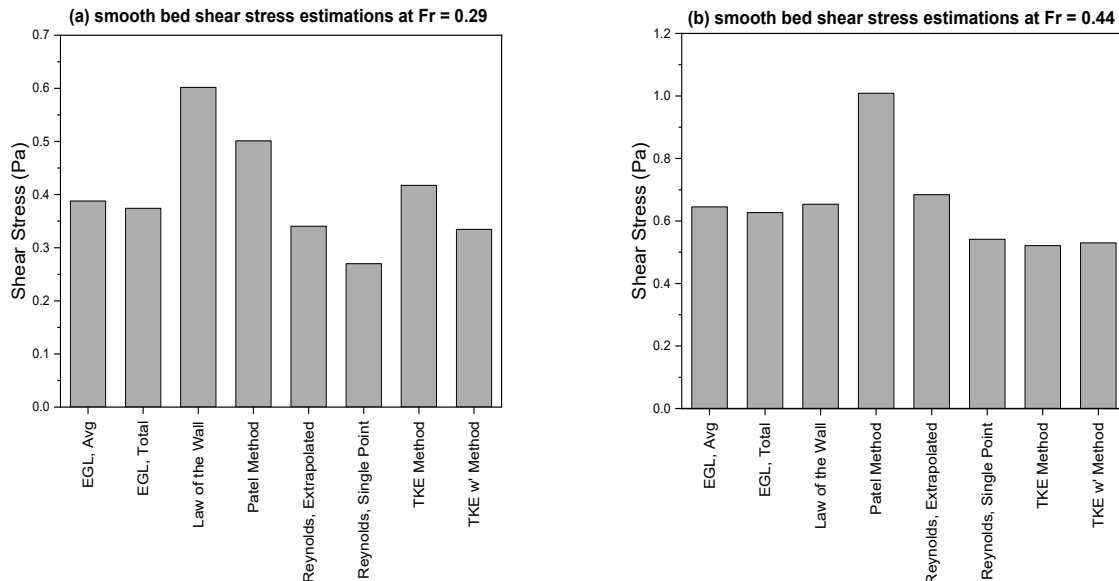


Figure 2-4: Shear stress estimations from each method on the smooth bed with (a)  $Fr = 0.29$ , and (b)  $Fr = 0.44$ .

At  $Fr = 0.29$ , the universal law of the wall method gives the highest local bed shear stress value (0.602 Pa), which is 1.6 times the EGL average total shear stress estimate (0.374 Pa) and 20% higher than the next highest estimate (0.501 Pa) from the Patel method. At  $Fr = 0.44$ , the Patel method estimates the highest local bed shear stress value (1.009 Pa), which is also 1.6 times the EGL average total shear stress estimate (0.627 Pa), and 47% higher than the next highest estimate (0.684 Pa) from the Reynolds stress via extrapolation method. Excluding the two highest shear stress estimates from the universal law of the wall and the Patel methods, the

remaining methods are within 35.3% of each other at  $Fr = 0.29$ . At  $Fr = 0.44$ , all methods, excluding the Patel method, are within 23.8% of each other, suggesting that at the higher Froude number there is a slightly better agreement among the different estimation methods.

Our results for smooth bed shear stress demonstrate a similar trend to those in the literature (Ackermann and Hoover 2001; Biron et al. 2004; Kim et al. 2000) where the universal law of the wall method estimated the highest local bed shear stress value at  $Fr = 0.29$ . This is not the case at the higher  $Fr$  number of 0.44, where this method shows the 3<sup>rd</sup> highest value. Notably, the Patel method relies on the law of the wall assumption and estimates the second highest and highest local bed shear stress values at  $Fr = 0.29$  and 0.44, respectively.

Biron et al. (2004) reasoned that the high estimates from the law of the wall method was due to undeveloped flow at the measurement location. In our study, the flow was fully developed at the location of measurement, and therefore the boundary layer was fully developed. However, the uncertainty relating to regression techniques (Wilcock 1996) and the applicability of empirical relationships (Eq. 2-7a-c) may explain the high estimates. The experimental conditions of Preston (1954) and Patel (1965) are drastically different from ours, as their experiments were conducted in a wind tunnel rather than open channel flow. These empirical regression models might need to be modified for conditions varying from their original experiments.

### 2.3.3 Method Comparison - Rough Bed Shear Stress

Contour plots of the bed elevation and local bed shear stress estimated from the different methods for the cement-filled geobag on the rough bed in Series 2 are shown in Figure 2-5 to further compare the different methods. For all the estimation methods, apart from the Patel method, the highest bed shear stress values on the geobag were located downstream of the geobag crest (see Figure 2-5a for the crest location), in locations E-R, E-L or F-M, and high

shear stress estimations are also located 5 cm upstream and downstream of the geobag (i.e., B-M and F-M). The lowest shear stress estimates were located leading up to and on the crest of the geobag (locations C-R, C-M, C-L, D-R, D-M, D-L). The Patel method illustrates an opposite pattern, where the highest shear stress estimates are located upstream of the crest of the geobag, and the lowest estimates are located downstream of this section.

Many previous studies demonstrated a wake form following the crest of a boulder or a blunt object in turbulent flow conditions, as well as a deceleration of flow approaching the object (Dey et al. 2011; Papanicolaou et al. 2012). It is therefore expected that the cement-filled geobag in Series 2, similar to a blunt object, generated similar phenomena. A wake is indicated in the shear stress contour estimated by the TKE method (Figure 2-5c), where greater shear stress values are located at the downstream corner locations (i.e., E-L and E-R) compared to the center location (i.e., E-M). This pattern is mimicked in the turbulence intensity and velocity distributions (see Figure 2-6). The shear stress contours estimated by the TKE  $w'$  method and the universal law of the wall method partially represent the wake on the right-hand side, whereas the Reynolds stress via extrapolation method partially represents the wake on the left-hand side and the Patel method fails to represent the wake formation clearly.

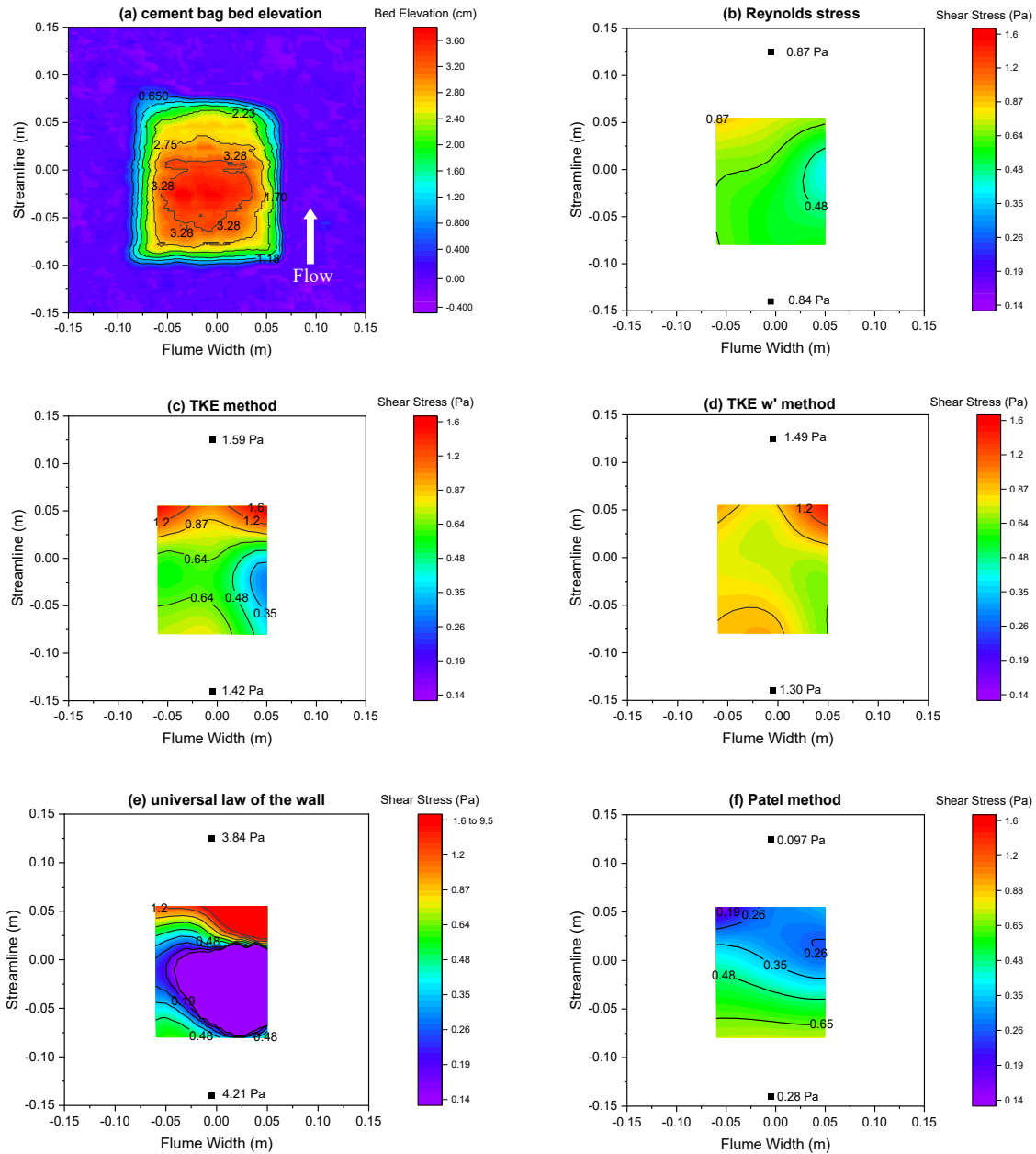


Figure 2-5: Contour plots for Series 2 on the rough bed, including (a) bed topography, and the local bed shear stress estimated by (b) Reynolds stress method via extrapolation, (c) TKE method, (d) TKE  $w'$  method, (e) universal law of the wall method, and (f) the Patel method.

Since the geobag shape is like a dune bedform, and deformable in the cases where the bag was filled with sand, it may also be compared to a sand dune bedform. Fernandez et al. (2006) observed that the highest shear stress estimates, estimated from the Reynolds stress method, were located downstream of a fixed-dune crest, and the lowest estimates were located leading up to

and on the dune crest, which are similar to our results with the exception of the Patel method. The high shear stress estimates downstream of the crest were attributed to flow separation and increased turbulence in their study. Slightly higher estimates were also observed further upstream of the dune crest in Fernandez et al. (2006), as was the case for the geobag at location B-M in this study. Based on the results of this study, the Patel method, which relies on a Pitot-Tube to measure the dynamic pressure, is unable to represent the shear stress estimates that are impacted by flow separation due to its limitations in capturing 3-D velocity fluctuations. Further, the Patel method requires positive integers in the estimation of the shear stress, which is not always guaranteed in measurement locations with significant turbulence, such as locations downstream of the geobag crest. This condition results in greater uncertainty in the Patel method.

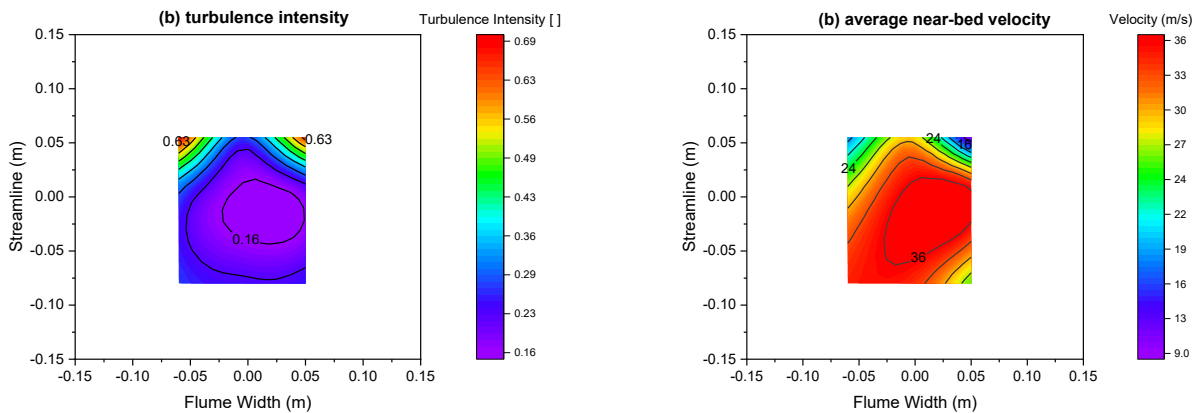


Figure 2-6: Contour plots of the streamwise (a) turbulence intensity, (b) velocity distribution for Series 2.

### 2.3.4 Method Comparison - Dimensionless Rough Bed Shear Stress

A comparison of the non-dimensional local bed shear stress values at all three Froude numbers for the cement and sand filled bags, respectively, are shown in Figure 2-7 and Figure 2-8 (Series 2 - 4 and Series 5 - 7). The non-dimensional local bed shear stress,  $\tau^*$ , is defined as the ratio of the local bed shear stress estimated by each method to the average bed shear stress estimated by the EGL method from Eq. 2-11.

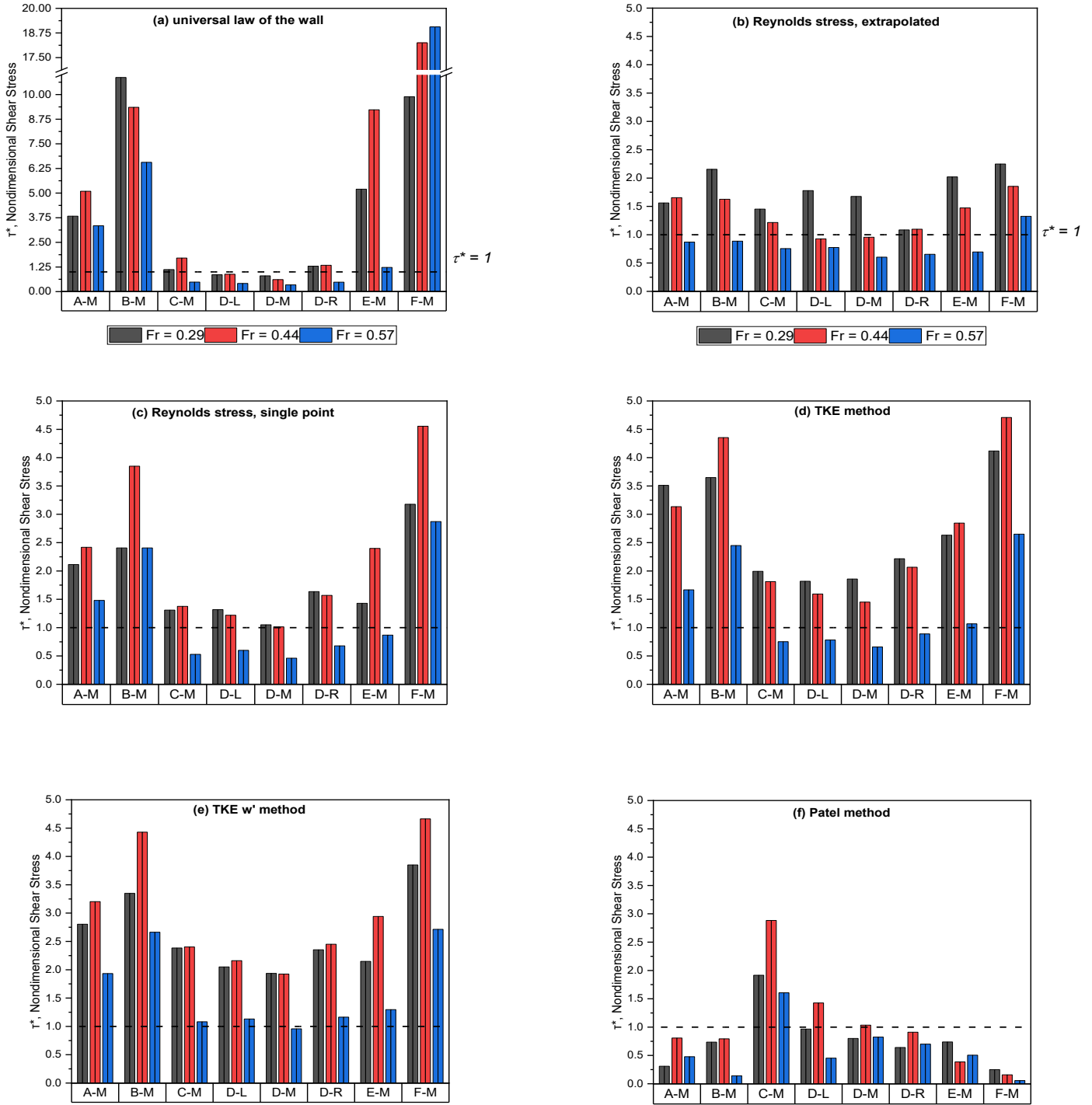


Figure 2-7: Comparison of dimensionless shear stress values for the cement-filled geobag at all Froude numbers (series 2, 3, 4), employing the a) universal law of the wall, b) extrapolated Reynold's stress, c) single near-bed point Reynold's stress, d) TKE, e) TKE  $w'$ , and f) Patel methods.

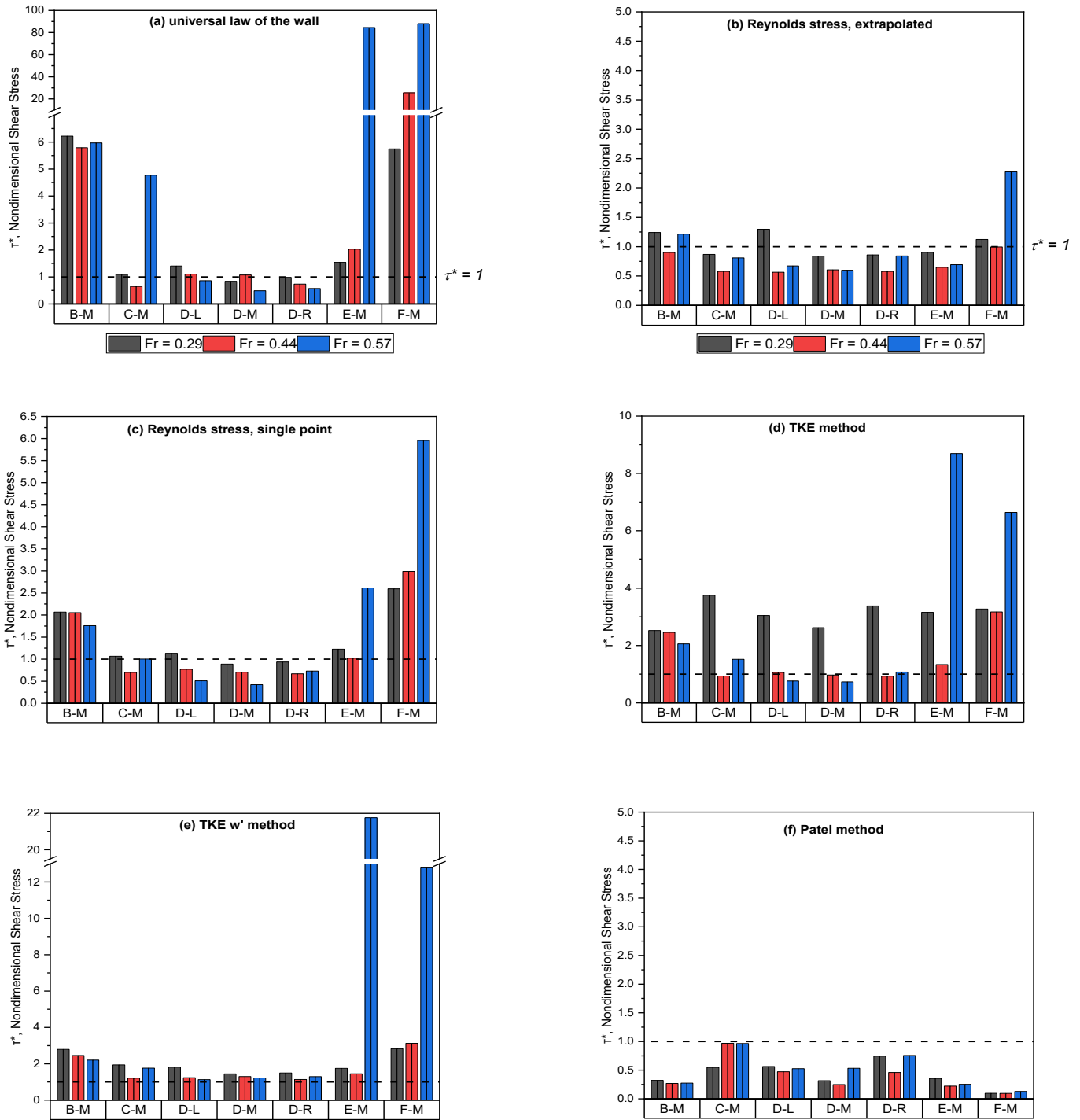


Figure 2-8: Comparison of dimensionless shear stress values for the sand-filled geobag at all Froude numbers (series 5, 6, 7), employing the a) universal law of the wall, b) extrapolated Reynold's stress, c) single near-bed point Reynold's stress, d) TKE, e) TKE  $w'$ , and f) Patel methods.

At higher Froude numbers, both higher average and local bed shear stress values are expected and thus the non-dimensional values may be comparable among the different Froude numbers. This is not always the case, where in Figure 2-8a and Figure 2-8e the dimensionless shear stresses at  $Fr = 0.57$  are an order of magnitude higher at locations E-M and F-M than the shear stresses at  $Fr = 0.29$  and  $Fr = 0.44$ . This may be due to a combination of factors such as the location of measurement, the bag shape and deformation, and the method for estimating the local bed shear stress. The sensitivity of the EGL method (discussed in the next section) may also explain why at the highest Froude number of 0.57, the estimated dimensionless local bed shear stress values are not necessarily comparable to the values estimated at the lower Froude numbers.

In Figure 2-7 and Figure 2-8, the dimensionless shear stress values estimated via the universal law of the wall method are significantly larger at the locations upstream and downstream of location D-M compared to the locations near the center of the bag (i.e., C-M, D-R, D-M, D-L). The extreme values downstream of the center of the bag are likely caused by the wake-formation and thus the breakdown of the law of the wall assumption (Papanicolaou et al. 2012). The values upstream of the center of the bag (i.e., B-M) are likely caused by the abrupt change in bed elevation from the rough bed to the geobag, which produces turbulence and impacts the shape of the velocity profile. In Biron et al. (2004), the universal law of the wall method estimated the highest bed shear stress over both plexiglass and sand beds, compared to the Reynolds stress, TKE and TKE  $w'$  methods, which is consistent with our results. At the center locations the universal law of the wall method estimated shear stress values comparable to the Reynolds stress, TKE and TKE  $w'$  methods, indicating that at areas with smaller turbulence intensity there is a better comparison between methods. One would expect the Patel method to demonstrate a

similar result, as it is based on the law of the wall assumption; however, in all figures the Patel method tends to estimate the lowest values, except at location C-M at all Froude numbers in Figure 2-7f and location C-M at  $Fr = 0.44$  in Figure 2-8f. Location C-M roughly corresponds to the crest of the cement-filled bag where the highest dynamic pressure values were measured. The low values in all other locations and series are explained by the inability of the Pitot-Tube to consider the effects of turbulence. The applicability of the Patel model is also questionable, as it was determined in a wind tunnel rather than an open channel river (Patel 1965). It is also important to note, at location F-M (5 cm downstream of the geobag) in Figure 2-7f and Figure 2-8f, the dynamic pressure readings were negative at the surface of the bed; therefore, the absolute value of the dynamic pressure was used in the Patel model, which could induce errors. To obtain an accurate positive pressure, the Pitot-Tube would need to be rotated to capture the flow direction, which was challenging at location F-M where the flow was not unidirectional and complex due to the wake effect of the geobag.

The shape of the sand-filled geobag varied depending on the Froude number, impacting the local bed shear stress estimations. At the lowest Froude number the geobag shape was relatively flat compared to its shape at higher Froude numbers, where a crest formed near the center cross-section of the geobag. In Figure 2-8, apart from the universal law of the wall method (Figure 2-8a) and the Patel method (Figure 2-8f), the local bed shear stress estimations are relatively similar regardless of measurement location at  $Fr = 0.29$ . At higher Froude numbers, the sand inside the bag shifts towards the downstream end of the bag. As more sand shifts downstream, the upstream section of the geobag lifts slightly to create a peak crest between the C-R, C-M, C-L and D-R, D-M, D-L locations, as shown in Figure 2-1c. At  $Fr = 0.57$ , the bag height increases from 3.55 cm to 5.35 cm which increases turbulence directly downstream of the bag based on the

ADV measurements, resulting in higher shear stress estimations from the TKE, TKE  $w'$  and Reynolds stress methods at the downstream locations of E-M and F-M, as shown in Figure 2-8. Notably, the TKE  $w'$  method estimates at these locations were the highest, suggesting that there is increased turbulence especially in the vertical direction downstream of the geobag crest, as the TKE  $w'$  method solely relies on vertical velocity fluctuations. It should be noted that in all sub-figures of Figure 2-8, the Reynolds stress employing the extrapolation method shows similar values in terms of scale and trend, indicating that this method is less affected by any changes to the bag shape, measurement location and flow conditions. It is expected that changes to the bag shape and flow conditions would impact the local bed shear stress values in different locations around the bag; therefore, the Reynolds stress via extrapolation method may not be suitable for this application.

### 2.3.5 Sources of Errors

In the estimation of the average total shear stress and the average bed shear stress via the EGL method, the sensitivity to flow depth measurements was investigated. In all series, the water surface slope had a height differential less than 1 cm and as such, a 1 mm difference in height measurement can result in a 20% difference in the estimated average shear stress. Due to small surface waves, which are almost unavoidable in any flume, the water depth measurements have some potential error. At higher flow rates, the height differential increases such that the sensitivity of the EGL method decreases, while the potential error may increase as surface waves also increase.

All local shear stress estimation methods used in this study rely on velocity measurements, including time-averaged-velocity, dynamic pressure and velocity fluctuations. It is therefore necessary to discuss the reliability of measurements by both the ADV and Pitot-Tube. For ADVs,

the effect of instrument noise (Doppler noise and sampling noise) on turbulence measurements has been discussed in the literature (Garcia et al. 2005; McLelland and Nicholas 2000; Moeini et al. 2019; Nikora and Goring 1998; Voulgaris and Trowbridge 1997), where Doppler noise effects were found to have little to no effect on TKE and Reynolds stress estimates. Doppler noise errors from ADV measurements consequently are not a concern to the results in this study with respect to the TKE, TKE  $w'$  and Reynolds stress estimations. The sampling noise has been reduced as much as possible in this study by increasing the user-set sampling frequency to 100 Hz, based on the recommendations from Garcia et al. (2005). As Nikora and Goring (2000) noted that nominal velocity range settings lower than the observed velocity range caused data aliasing, the user-set nominal velocity range settings were modified depending on the observed velocity.

The Pitot-Tube is arguably less robust in measuring velocity via the dynamic pressure, especially in high turbulent flow regimes where there can be significant flow separation (Ackerman and Hoover 2001). This is caused by the position of the Pitot-Tube in relation to the flow streamlines since the ideal position is where the Pitot-Tube is within  $20^\circ$  to the flow streamline (Ackerman and Hoover 2001). Other issues with the Pitot-Tube include the possible damping effect of long tubing to the pressure transducer, the response rate of the transducer to velocity fluctuations and potential blockage in the static and total-pressure ports (Ackerman and Hoover 2001). The Pitot-Tube was regularly purged in our experiments to prevent any blockage.

## 2.4 Conclusions

There are limited studies that perform a comprehensive comparison between the various bed shear stress estimation methods, especially under complex flow conditions. This study compared various bed shear stress estimation methods to determine the most suitable method for the practical use of geobags in river environment. Five shear stress estimation methods (including

EGL, universal law of the wall, the Patel method, the Reynolds stress and TKE methods) were compared for both a smooth bed condition, and a rough bed condition with a single geobag filled with cement or sand under different flow conditions.

Based on this experimental study, a summary of the applicability of each bed shear stress estimation method is provided in Table 2-3. In the smooth bed condition, the methods compared reasonably well with each other (within 35% of each other), apart from the high estimates from the Patel method at both Froude numbers ( $Fr = 0.29$  and  $Fr = 0.44$ ) and the universal law of the wall method at the lower Froude number of 0.29. Uncertainty relating to regression techniques, as well as using a single point of measurement for the near-bed dynamic pressure, rather than multiple-point measurements, contribute to these differences.

In the complex flow condition for a single geobag on a rough bed, new proportionality constants of  $C_1 = 0.30$  and  $C_2 = 1.6$  were estimated for the TKE and TKE  $w'$  methods. The TKE and TKE  $w'$  methods both reflected the changes in geobag shape and flow conditions. The TKE method represented the bed topography and the wake following the geobag crest better than the other methods. In contrast, the Reynolds stress method did not represent the expected wake-form following the geobag crest or the changes to the geobag shape at higher Froude numbers. The Patel method was deemed the least suitable due to its inability to capture the effects of turbulence and uncertainty about the method applicability. The universal law of the wall method is also unsuitable for the complex flow condition, as velocity profiles did not always follow a logarithmic profile especially in the wake following the geobag crest. The results of this study suggest that the TKE method is the most suitable for complex flow conditions involving a single geobag on a rough bed.

Table 2-3: Summary of the results of the local bed shear stress estimation methods

Method	Summary
Universal Law of the Wall	<ul style="list-style-type: none"> <li>• Estimated highest value in the smooth bed condition at <math>Fr = 0.29</math></li> <li>• Law of the wall breaks down upstream and downstream of geobag</li> </ul>
Patel Method	<ul style="list-style-type: none"> <li>• Estimates 2<sup>nd</sup> highest (<math>Fr = 0.29</math>) and highest value (<math>Fr = 0.44</math>) in the smooth bed condition</li> <li>• Does not consider turbulence affects</li> </ul>
Reynolds Stress, Extrapolated	<ul style="list-style-type: none"> <li>• Does not reflect changes to the bag shape, flow conditions and measurement locations</li> </ul>
Reynolds Stress, Single Point	<ul style="list-style-type: none"> <li>• Reflects changes to the bag shape, flow conditions and measurement locations</li> <li>• Single point has higher uncertainty than extrapolation method</li> </ul>
TKE Method	<ul style="list-style-type: none"> <li>• Reflects changes to the bag shape, flow conditions and measurement locations</li> <li>• New proportionality constant estimated, <math>C_1 = 0.30</math></li> <li>• Indicates a wake form following the cement-filled geobag</li> </ul>
TKE $w'$ Method	<ul style="list-style-type: none"> <li>• Represents changes to the bag shape, flow conditions and measurement locations</li> <li>• New proportionality constant estimated, <math>C_2 = 1.60</math></li> </ul>

For future considerations, it would be beneficial to conduct more comparisons among the different methods under different flow conditions. Additionally, the Patel method may need to be modified for open channel flow applications similar to our study. It would also be useful to estimate the proportionality constants in fluvial applications of various channel geometries, such that the TKE and TKE  $w'$  methods may be more widely applied.

## 2.5 References

- Ackerman, J. D. & Hoover, T. M., 2001. Measurement of local bed shear stress in streams using a Preston-static tube. *Limnology and Oceanography*, 46(8), pp. 2080-2087.
- Akter, A., Pender, G., Wright, G. & Crapper, M., 2013. Performance of a Geobag Revetment I: Quasi-Physical Modeling. *Journal of Hydraulic Engineering*, 139(8), pp. 865-876.
- Bezuijen, A. & Vastenbunrg, E., 2013. *Geosystems. Design Rules and Applications*. 1st ed. London: Taylor & Francis Group.

- Biron, P. M., Robson, C., Lapointe, M. F. & Gaskin, S. J., 2004. Comparing different methods of bed shear stress estimates in simple and complex flow fields. *Earth Surface Processes and Landforms*, Volume 29, pp. 1403-1415.
- Chow, V. T., 1959. *Open-Channel Hydraulics*. 1st ed. Tokyo: McGraw-Hill Book Company.
- Dey, S. et al., 2011. Wall-wake flows downstream of a sphere placed on a rough wall. *Journal of Hydraulic Engineering*, 137(10), pp. 1173-1189.
- Dietrich, W. E. & Whiting, P., 1989. Boundary shear stress and sediment transport in river meanders of sand and gravel. *Water Resources Monograph*, Volume 12, pp. 1 - 50.
- Fernandez, R., Best, J. & Lopez, F., 2006. Mean flow, turbulence structure, and bed form superimposition across the ripple-dune transition. *Water Resources Research*, Volume 42, pp. 1-17.
- Garcia, C. M., Cantero, M. I., Nino, Y. & Garcia, M. H., 2005. Turbulence measurements with acoustic doppler velocimeters. *Journal of Hydraulic Engineering*, 131(12), pp. 1062-1073.
- Gordon, L. & Cox, J., 2000. *Acoustic doppler velocimeter performance in a laboratory flume*, San Diego, California: NortekUSA.
- Guo, J., 2015. Sidewall and non-uniformity corrections for flume experiments. *Journal of Hydraulic Research*, 53(2), pp. 218-229.
- Guo, J., 2017. Exact Procedure for Einstein-Johnson's Sidewall Correction in Open Channel Flow. *Journal of Hydraulic Engineering*, 143(4), pp. 1-6.
- Guo, J. & Julien, P. Y., 2005. Shear Stress in Smooth Rectangular Open-Channel Flows. *Journal of Hydraulic Engineering*, 131(1), pp. 30-37.
- Henderson, F. M., 1966. *Open Channel Flow*. New York: Macmillan.
- Hoover, T. M. & Ackerman, J. D., 2004. Near-bed hydrodynamic measurements above boulders in shallow torrential streams: Implications for stream biota. *Journal of Environmental Engineering*, Volume 3, pp. 365-378.
- Kim, S.-C., Friedrichs, C. T., Maa, P.-Y. & Wright, L. D., 2000. Estimating bottom stress in tidal boundary layer from acoustic doppler velocimeter data. *Journal of Hydraulic Engineering*, 126(6), pp. 399-406.
- McLelland, S. J. & Nicholas, A. P., 2000. A new method for evaluating errors in high-frequency ADV measurements. *Hydrological Processes*, Volume 14, pp. 351-366.
- Moeini, M., Kazemi, M., Khorsandi, B. & Mydlarski, L., 2019. *A laboratory study of the effect of acoustic doppler velocimeter sampling frequency and sampling volume on measurements*. Laval, CSCE Annual Conference.
- Nezu, I. & Nakagawa, H., 1993. *Turbulence in Open-Channel Flows*. 1 ed. Rotterdam: A.A.Balkema.

- Nikora, V. & Goring, D., 2000. Flow turbulence over fixed and weakly mobile gravel beds. *Journal of Hydraulic Engineering*, 126(9), pp. 679-690.
- Nikora, V. I. & Goring, D. G., 1998. ADV measurements of turbulence: Can we improve their interpretation?. *Journal of Hydraulic Engineering*, 124(6), pp. 630-634.
- Nortek, 2018. *The Comprehensive Manual for Velocimeters*, s.l.: s.n.
- Oberhagemann, K., Stevens, M., Haque, S. & Faisal, M., 2006. *Geobags for Riverbank Protection*. Amsterdam, Proceedings 3rd International Conference on Scour and Erosion (ICSE-3).
- Papanicolaou, A. N. et al., 2012. Effects of a fully submerged boulder within a boulder array on the mean and turbulent flow fields: Implications to bedload transport. *Acta Geophysica*, 60(6), pp. 1502-1546.
- Patel, V. C., 1965. Calibration of the Preston tube and limitations on its use in pressure gradients. *Journal of Fluid Mechanics*, 23(1), pp. 185-208.
- Pokrajac, D. et al., 2006. On the definition of the shear velocity in rough bed open channel flows. *Proceedings of the International Conference of Fluvial Hydraulics - River Flow*, pp. 89-98.
- Preston, J. H., 1954. The determination of turbulent skin friction by means of Pitot tubes. *Journal of the Royal Aeronautical Society*, Volume 58, pp. 109-121.
- Schindler, R. J. & Robert, A., 2005. Flow and turbulence structure across the ripple-dune transition: an experiment under mobile bed conditions. *Sedimentology*, Volume 52, pp. 627-649.
- Schindler, R. & Robert, A., 2004. Suspended sediment concentration and the ripple - dune transition. *Hydrological Processes*, Volume 18, pp. 3215-3227.
- Schlichting, H. & Gersten, K., 2000. *Boundary-Layer Theory*. 8 ed. Berlin: Springer-Verlag.
- Soulsby, R. L., 1983. The Bottom Boundary Layer of Shelf Seas. In: J. B., ed. *Physical Oceanography of Coastal and Shelf Areas*. Amsterdam: Elsevier, pp. 189-266.
- Sutardi & Ching, C. Y., 2001. Effect of tube diameter on Preston tube calibration curves for the measurement of wall shear stress. *Experimental Thermal and Fluid Sciences*, Volume 24, pp. 93-97.
- Thompson, A., Oberhagemann, K. & She, Y., 2020a. Geobag stability for riverbank erosion protection structures: Physical model study. *Geotextiles and Geomembranes*, 48(1), pp. 110-119.
- Thompson, A., She, Y. & Oberhagemann, K., 2020b. Geobag stability for riverbank erosion protection structures: Numerical model study. *Geotextiles and Geomembranes*, 48(5), pp. 703-712.
- Voulgaris, G. & Trowbridge, J. H., 1997. Evaluation of the Acoustic Doppler Velocimeter (ADV) for Turbulence Measurements. *Journal of Atmospheric and Oceanic Technology*, Volume 15, pp. 272-289.

White, F. M., 1999. Chapter 7 Flow Past Immersed Bodies. In: J. P. Holman & J. Lloyd, eds. *Fluid Mechanics*. 4th ed. s.l.:McGraw-Hill, pp. 427 - 494.

Wilcock, P. R., 1996. Estimating local bed shear stress from velocity observations. *Water Resources Research*, 32(11), pp. 3361-3366.

Zhang, L. et al., 2020. Comparison of Methods for Bed Shear Stress Estimation in Complex Flow Field of Bend. *Water*, 2753(12), pp. 1-16.

Zhu, L. et al., 2004. Settling Distance and Incipient Motion of Sandbags in Open Channel Flows. *Journal of Waterway, Port, Coastal and Ocean Engineering*, 130(2), pp. 98-103.

### 3 Effects of Bag Characteristics on Incipient Motion of a Single Geobag

#### 3.1 Introduction

Geobags (geotextile bags filled with sand) have been used as primary elements in erosion protection or revetment structures in several rivers (e.g., Thompson et al. 2020a; Yang et al. 2008; Zhu et al. 2004). Benefits to using geobags as primary elements in revetment structures include their relatively low cost and combined filtering-protection ability which increases scour protection in the self-launching apron (Heibaum et al. 2008; Heibaum 2014; Oberhagemann and Hossain 2011). Designing revetment structures requires knowledge on the element stability under the hydraulic loading conditions of the study reach. In coastal applications, geobag stability has been studied rather extensively (e.g., Grune et al. 2007; Hornsey et al. 2010; Moreira et al. 2016; Recio and Oumeraci 2009). However, hydraulic loading in coastal applications is dominated by wave loading whereas in fluvial applications it is dominated by current loading (Pilarczyk 1991). As such the two applications require independent study.

A limitation to using geobags in revetment structures is that there is relatively little knowledge on their stability in fluvial applications, which ultimately results in the potential for their overdesign (Oberhagemann and Hossain 2011; Thompson et al. 2020a). Thus far, fluvial studies on geobag stability have largely focused on failure mechanisms (i.e., geobags in revetment structures may fail by uplifting, pulling-out or sliding) (Akter et al. 2013; Khajenoori et al. 2021), geobag revetment configurations (Akter et al. 2013; Korkut et al. 2007) and modifications to pre-existing rock sizing formulas for geobag applications (Neill et al. 2008; NHC 2010; Thompson et al. 2020a). Currently, geobags are sized with a design formula for riprap developed by the U.S. Army Corps of Engineers (USACE), which has been modified by Neill et al. (2008), NHC (2010) and Thompson et al. (2020a). Although improvements have been made to the current geobag sizing formula, it relies on a depth-averaged velocity and empirically calibrated

stability coefficient to determine a stable geobag size (USACE 1994). This formula does not consider the deformation, flexibility, or shape of geobags which may be crucial components to their stability (Pilarczyk 2000; Gogus and Defne 2005; Grune et al. 2007; Thompson et al. 2020a).

Grune et al. (2007) observed that geobags with higher fill ratios of sand were more stable under wave loading for coastal applications. Under current loading, Thompson et al. (2020a) indicated a similar trend to Grune et al. (2007) based on the results from their physical model. Their study did not evaluate the fill ratio independently of other variables such that this trend needs further investigation. Thompson et al. (2020a) also evaluated the stability of geobags with different bag materials, which mainly resulted in different flexibility, though the impact of the bag material also requires further evaluation. Gogus and Defne (2005) studied large solitary particles of varying shapes and found that the stability was a function of particle shape. Shields (1936) also observed that grain shape (i.e., rounded grains versus angular grains) impacted the stability of the bed. To the author's knowledge, the impact of geobag shape on its stability has not been previously studied, which may be due to the challenge of controlling the geobags shape. It would be interesting to learn if the initial shape of a flexible element has an impact on its stability under current loading.

Incipient motion is defined as when the element(s) begin to move (Shields 1936), or when the acting lift, drag and inertia forces exceed the contact and submerged weight forces of the element(s) (Pilarczyk 1991). The USACE (1994) design formula employs a critical depth-averaged velocity to describe incipient motion of an element because this variable can be easily measured in the field. However, bed load transport is often characterized by bed shear stresses since these reflect the acting forces on the bed that cause incipient motion. Shields (1936)

defined a dimensionless parameter to characterize the incipient motion of sediment, based on a critical bed shear stress:

$$\psi = \frac{\tau_{cr}}{(\rho_s - \rho_w)gd_n} \quad \text{Eq. 3-1}$$

Where,  $\psi$  is the Shield's parameter,  $\tau_{cr}$  is the critical shear stress at incipient motion [Pa],  $\rho_w$  is the density of water [kg/m<sup>3</sup>],  $\rho_s$  is the density of the sediment or element [kg/m<sup>3</sup>],  $g$  is the acceleration due to gravity [m/s<sup>2</sup>], and  $d_n$  is the characteristic size. Shields (1936) defined the characteristic size as the cube root of the particle's volume.

Different studies have estimated the critical bed shear stress via the Reynolds stress, logarithmic wall of the law and energy grade line method (Buffington and Montgomery 1997; Recking 2009). Local bed shear stresses can be higher than the average bed shear stress applied to the entire study reach due to variations in bed roughness (Neill 1968). Therefore, employing a critical local bed shear stress in the Shields parameter formula may be more representative of the instantaneous conditions at incipient motion. Shields (1936) demonstrated that the critical Shields parameter becomes constant above a boundary Reynolds number of approximately 1000 ( $Re = \frac{u_{cr}^* d_n}{\nu}$ ; where  $Re$  is the boundary Reynolds number,  $u_{cr}^*$  is the critical shear velocity ( $= \sqrt{\tau_{cr}/\rho_w}$ ) and  $\nu$  is the kinematic viscosity). The value of this constant can be useful in design formulas as it indicates a single threshold for incipient motion of the element under any rough, turbulent flow condition.

Thompson et al. (2020a) studied the stability of a bed of geobags under current loading in a physical model. Velocity profiles and the critical depth-averaged velocity were determined at incipient motion (when 5% of the elements had been displaced) of geobags and a control section made of rocks. Thompson et al. (2020b) used these data to validate a computational fluid

dynamics (CFD) model and characterized the forces acting on the bed to estimate the critical bed shear stresses and Shields parameters. They provided an estimate of a critical Shields parameter for geobags ( $= 0.09$ ) and for the control section of rock ( $= 0.041$ ). The critical Shields parameter for rock has previously been estimated at 0.045 (Buffington and Montgomery 1997). Thompson et al. (2020b) explained that the higher critical Shields parameter for geobags compared to their control rock section was due to a higher drag force acting on the geobags and their relatively low density compared to rock. To the author's knowledge, only Thompson et al. (2020b) have estimated a critical Shields parameter for geobags. Critical Shields parameters are inherently statistical, due to the instantaneous nature of incipient motion (Shields 1936; Neill 1968). Furthermore, variations to the definition of incipient motion, measurement techniques, critical shear stress estimation methods and element uniformity increase the variability in critical Shields parameters (Buffington and Montgomery 1997). Determining a critical Shields parameter for geobags therefore requires more data and an understanding of the influence of different geobag parameters on their stability.

The objective of this study was to gain a better understanding of geobag stability and the influencing factors. A scaled physical model of a single geobag placed on a rough surface was constructed. The fill ratio of sand, geobag shape, bag material and side slope were varied to determine their impact on the incipient motion of the single geobag. Local bed shear stresses were estimated on the geobag to calculate the critical Shields parameters at incipient motion. This paper presents the cross-sectional average flow velocity corresponding to the geobags incipient motion, along with the critical Shields parameters. A shape factor is proposed to provide a better understanding of the impact of geobag flexibility and fill ratio on the incipient motion and the critical Shields parameters.

## 3.2 Methodology

### 3.2.1 Experimental Set-Up

The experiments were conducted in a recirculating flume (1.2 m x 25 m) in the T. Blench Hydraulics Laboratory at the University of Alberta. The flume sidewalls were made of glass and the bed at the test section was made of roofing asphalt (Manning's  $n = 0.016$ ). The flume slope was set at 0%. The test section was placed 13 m downstream of the flume head tank. Two bed configurations were studied: a flat bed and a 1V:2H sloped bed (see Figure 3-1). In the flat bed configuration, the asphalt bed was 2 m long and the single geobag was placed in the center, 1 m downstream of the beginning of the asphalt. In the 1V:2H sloped bed configuration, the asphalt covered side slope was 6 m long and the single geobag was placed 5 m downstream of the beginning of the slope. A 2-meter transition section was attached to the upstream edge of the slope to minimize the change in flow depth from the flat bed to the sloped bed. The flat bed configuration provides a baseline for comparisons and the slope bed configuration represents the launched slope of geobags in the field, where geobags self-launch to a geotechnically stable slope of 1V:2H (Oberhagemann and Hossain 2011). Flow was fully developed upstream of the single geobag for both the flat bed and 1V:2H sloped bed, verified by Acoustic Doppler Velocimeter (ADV) measurements of the velocity profiles. The single geobag was placed in the center of the test section to minimize sidewall effects.

The flow capacity of the flume's pump was  $0.390 \text{ m}^3/\text{s}$ . To ensure the velocity would be high enough to incur incipient motion, the flow depth,  $h$ , was maintained at 0.30 m above the geobag. Flow depths were measured with a point gauge with an accuracy of  $\pm 0.5 \text{ mm}$ . Schematics of the experimental set-up are shown in Figure 3-1 for both bed configurations.

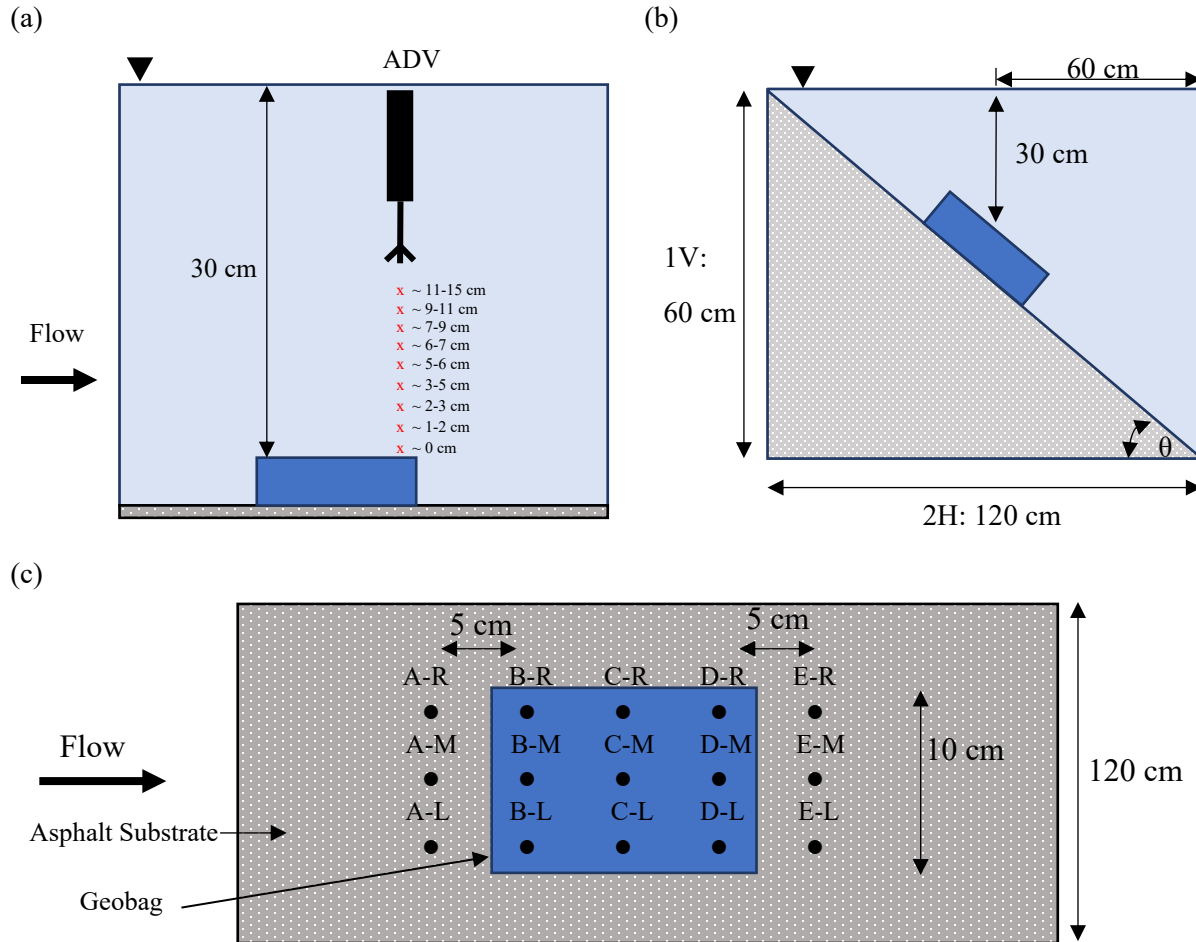
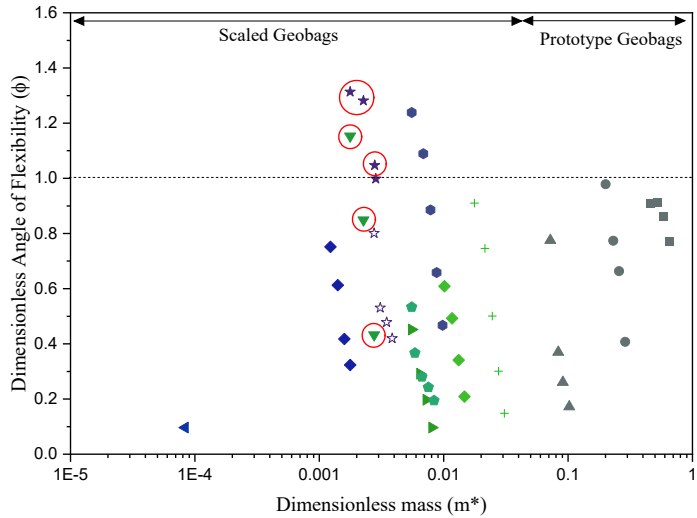


Figure 3-1: Schematic of the (a) sideview of the flat-bed configuration, (b) the cross-sectional view of the 1V:2H slope-bed configuration (flow going into the page), and (c) the plan view of the measurement locations.

### 3.2.2 Geobag Characteristics

The geobags were scaled from a 125 kg prototype geobag used in the Bangladesh projects, using a 1:7 Froude scale. Six geobags of the same dimensions (10 cm x 15 cm) with varying sand fill ratios and bag materials were studied (see Table 3-1). Three fill ratios were studied: 84%, 69% and 54%. The fill ratio was defined as the actual geobag mass divided by the geobag mass when fully filled with sand. The fill ratio of 84% was selected because its mass corresponds to the scaled 125 kg prototype geobag mass (0.364 kg). As the literature suggests a fill ratio of ~80% is most stable for geobags (Thompson et al. 2020a; Pilarczyk 2000), two additional fill ratios of 69% and 54% were also studied to observe the effect of fill ratio on geobag stability. Two bag

materials were also studied: geotextile and cloth. Due to the porosity of the geotextile material, the lowest possible fabric weight is 150 g/m<sup>2</sup>. This, along with the fill ratio, impacts the flexibility of the geobag. The flexibility of the geobag is an important characteristic that can be challenging to scale down proportionally especially as the scaling factor increases (NHC 2010; Thompson et al. 2020a). Therefore, a cloth material with a fabric weight of 80 g/m<sup>2</sup> was also studied. The flexibility of the geobags were compared to the prototype geobag and previous studies (NHC 2010; Thompson et al. 2020a) (see Figure 3-2). The angle of flexibility was measured by hanging half the geobag from a flat surface and measuring the resulting angle to the horizontal surface. The dimensionless angle of flexibility ( $\phi$ ) and mass ( $m^*$ ) were made dimensionless by taking the ratio of the geobag variable to a prototype 125 kg geobag (Thompson et al. 2020a). The points circled in red correspond to the geobags used in this study, all other points are from Thompson et al. (2020a) and NHC (2010). It can be seen that the cloth bag with an 84% fill ratio had a more comparable angle of flexibility to the prototype 125 kg geobag than the remaining bags. The cloth bags had a higher dimensionless angle of flexibility than the geotextile bags, for the same fill ratios. Figure 3-3 shows the relationship between the dimensionless angle of flexibility and the fill ratio for the geotextile and cloth bags, respectively.



■ 0.83 x 0.60 m (Geotextile, 400 gm/m <sup>2</sup> ) Prototype	● 0.68 x 0.45 m (Geotextile, 400 gm/m <sup>2</sup> ) Prototype
▲ 0.40 x 0.31 m (Geotextile, 400 gm/m <sup>2</sup> ) Prototype	◆ 0.25 x 0.18 m (Geotextile, 200 gm/m <sup>2</sup> ) 1:7 Model Scale (Thompson et al. 2020a)
+ 0.29 x 0.21 m (Geotextile, 150 gm/m <sup>2</sup> ) 1:7 Model Scale (Thompson et al. 2020a)	● 0.18 x 0.14 m (Geotextile, 150 gm/m <sup>2</sup> ) 1:7 Model Scale (Thompson et al. 2020a)
▶ 0.18 x 0.14 m (Geotextile, 200 gm/m <sup>2</sup> ) 1:7 Model Scale (Thompson et al. 2020a)	▼ 0.15 x 0.10 m (Geotextile 150 gm/m <sup>2</sup> ) 1:7 Model Scale 1:7 (This Study)
● 0.18 x 0.14 m (Cloth, 80 gm/m <sup>2</sup> ) 1:7 Model Scale (Thompson et al. 2020a)	☆ 0.15 x 0.10 m (Cloth, 80 gm/m <sup>2</sup> ) 1:7 Model Scale (This Study)
☆ 0.15 x 0.10 m (Cloth, 80 gm/m <sup>2</sup> ) 1:7 Model Scale (Thompson et al. 2020a)	◆ 0.11 x 0.095 m (Cloth, 80 gm/m <sup>2</sup> ) 1:7 Model Scale 1:7 (Thompson et al. 2020a)
◆ 0.11 x 0.095 m (Cloth, 80 gm/m <sup>2</sup> ) 1:7 Model Scale 1:7 (Thompson et al. 2020a)	◀ 0.0475 x 0.0375 m (Cloth, 80 gm/m <sup>2</sup> ) 1:20 Model Scale 1:20 (NHC 2010)

Figure 3-2: Comparison of the dimensionless angle of flexibility and mass between scaled and prototype geobags.

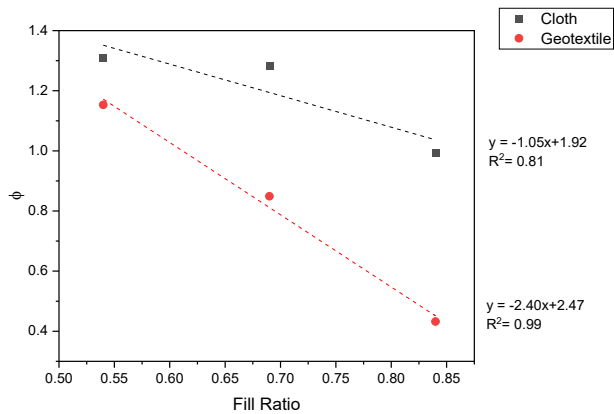


Figure 3-3: Relationship between the dimensionless angle of flexibility and the fill ratio.

The density of the geobags was measured by freezing the fully saturated geobags, then measuring the displaced water volume of the frozen geobags. The density was calculated as the ratio of the geobag mass to the displaced water volume. The geobags were filled with a fine sand ( $D_{50} = 0.27$  mm) with similar size and gradation to sand from the Brahmaputra River (Kumar et

al. 2014). The average density of all geobags in this study was 1725 kg/m<sup>3</sup> which is comparable to previous studies where Zellweger (2007) measured an average density of 1760 kg/m<sup>3</sup>, NHC (2010) measured an average density of 1778 kg/m<sup>3</sup> and Thompson et al. (2020a) measured an average density of 1718 kg/m<sup>3</sup>. The nominal thickness was taken as the thickness of the geobag if the filling sand were evenly distributed within the bag.

Table 3-1: Summary of characteristics of the six geobags studied

Bag	Bag Material	Fill Ratio [%]	Mass [kg]	Density [kg/m <sup>3</sup> ]	Nominal Thickness [m]
G1	Geotextile (150 g/m <sup>2</sup> )	54	0.234	1609	0.017
G2	Geotextile (150 g/m <sup>2</sup> )	69	0.299	1807	0.021
G3	Geotextile (150 g/m <sup>2</sup> )	84	0.364	1804	0.025
C1	Cloth (80 g/m <sup>2</sup> )	54	0.234	1716	0.014
C2	Cloth (80 g/m <sup>2</sup> )	69	0.299	1628	0.015
C3	Cloth (80 g/m <sup>2</sup> )	84	0.364	1788	0.022

### 3.2.3 Experimental Procedure

Three shapes were studied for each geobag (G1, G2, G3, C1, C2, C3): upstream heavy, even, and downstream heavy. The upstream heavy shape refers to a heavier distribution of sand in the upstream end of the geobag. The even shape refers to a balanced distribution of sand and downstream heavy shape refers to a heavier distribution of sand in the downstream section of the geobag. The distribution of sand was determined by measuring the thickness of the geobag at locations B-M, C-M and D-M from Figure 3-1c at the lowest flow velocity set point of the flume's pump (0.14 m/s).

Each geobag (see Table 3-1) and shape was subjected to increasing flow velocity set points until incipient motion was observed. The flow velocity set points were increased by approximately 0.05 m/s and held for 10 minutes. In this study, incipient motion was defined as when the geobag moved from one location to another (Thompson et al. 2020a). One of the challenges to this study was maintaining repeatability between the experiments since geobag shapes are deformable.

Although the initial shapes were consistent, the progression of shapes throughout the experimental runs was difficult to control. Therefore, at least three observations of incipient motion were made for each geobag and shape, and the average cross-sectional velocity was recorded. The average failure velocity across all observations was then determined for each series.

Once the failure velocities were determined, additional tests were performed to estimate the critical bed shear stresses, velocity profiles and changes to the geobag shapes. Due to the range in failure velocities, data was collected at a velocity set point as close to the failure velocity as possible (see Table 3-2 and Table 3-3 for complete list of series). The highest cross-sectional averaged velocity set points, 1.08 m/s, was limited by the capacity of the flume's pump.

At the velocity set-point just before failure, velocity profiles and local bed shear stresses were determined at measurement locations B-M, C-M and D-M (see Figure 3-1). For Series 5b and 11b from Table 3-2 and Table 3-3, respectively, the velocity profiles and local bed shear stress values were determined at all measurement locations shown in Figure 3-1c (A-M to E-R, inclusive) at an average flow velocity of  $\sim 0.50$  m/s to collect relevant contours of similarly shaped geobags. The flow velocity of 0.50 m/s was selected as the bag shapes were relatively consistent at this velocity which allows for a more direct comparison between the two bed configurations. Sideview photos were taken by a SONY DSLR camera at each velocity set-point to characterize the changes to the geobag shape.

The local bed shear stress was estimated using the turbulent kinetic energy (TKE) method (see Eq. 3-2), since the flow conditions at incipient motion for geobags are more likely complex and turbulent such that the TKE method may provide a better estimate compared to other methods

(i.e., universal law of the wall, Reynolds stress methods) (Biron et al. 2004; White et al. Submitted).

$$\tau_b = C_1 \frac{\rho_w}{2} (\langle u'^2 \rangle + \langle v'^2 \rangle + \langle w'^2 \rangle) \quad \text{Eq. 3-2}$$

where  $C_1$  is a proportionality constant,  $u'$  is the velocity fluctuation in the streamwise direction,  $v'$  is the velocity fluctuation in the transverse direction, and  $w'$  is the velocity fluctuation in the vertical direction. In turbulent flows,  $C_1$  is commonly calibrated by relating the shear stress estimated from the TKE method to the shear stress estimated from the Reynolds stress method (Soulsby 1983; Kim et al. 2000; Biron et al. 2004; Zhang et al. 2020). From Chapter 2,  $C_1$  was calibrated to be 0.30 for a single geobag on a rough surface.

To estimate local bed shear stresses via the TKE method (see Eq. 3-2) and collect vertical velocity profiles, time-averaged velocity and velocity fluctuations were measured with a Nortek Vectrino ADV (Model #: P 21363-1), at 100 Hz sampling rate. The vertical velocity profiles were collected by measuring the time-averaged velocity at 8-9 points above the geobag in increments of 1 – 3 cm (see Figure 3-1a). The ADV data was filtered to an average correlation > 70% and signal to noise ratio (SNR) > 15dB, as recommended by the manufacturer (Nortek 2018). Phase space thresholding was applied to the data as per Nikora and Goring (2000).

Table 3-2: Summary of single bag experiment series for the flat bed

Series	Initial Bag Shape	Bag	Average Cross-Sectional Flow Velocity Set Point (m/s)
1	a. Upstream Heavy	G1	0.71
	b. Even		0.61
	c. Downstream Heavy		0.49
2	a. Upstream Heavy	G2	0.77
	b. Even		0.72
	c. Downstream Heavy		0.60
3	a. Upstream Heavy	G3	0.92
	b. Even		0.76
	c. Downstream Heavy		0.74
4	a. Upstream Heavy	C1	0.71
	b. Even		0.76
	c. Downstream Heavy		0.71
5	a. Upstream Heavy	C2	0.85
	b. Even		0.86
	c. Downstream Heavy		0.96
6	a. Upstream Heavy	C3	0.97
	b. Even		1.06
	c. Downstream Heavy		1.06

Table 3-3: Summary of single bag experiment series for 1V:2H slope bed.

Series	Initial Bag Shape	Bag	Average Cross-Sectional Flow Velocity Set Point (m/s)
7	a. Upstream Heavy	G1	0.66
	b. Even		0.61
	c. Downstream Heavy		0.51
8	a. Upstream Heavy	G2	0.76
	b. Even		0.73
	c. Downstream Heavy		0.66
9	a. Upstream Heavy	G3	0.88
	b. Even		0.79
	c. Downstream Heavy		0.73
10	a. Upstream Heavy	C1	0.77
	b. Even		0.82
	c. Downstream Heavy		0.62
11	a. Upstream Heavy	C2	0.77
	b. Even		0.82
	c. Downstream Heavy		0.62
12	a. Upstream Heavy	C3	0.78
	b. Even		1.05
	c. Downstream Heavy		0.78

### 3.3 Results

#### 3.3.1 Incipient Motion

Incipient motion was observed for almost all series, apart from Series 5c, 6b, 6c and 12b, where the geobags remained stable at the highest flow velocity (as dictated by the flume's pump capacity). The average failure velocity, where the velocity is the average cross-sectional velocity, is shown in Figure 3-4 for all series. Notably, the geotextile bags G1, G2 and G3 experienced a consistent trend where incipient motion at higher velocities was observed for geobags with an upstream heavy shape compared to geobags with an even shape. Incipient motion was observed for the downstream heavy shape at the lowest velocities for G1, G2 and G3. The geotextile bags with higher fill ratios (G3) also had better stability than the geotextile bags with lower fill ratios. These trends are consistent for both the flat bed series and the 1V:2H bed series.

The cloth bags did not experience consistent shape progressions (i.e., the internal sand movement was inconsistent such that bags with same initial shapes did not always result in the same final shapes) throughout the experiment runs, and as such there is no clear trend between the failure velocities and initial bag shape. In some cases, the cloth bags did not fail even at the highest achievable flow velocity. The cloth bags, C2 and C3, with a downstream heavy shape did not fail on the flat bed, and the cloth bag C3 with an even shape did not fail on either the flat bed or 1V:2H sloped bed.

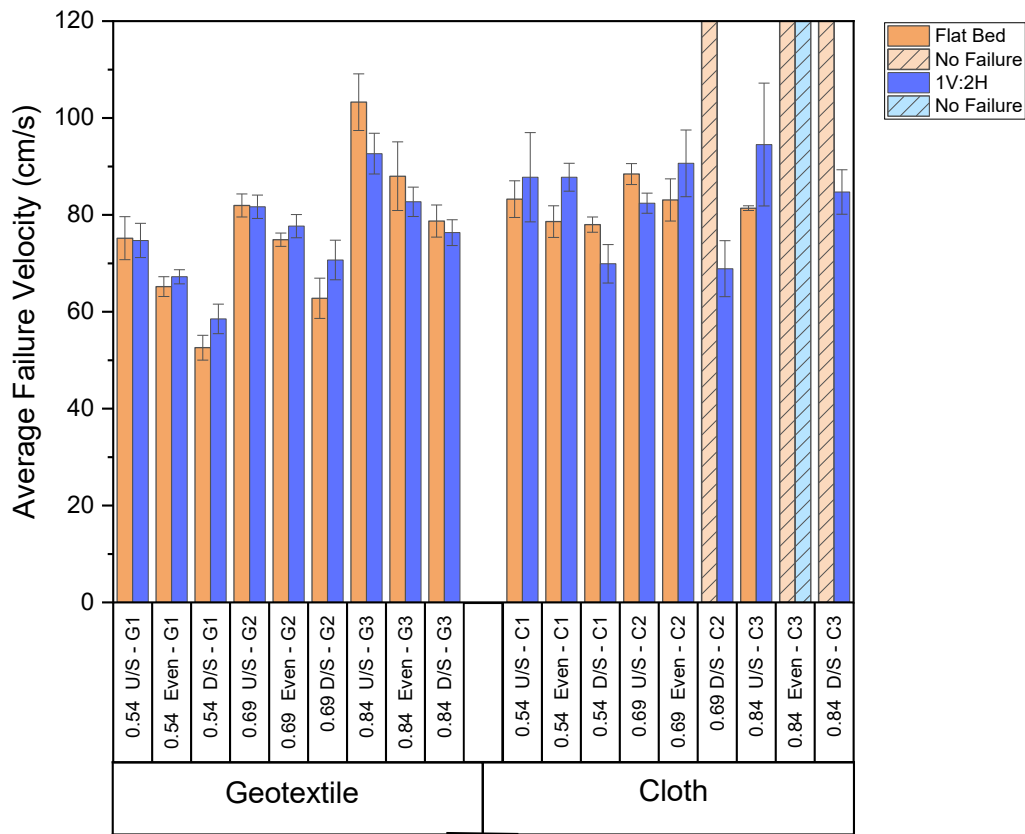


Figure 3-4: Comparison of the average failure velocity for each series. Error bars indicate the standard deviations.

In eight of the eighteen cases, the same geobag and shape was more stable on the 1V:2H slope bed configuration compared to the flat bed configuration for both geotextile and cloth bags. For the geotextile bags, this occurs at the lower fill ratios, whereas the cloth bags experienced this at all three fill ratios. For the cloth bags, the variation in failure velocity on the 1V:2H slope bed was greater than the geotextile bags, which may be attributed to their inconsistent shape progressions. On the 1V:2H slope bed, the gravity force pushes the geobag towards the bottom of the slope while the drag force acts in the direction of flow. This caused the geobags to fail by both flipping over with the direction of flow and twisting towards the slope bottom.

### 3.3.2 Critical Bed Shear Stresses

The critical local bed shear stresses were estimated at the velocity set point closest to the average failure velocity at measurement locations B-M, C-M and D-M for all experiment series (see Figure 3-5). The critical local bed shear stresses varied at the different measurement locations and appeared to be influenced by the geobag and bed characteristics. Geobags with an upstream heavy shape observed a higher average and standard deviation of critical bed shear stresses ( $\tau_b = 3.45 \pm 5.02$  Pa) than the geobags with a downstream heavy shape ( $\tau_b = 1.89 \pm 2.31$  Pa) and even shape ( $\tau_b = 1.52 \pm 1.14$  Pa). In some cases, the critical local bed shear stresses estimated for the same geobag and shape were higher on the 1V:2H sloped bed compared to the flat bed. These cases tend to correspond to when the geobag failed at a higher average flow velocity on the 1V:2H sloped bed compared to the flat bed. For example, the critical local bed shear stresses estimated for the cloth bag, C3, with the upstream heavy and even shapes were higher on the 1V:2H slope bed compared to the flat bed. In the case of the upstream heavy shape, the C3 geobag failed at a higher average velocity on the 1V:2H sloped bed compared to on the flat bed.

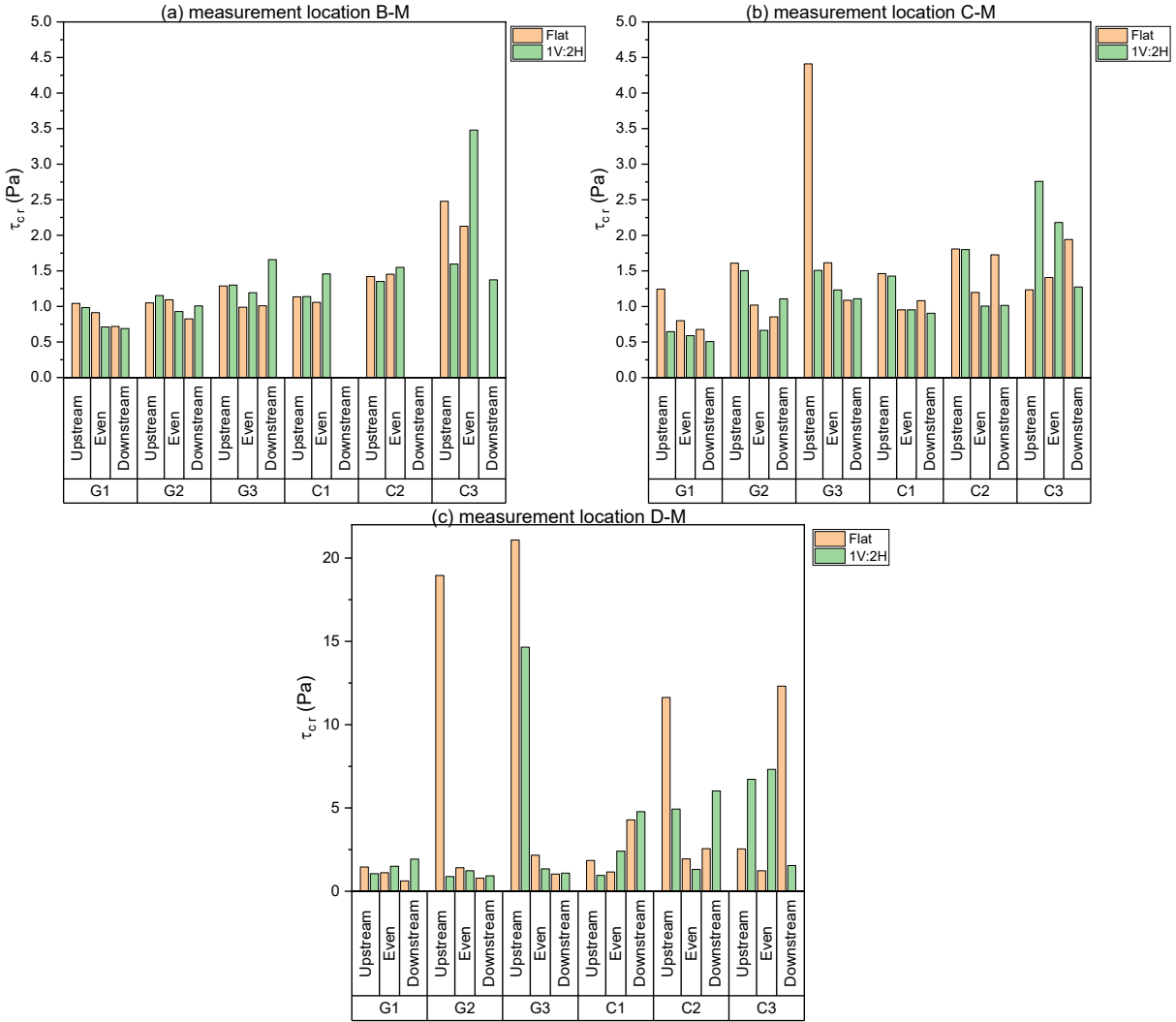


Figure 3-5: Summary of the local critical bed shear stresses estimated at measurement location (a) B-M, (b) C-M, and (c) D-M, for all experiment series.

### 3.3.3 Contour Analysis

Contours were created from the local bed shear stress values and mean near-bed velocities for the cloth bag C2 with an even shape on both the flat and 1V:2H slope bed configurations (i.e., Series 5b and 11b) at an average flow velocity of 0.50 m/s (see Figure 3-6). As the local shear stress values were estimated by the TKE method, greater shear stress values indicate greater turbulence, and may indicate the presence of a near-wake flow where there is greater vorticity (Dey et al. 2011). In the flat bed series, Series 5b, flow separation and re-attachment appears to

occur downstream of the geobag. At location D-M, a bed shear stress of 0.81 Pa was estimated, and at location E-M the maximum bed shear stress (= 1.86 Pa) was estimated. This indicates a similar pattern to a dune bedform, where in Fernandez et al. (2006), the highest Reynolds stress estimates were located downstream of the dune crest near a flow reattachment point. As the geobag was relatively flat, the flow separation and reattachment are expected to occur downstream of the geobag where the surface elevation drops from the bag to the bed. The mean near-bed velocity contours indicate a wake-form at the downstream end of the geobag. In Series 11b, the contours are affected by the bed slope such that the highest bed shear stress value is located at location E-L, which corresponds to the downstream corner closest to the bottom end of the slope. This reflects the direction of the observed failure mechanism for geobags on the sloped bed.

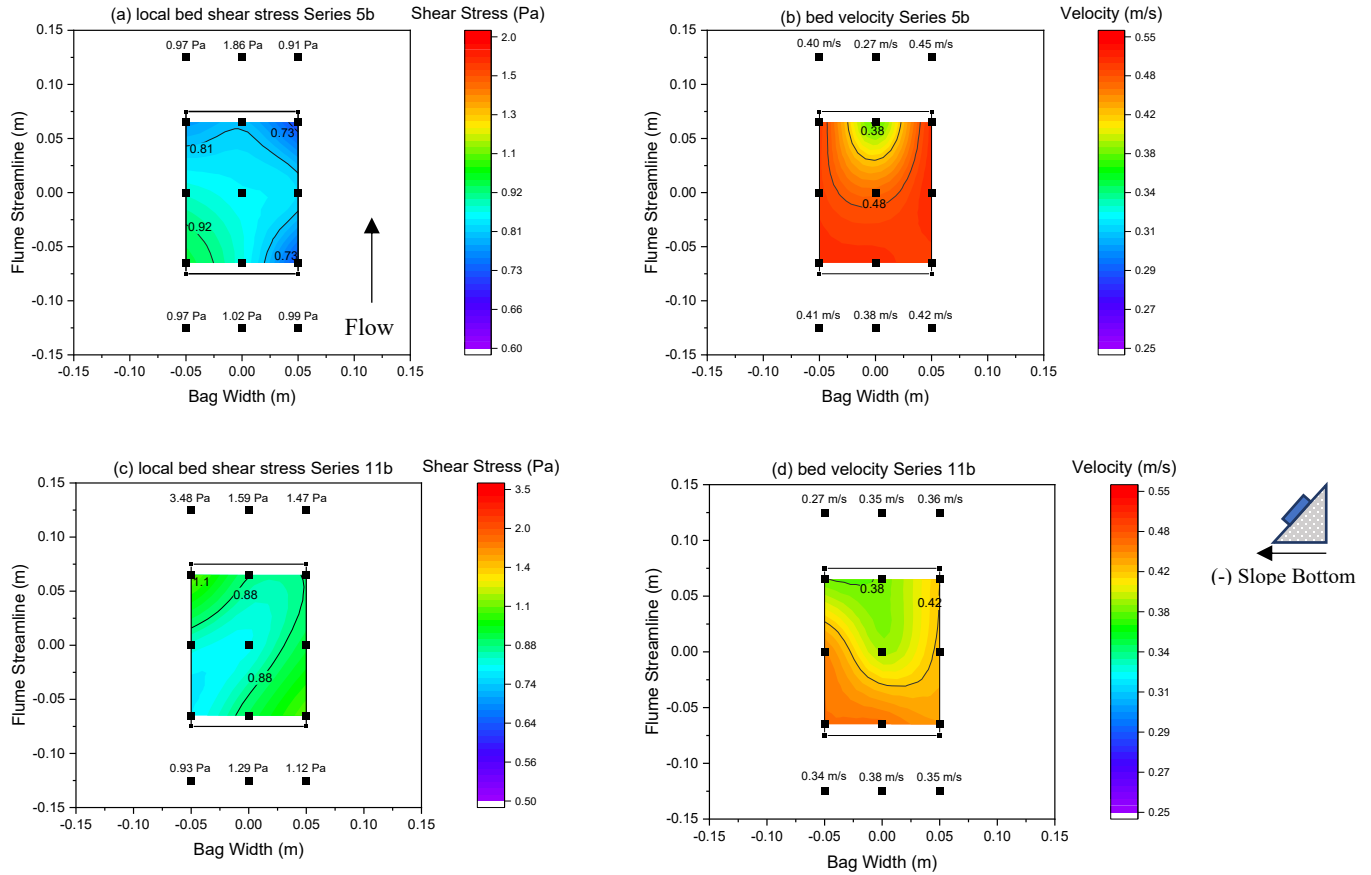


Figure 3-6: Contours of the local bed shear stress and near-bed streamwise velocity for (a-b) Series 5b (flat bed, even initial shape), and (c-d) Series 11b (1V:2H sloped bed, even initial shape), at an average flow velocity of 0.50 m/s. The square points represent the measurement locations, and the rectangle represents the geobag.

### 3.3.4 Critical Shields Parameter

The critical Shields parameters for all series are shown in Figure 3-7 with respect to the boundary Reynolds number ( $= u_{cr}^* d_n / \nu$ , where  $u_{cr}^* = \sqrt{\tau_{cr} / \rho}$ ). The critical Shields parameters ranged from 0.0018 to 0.019 for both the flat and 1V:2H slope bed cases. This is significantly lower than the critical Shields parameter obtained by Thompson et al. (2020b), which was estimated to be 0.09. In Thompson et al. (2020b), the test section was made up of hundreds of geobags to simulate a revetment structure which resulted in higher contact forces between geobags and therefore higher stability. Furthermore, they defined incipient motion as when 5% of bags had moved. This may explain the different Shields parameters, where in this study the

single geobag has lower contact forces and the incipient motion was defined as when the single bag had moved. Gogus and Defne (2005) studied a single solid particle similarly to this study, and their data is more comparable. The critical Shields parameters from Gogus and Defne (2005) are slightly smaller than the critical Shields parameters from this study, which is likely due to their larger size ( $d_n = 0.062$  m) and higher density (approx.  $1960$  kg/m<sup>3</sup>).

It is clearly observed that geobags of the same dimensions, fill ratio and bag materials, but with different initial shapes and bed slopes, have different critical Shields parameters and boundary Reynolds numbers. The critical Shields parameters for each initial shape were:  $\psi = 0.011 \pm 0.007$  ( $\psi = \text{average} \pm \text{standard deviation}$ ) for even shapes,  $\psi = 0.024 \pm 0.03$  for the upstream heavy shapes, and  $\psi = 0.015 \pm 0.018$  for the downstream heavy shapes. Gogus and Defne (2005) obtained a similar result in their observations of irregularly shaped solitary rocks, as did Shields (1936) in their observations of angular versus rounded grains, where objects with the same effective diameter yet different shapes resulted in different critical Shields parameters.

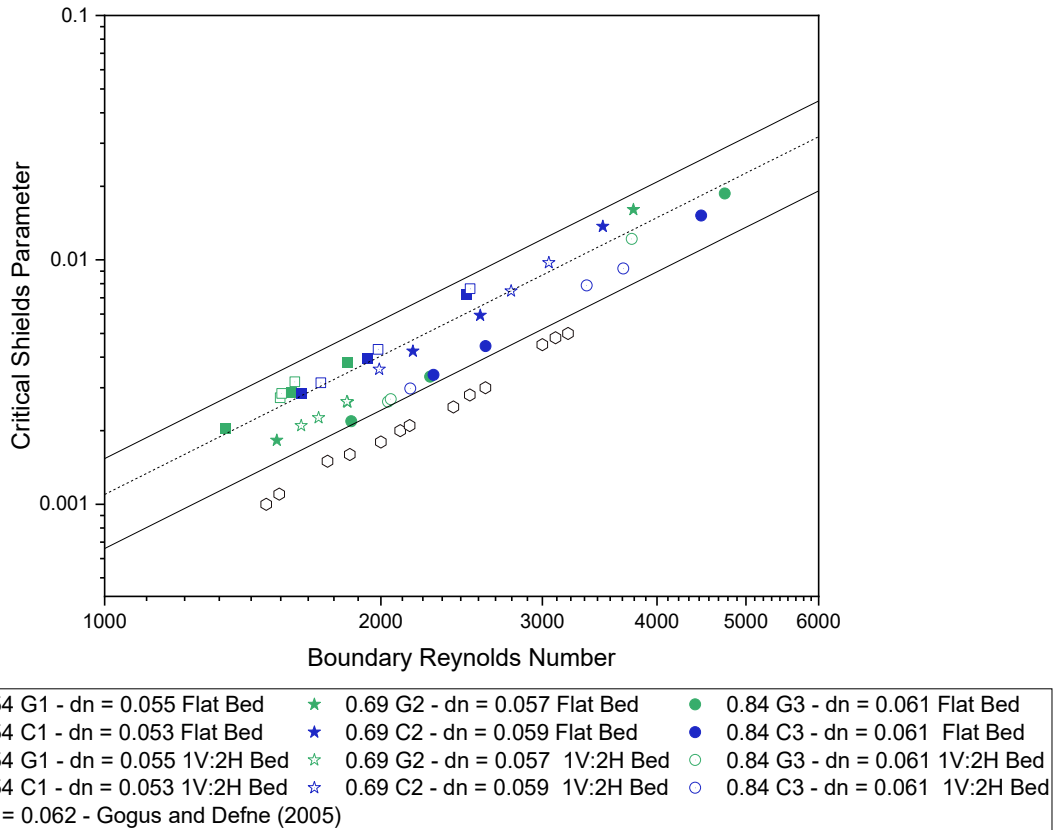


Figure 3-7: Relationship between the critical Shields parameter and boundary Reynolds number for all series. The dashed line represents the line of best fit ( $y = x^2$ ), and the two solid lines represent the upper and lower bounds ( $\pm 30\%$ ).

## 3.4 Discussion

### 3.4.1 Fill Ratio

The results obtained from measuring the critical velocity demonstrate that geobags with higher fill ratios tend to be more stable than geobags with lower fill ratios. The critical Shields parameters does not necessarily reflect this observation (see Figure 3-7). This may be because the Shields formula incorporates the particles characteristic size (see Eq. 3-1; Shields 1936), which is indirectly related to the fill ratio. However, the characteristic size does not consider the impact of the geobags flexibility on the critical Shields parameter, nor does it consider the void space within the geobag, both of which are impacted by the fill ratio.

The literature (i.e., Grune et al. 2007; Pilarczyk 2000; Thompson et al. 2020a) has also observed that stability improves with increasing fill ratios, and Pilarczyk (2000) and Thompson et al. (2020a) suggest that a fill ratio of ~80% is most stable in a revetment structure. Thompson et al. (2020a) attributed this trend to the geobag's internal sand movement, where geobags with higher fill ratios observe less internal sand movement than those with lower fill ratios. Internally, the sand will move towards the downstream end of the bag with the direction of flow, thus changing the bag's shape and creating an opportunity for the upstream end of the bag to lift. This allows the lift force to play a stronger role in the incipient motion of the bag. This may explain why the failure velocities for the geotextile bags with higher fill ratios was higher than the bags with lower fill ratios. It also explains why the cloth bags from Series 6b and 12b did not fail, as these bags had the highest fill ratios. As a single size of bags was used in this study, a higher fill ratio corresponded to higher mass, which also attributed to higher stability. However, the cloth bags observed a variable trend which may be attributed to other factors such as the flexibility of the bag material and its impact on the bag shape and internal sand movement at different flows.

### 3.4.2 Bag Material

From visual observations, the geotextile bags had a consistent shape progression throughout the experiment runs which is likely due to their relatively high stiffness compared to their cloth bag counterparts. In Figure 3-8, photos of the geotextile bags at the highest velocity set point prior to failure are shown. The photos demonstrate that the geobags have begun to lift from the approaching flow, whereas the cloth bags in the same cases either compressed or folded in on themselves (see Figure 3-9). This suggests that the lift force played a greater role in the geotextile bag failures.

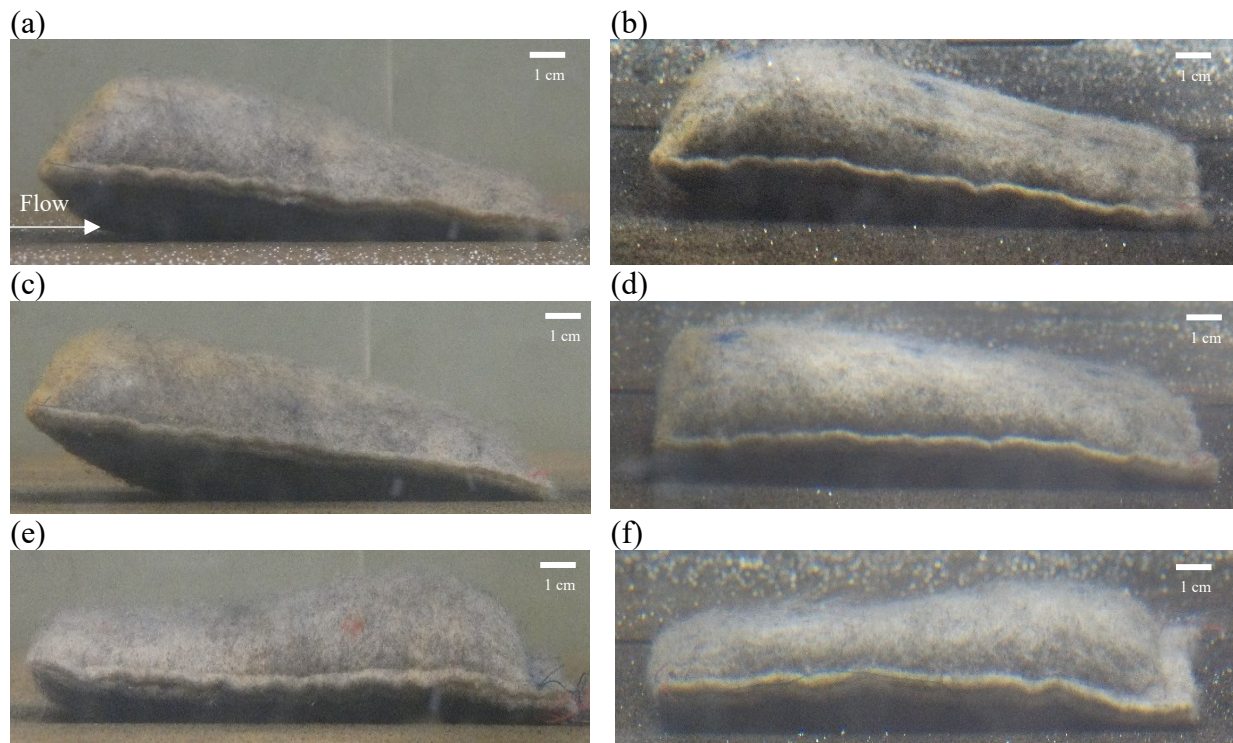


Figure 3-8: Sideview photos of geotextile geobags at their highest velocity set-points before failure for flat bed configurations (a, c, e) and 1V:2H slope bed configurations (b, d, f), for (a) Series 3a (G3 upstream heavy), (b) Series 9a (G3, upstream heavy), (c) Series 3b (G3 even), (d) Series 9b (G3 even), (e) Series 2c (G2 downstream heavy), (f) Series 8c (G2 downstream heavy). Flow is from left to right.

The cloth bags did not demonstrate consistent shape progressions throughout the experiment runs. This may be caused by the relatively higher flexibility of the C1, C2 and C3 geobags compared to their geotextile counterparts, as well as the potential for internal sand movement. In Series 5c and 6c (downstream heavy shapes for geobags C2 and C3), the geobags remained stable at the highest possible velocity, which may be specifically caused by the upstream section of the cloth bags folding on top of itself (see Figure 3-9e), thus restricting the internal movement of sand in the bag. As a result, the effective volume of the cloth bag reduced such that the fill ratio effectively increased. The same cases for the sloped bed (Series 11c and 12c, downstream heavy shapes for geobags C2 and C3) observed failure, where the bags did not compress on

themselves as much as the cloth bags on the flat bed (see Figure 3-9f). In Series 6b and 12b, the geobag (C3) did not fail. This can be explained by a restriction of internal sand movement in the bag because of the higher fill ratio of sand. Also, the even sand distribution of the initial shapes resulted in the final sand distribution being heavier in the center of the bag (see Figure 3-9c and Figure 3-9d).

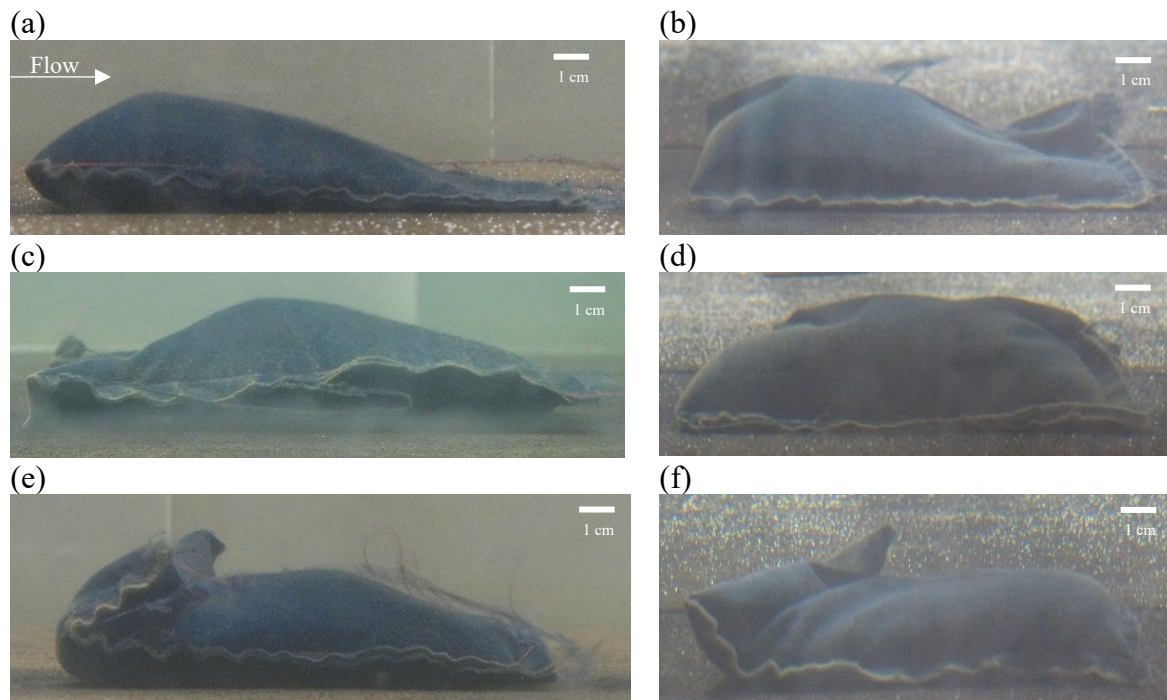


Figure 3-9: Sideview photos of cloth geobags at their highest velocity set points before failure for flat bed configurations (a, c, e) and 1V:2H slope bed configurations (b, d, f), for (a) Series 5a (C2, upstream heavy), (b) Series 11a (C2, upstream heavy), (c) Series 6b (C3, even), (d) Series 12b (C3, even), (e) Series 5c (C2, downstream heavy), (f) Series 11c (C2, downstream heavy).

From Figure 3-7, it appears that in most cases, the cloth bags have higher critical Shields parameters and therefore higher stability compared to the geotextile bags. Overall, cloth bags failed at velocities that were on average 0.45 m/s higher than geotextile bags in both flat and 1V:2H slope bed configurations. This suggests that the bag material impacts the stability of the geobags. In the section above, the fill ratio was also identified to influence the geobag's stability, such that a more flexible bag material combined with a higher fill ratio is a more stable geobag.

### 3.4.3 Geobag Shapes

As shown in Figure 3-5, the geobags with initial upstream heavy shapes observed the highest average and range in critical bed shear stresses compared to the geobags with initial downstream heavy and even shapes. This trend is likely due to the location and height of the crest (highest elevation) on the geobags. At the critical point just before failure, the crest was typically located at the upstream measurement location, B-M, for geobags with an initial upstream heavy shape (see Figure 3-1c for measurement locations). The location of this crest resulted in higher critical bed shear stresses at location D-M (see Figure 3-5c) for most of the upstream heavy cases.

Downstream of the crest, flow separation occurs such that the bed shear stresses increase nearer to and downstream of the flow reattachment point (Dey et al. 2011; Fernandez et al. 2006).

Similar shapes, such as dune bed forms, have demonstrated this phenomenon (Fernandez et al. 2006), where the lowest shear stress was estimated on top of the crest and the highest shear stress at a point downstream that correlated to the flow reattachment point.

Upstream heavy cases that did not observe a higher bed shear stress at location D-M include cloth bag C3 on the flat bed, cloth bag C1 on the 1V:2H slope bed and geotextile bags G1 and G2 on the 1V:2H slope bed. In the flat bed configuration, cloth bag C3 changed shape at the highest velocity set-point where the sand appeared to shift towards the downstream end of the bag (see Figure 3-10), thus shifting the location of the geobags crest to location C-M. This explains why the local bed shear stress estimated at location C-M was lowest ( $= 1.23 \text{ Pa}$ ; see Figure 3-5b). This also explains why the local bed shear stress estimated at location D-M ( $= 2.54 \text{ Pa}$ ) was not significantly higher than at location B-M ( $= 2.48 \text{ Pa}$ ), as the crest shift also changes the location of the flow separation and reattachment points. In the 1V:2H slope bed configurations, the geobags with lower sand fill ratios (i.e., G1, G2 and C1) also did not observe

higher local bed shear stresses in the downstream location of D-M. This may be caused by both the shapes and the bed configuration. The location of the crest appeared to shift from the centerline of the geobag towards the bottom end of the slope, effectively reducing the height of the crest along the centerline. The measurements were taken along the centerline of the geobag and were thus less affected by the crest's location. For the geobags with lower fill ratios, the crest may shift more easily due to higher potential for internal sand movement.

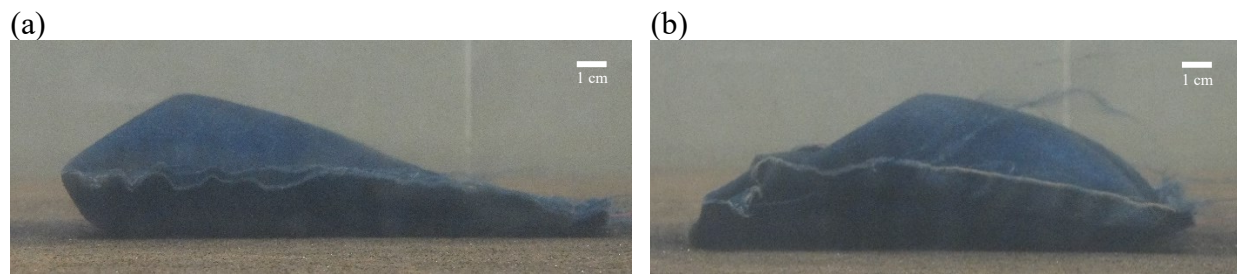


Figure 3-10: Geobag shape change between the last two velocity set-points for Series 6a (C3, upstream heavy) at (a) velocity set point of 0.87 m/s, (b) velocity set point of 0.97 m/s.

The geobags with even shapes observed very little difference between the local critical bed shear stresses estimated at the three measurement locations, compared to the geobags with upstream or downstream heavy shapes. This is due to the relatively flat shape of these geobags. At the higher velocity set points before failure, the overall bag shape changed such that sand moved towards the downstream end and/or bottom end of the slope, depending on the bed configuration.

However, the shape change was not drastic enough to create large crests, thus the critical local bed shear stresses remained relatively unaffected. The critical local bed shear stresses, and thus critical Shields parameters ( $\psi = 0.011 \pm 0.007$ ), were also smaller than the two other shapes (upstream heavy shapes:  $\psi = 0.024 \pm 0.03$ ; downstream heavy shapes:  $\psi = 0.015 \pm 0.018$ ) suggesting that lift force played a larger role in their incipient motion (Buffington and Montgomery 1997).

The geobags with downstream heavy shapes had variable shape progressions depending on the bag material. Initially, the downstream heavy shape geobags had a crest at location D-M, such that there was no flow separation or reattachment points near any of the measurement locations. The geotextile bags did not experience significant shape changes, and their local critical bed shear stresses estimated at B-M, C-M and D-M remained comparable throughout the experiment series. The cloth bags however, tended to have higher critical Shields parameters at the downstream D-M location at the highest velocity set-point. This was due to the upstream section of the bag folding on top of itself, thus creating a higher elevation at the upstream point, i.e., a crest (see Figure 3-9e-f). This peak elevation caused flow separation and reattachment points downstream of it, such that a higher local bed shear stress was estimated at location D-M. The cloth bag C3 in Series 12c, on a 1V:2H slope bed configuration, did not observe this trend because the upstream section of the bag did not fold in on itself in this case. This was likely due to the higher fill ratio of sand in C3 restricting the internal sand movement.

#### 3.4.4 Bed Configuration

In almost half of the cases, the same geobags and shapes failed at a higher average velocity on the 1V:2H sloped bed than the flat bed (see Figure 3-4), indicating a higher stability. The critical Shields parameters (see Figure 3-7) reflect this trend for these cases as well. This trend is counterintuitive, because additional gravitational forces would be expected to reduce the stability and therefore the critical Shields parameters (Recking 2009; Prancevic and Lamb. 2015); however, much of the literature has observed similar results. Thompson et al. (2020a) observed that placed geobags (placed side-by-side) were typically more stable on a 1V:2H slope than a flat bed while geobags that were dropped (i.e., dropped from surface of water) were less stable on the 1V:2H slope. Khajenoori et al. (2021) observed that steeper slopes (i.e., 1V:3H vs 1V:1.5H)

resulted in higher stability. Both Thompson et al. (2020a) and Khajenoori et al. (2021) studied beds made up of many geobags rather than a single bag, where the slopes were perpendicular to the flow direction similar to this study. Shields (1936), and many others (e.g., Buffington and Montgomery 1997; Mueller et al. 2005) observed that critical Shields parameters increased with increasing slopes when the slopes were parallel to the flow direction. Much of the literature has attempted to explain this counterintuitive trend (e.g., Buffington and Montgomery 1997; Schvidchenko and Pender 2000; Gogus and Defne 2005; Recking 2009; Zimmerman et al. 2010; Prancevic and Lamb 2015), and have attributed it to bed form drag, relative depth, particle interlocking and sidewall effects. Prancevic and Lamb (2015) were able to isolate for bed slope and relative roughness in their study and determined that the critical Shields parameter does not correlate to bed slope consistently and is rather a function of the relative roughness, which happens to be influenced by the bed slope. In this study, only eight of the eighteen cases experienced higher stability on the 1V:2H slope, indicating that bed configuration alone does not correlate to critical Shields parameters or stability. It is more likely that the combination of geobag characteristics (i.e., the fill ratio, bag material and bag shape) and bed configurations (i.e., bed slope and relative roughness) impact stability.

#### 3.4.5 Shape Factor of Geobag

A shape factor was proposed to determine the relationship between shape and stability, which can be quantified either by the critical Shields parameter or critical velocity. Gogus and Defne (2005) defined a shape factor for irregularly shaped particles by comparing the particle shape to a rectangular prism containing the particle (see Figure 3-11). They introduced two dimensionless terms which describe the relative length of the particle (see Eq. 3-3) and relative volume of the particle (see Eq. 3-4).

$$\left(\frac{a+b}{2c}\right) \quad \text{Eq. 3-3}$$

$$\left(\frac{\forall}{abc}\right) \quad \text{Eq. 3-4}$$

where  $a$  is the width of the rectangular prism,  $b$  is the height of the rectangular prism and  $c$  is the length of the rectangular prism in Figure 3-11.  $\forall$  is the measured volume of the object. Gogus and Defne (2005) compared the shape factor to that of a cube, which is why the denominator in Eq. 3-3 is  $2c$  to ensure the cubic shape factor was equal to unity.

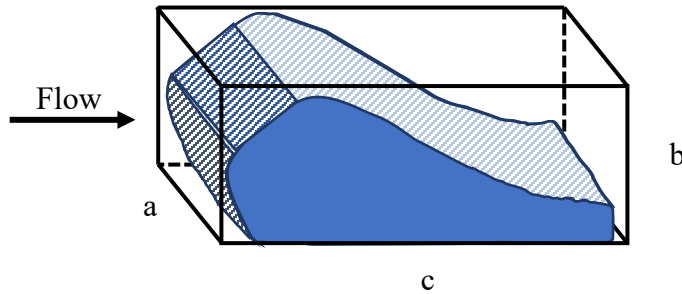


Figure 3-11: Rectangular prism containing an irregularly shaped object, i.e., a geobag.

The fill ratio of the geobag was included in the shape factor, as it represents the potential for internal sand movement. The shape factor of a geobag,  $SF_G$ , is defined as:

$$SF_G = FR^3 \cdot \phi^{0.6} \cdot \left(\frac{a+b}{2c}\right) \cdot \left(\frac{\forall}{abc}\right)^{\frac{1}{3}} \quad \text{Eq. 3-5}$$

where, FR is the fill ratio of the geobag (i.e., 54 %, 69 % or 84 %). The angle of flexibility was included to consider the impact of the bag material in the shape factor, although it should be noted that this term is also related to the fill ratio (see Figure 3-3). The relative length and volume of the geobag are also indirectly related to the fill ratio of the geobag, where higher fill ratios result in a greater measured volume and thickness. All the terms were raised to the power

of an arbitrary value which was calibrated using the data from this study. In Figure 3-12, the critical cross-sectional average velocity is plotted against the proposed shape factor.

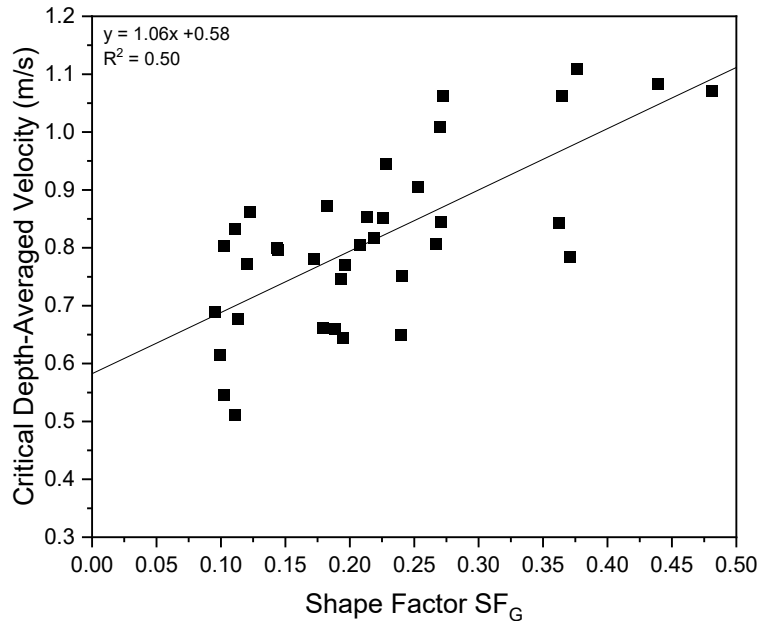


Figure 3-12: Relationship between the critical depth-averaged velocity with the shape factor,  $SF_G$ , for all experiment series.

The stability of the geobag increases with increasing shape factors, although the correlation is relatively weak ( $R^2 = 0.50$ ). Based on the calibration of  $SF_G$ , the fill ratio has the highest impact on the geobags stability, such that higher fill ratios result in higher stability. This result supports the literature, where many studies have determined that element stability increases with increasing fill ratios (Pilarczyk 2000; Grune et al. 2007; Thompson et al. 2020a). The weak correlation between the shape factor and critical depth-averaged velocity may be explained by the exclusion of parameters such as bed configuration and relative roughness.

From the analyses above, it has been suggested that the geobag stability is influenced by a shape factor, the bed configuration and relative roughness. The stability, represented by the critical depth-averaged velocity, can thus be written as function of these variables:

$$V_{cr} = \text{fcn} \left( (SF_G)^k \cdot (K_s)^m \cdot \left( \frac{d_n}{R_h} \right)^n \right) \quad \text{Eq. 3-6}$$

where fcn is a function,  $V_{cr}$  is the critical depth-averaged velocity,  $SF_G$  is the shape factor,  $K_s$  is a slope factor ( $= \sqrt{1 - \left( \frac{\sin^2 \theta}{\sin^2 \vartheta} \right)}$ , where  $\theta$  is the angle of the slope to the horizontal, and  $\vartheta$  is the angle of repose of the elements taken as  $40^\circ$ ; Pilarczyk 2000),  $R_h$  is the hydraulic radius. Each variable was raised to an arbitrary power,  $k$ ,  $m$  and  $n$ , which was then calibrated with the critical depth-averaged velocity to be 0.5, 0.6, and -0.1, respectively. The best result is presented in Figure 3-13.

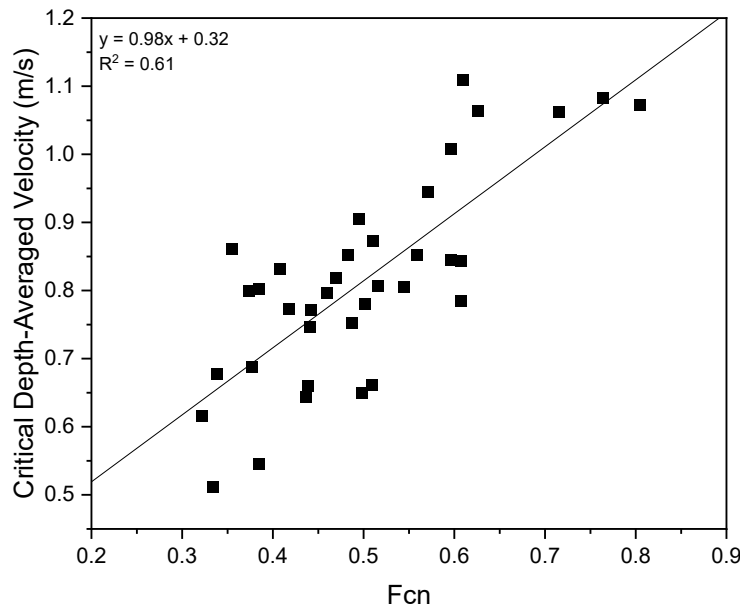


Figure 3-13: Relationship between the critical depth-averaged velocity with the shape factor, slope factor and relative depth, for all experiment series.

The shape factor and side-slope factor have a greater impact (higher power value) on the geobag stability than the relative roughness. The positive trendline in Figure 3-13 also suggests that lower slope factors would reduce the geobag stability, where a lower slope factor physically represents steeper revetment slopes. Both the Pilarczyk (2000) and USACE (1994) revetment design formulas suggest that steep revetment slopes result in lower stability, thus requiring larger sized elements. Higher relative roughness also suggest lower stability. Physically, this means that higher flow depths for equal particle diameters would require higher velocities to undergo incipient motion. Gogus and Defne (2005), Schvidchenko and Pender (2000) obtained a similar result, where the boundary Reynolds number increased with increasing relative depths. The correlation between the critical depth-averaged velocity and the function is stronger ( $R^2 = 0.61$ ) than the correlation between the critical depth-averaged velocity and the shape factor ( $R^2 = 0.50$ ); however, the correlation is still relatively weak. The correlations may be improved by conducting more tests with the isolated variables, and by including more variables altogether. However, one drawback to including many variables in Eq. 3-5 and Eq. 3-6 is that the equations may not be applicable for varying experimental conditions and are thus not very practical.

The critical Shields parameter is a function of the boundary Reynolds number, element density and size. As per Shields (1936), the critical Shields parameter should be proportional to the squared boundary Reynolds number. In Figure 3-7, the critical Shields parameter correlates to the squared boundary Reynolds number well ( $R^2 = 0.91$ ). When the shape factor from Eq. 3-5 is applied to the critical Shields parameter, the correlation improves to  $R^2 = 0.97$  (see Figure 3-14). This further suggests that the critical Shields parameter is a function of the shape factor.

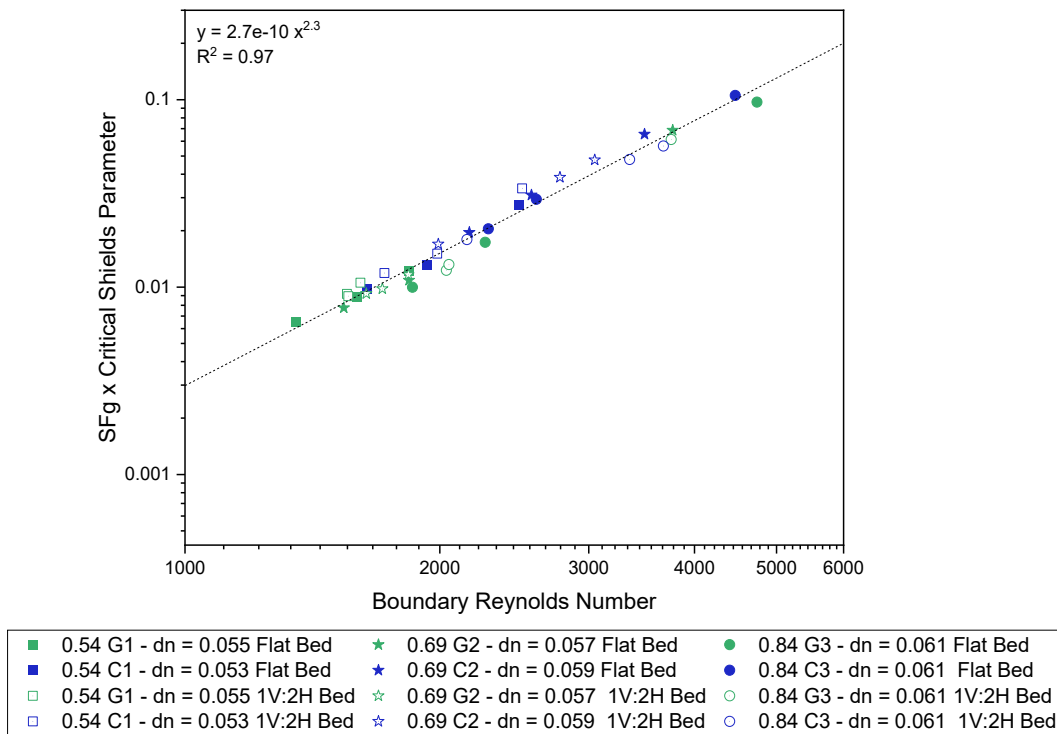


Figure 3-14: Relationship between critical Shields parameter and boundary Reynolds number, with an applied shape factor. The dashed line represents the line of best fit ( $y = x^2$ ).

### 3.5 Conclusion

The conditions at incipient motion were studied for a single geobag, with varying shapes, fill ratios, bag materials and side slopes. First, the point at which the geobag underwent incipient motion was determined. The local bed shear stresses, velocity profiles were then determined at a velocity set points near the average cross-sectional velocity corresponding to incipient motion. The effect of geobag characteristics and bed configuration were then analysed to determine their impact on the geobag's stability. A summary of results is presented below.

- Geotextile bags observed a consistent shape progression throughout the experimental runs, where the internal sand movement was relatively similar for bags with the same initial shapes. Therefore, a clear trend was observed in failure velocities with respect to

the initial bag shape. Upstream heavy shapes were most stable and downstream heavy shapes were least stable.

- Cloth bags did not observe a clear trend due to the variability in their shape progressions throughout the experimental runs. This has been attributed to their relatively high flexibility compared to their geotextile counterparts.
- The range of local critical Shields parameters estimated at locations B-M, C-M and D-M varied between geobag shapes: upstream heavy shape geobags observed the largest range  $\psi = 0.024 \pm 0.03$ , downstream heavy shape geobags observed the second largest range  $\psi = 0.015 \pm 0.018$ , and the even shape observed the lowest range  $\psi = 0.011 \pm 0.007$ . This indicates that the upstream heavy shapes were most stable on average, and the even shapes were least stable on average.
- A shape factor has been proposed to improve the understanding of the relationship between the geobag stability and geobag characteristics. When the shape factor is applied to the critical Shields parameters, the correlation between the boundary Reynolds number improves.
- Overall, a higher fill ratio combined with a more flexible bag material increases the stability of the geobag. The geobag shape, geobag fill ratio, bed slope and relative depth all influence the stability of the geobag to a certain degree.

For future research considerations, it would be beneficial to perform more tests with more variations of fill ratios and shapes to validate the relationship between geobag stability and the proposed shape factor. As local bed shear stress values can widely vary due to the random nature of turbulence, future studies should also consider obtaining local bed shear stress estimates at many locations. Furthermore, the data from these single geobag tests are useful for validating a

CFD model, which will have the capability to model the forces acting on the geobags with more detail.

### 3.6 References

- Akter, A., Pender, G., Wright, G. & Crapper, M., 2013. Performance of a Geobag Revetment I: Quasi-Physical Modeling. *Journal of Hydraulic Engineering*, 139(8), pp. 865-876.
- Bangladesh Water Development Board, 2010. *Guidelines for Riverbank Protection. Jamuna-Meghna River Erosion Protection Project*, Bangladesh: s.n.
- Bezuijen, A. & Vastenbunrg, E., 2013. *Geosystems. Design Rules and Applications*. 1st ed. London: Taylor & Francis Group.
- Biron, P. M., Robson, C., Lapointe, M. F. & Gaskin, S. J., 2004. Comparing different methods of bed shear stress estimates in simple and complex flow fields. *Earth Surface Processes and Landforms*, Volume 29, pp. 1403-1415.
- Buffington, J. M. & Montgomery, D. R., 1997. A systematic analysis of eight decades of incipient motion studies, with special reference to gravel-bedded rivers. *Water Resources Research*, 33(8), pp. 1993-2029.
- Chow, V. T., 1959. *Open-Channel Hydraulics*. 1st ed. Tokyo: McGraw-Hill Book Company.
- Dey, S. et al., 2011. Wall-wake flows downstream of a sphere placed on a rough wall. *Journal of Hydraulic Engineering*, 137(10), pp. 1173-1189.
- Fernandez, R., Best, J. & Lopez, F., 2006. Mean flow, turbulence structure, and bed form superimposition across the ripple-dune transition. *Water Resources Research*, Volume 42, pp. 1-17.
- Gogus, M. & Defne, Z., 2005. Effect of Shape on Incipient Motion of Large Solitary Particles. *Journal of Hydraulic Engineering*, 131(1), pp. 38-45.
- Grune, J. et al., 2007. *Stability tests of geotextile sand containers for monopile scour protection*. San Diego, 30th. International Conference on Coastal Engineering (ICCE 2006).
- Heibaum, M., 2014. Geosynthetics for Waterways and Flood Protection Structures- Controlling the Interaction between Water and Soil. *Geotextiles and Geomembranes*, Volume 42, pp. 374-393.
- Heibaum, M., Oberhagemann, K., Faisal, M. & Haque, S., 2008. *Geotextile bags for sole permanent bank protection*. Edinburgh, 4th European Geosynthetics Conference.
- Hornsey, W. P., Carley, J. T., Coghlan, I. R. & Cox, R. J., 2011. Geotextile sand container shoreline protection systems: Design and application. *Geotextiles and Geomembranes*, Volume 29, pp. 425 - 439.

- Khajenoori, L., Wright, G. & Crapper, M., 2021. Laboratory Investigation of Geobag Revetment Performance in Rivers. *Geosciences*, 11(304).
- Kim, S.-C., Friedrichs, C. T., Maa, P.-Y. & Wright, L. D., 2000. Estimating bottom stress in tidal boundary layer from acoustic doppler velocimeter data. *Journal of Hydraulic Engineering*, 126(6), pp. 399-406.
- Korkut, R. et al., 2007. Geobag Performance as Scour Countermeasure for Bridge Abutments. *Journal of Hydraulic Engineering*, 133(4), pp. 431-439.
- Kumar, S. S., Krishna, A. M. & Dey, A., 2014. *Dynamic soil properties of Brahmaputra sand using Cyclic Triaxial tests*. Guwahati, Assam, North East Students Geo-Congress on Advances in Geotechnical Engineering.
- Moreira, A., Vieira, C., Neves, L. & Lopes, M., 2016. Assessment of friction properties at geotextile encapsulated-sand systems' interfaces used for coastal protection. *Geotextiles and Geomembranes*, 44(3), pp. 278-286.
- Mueller, E. R., Pitlick, J. & Nelson, J., 2005. Variation in the reference Shields stress for bed load transport in gravel-bed streams and rivers. *Water Resources Research*, Volume 41.
- Neill, C., 1968. *A re-examination of the beginning of movement for coarse granular bed materials*, s.l.: Research Council of Alberta.
- Neill, C., Mannerstrom, M. & Azad, A. K., 2008. *Model tests on geobags for erosion protection*. Tokyo, Fourth International Conference on Scour and Erosion.
- Nikora, V. & Goring, D., 2000. Flow turbulence over fixed and weakly mobile gravel beds. *Journal of Hydraulic Engineering*, 126(9), pp. 679-690.
- Nortek, 2018. *The Comprehensive Manual for Velocimeters*, s.l.: s.n.
- Northwest Hydraulics Consultants (NHC), 2010. *Padma Multipurpose Bridge Design Project RT23 Geobag Flume Model Study*. s.l.:Prepared for Maunsell/AECOM and Bangladesh Bridge Authority.
- Oberhagemann, K. & Hossain, M., 2011. Geotextile bag revetments for large rivers in Bangladesh. *Geotextiles and Geomembranes*, Volume 29, pp. 402-414.
- Pilarczyk, K., 2000. *Geosynthetics and Geosystems in Hydraulic and Coastal Engineering*. Rotterdam: A. A. Balkema.
- Pilarczyk, K. W., 1991. *Coastal Protection Short Course Rijkswaterstaat*. Delft: Road and Hydraulic Engineering Division Van der Burghweg.
- Prancevic, J. P. & Lamb, M. P., 2015. Unraveling bed slope from relative roughness in initial sediment motion. *Journal of Geophysical Research: Earth Surface*, Volume 120, pp. 474 - 489.
- Recio, J. & Oumeraci, H., 2009. Process based stability formulae for coastal structures made of geotextile sand containers. *Coastal Engineering*, Volume 56, pp. 632-658.

- Recking, A., 2009. Theoretical development on the effects of changing flow hydraulics. *Water Resources Research*, 45(W04401), pp. 1-16.
- Schvidchenko, A. & Pender, G., 2000. Flume study of the effect of relative depth on incipient motion of coarse uniform sediments. *Water Resources Research*, 36(2), pp. 619-628.
- Shields, A., 1936. *Application of similarity principles and turbulence research to bed-load movement: English translation*, Pasadena: California Institute of Technology.
- Soulsby, R. L., 1983. The Bottom Boundary Layer of Shelf Seas. In: J. B, ed. *Physical Oceanography of Coastal and Shelf Areas*. Amsterdam: Elsevier, pp. 189-266.
- Thompson, A., Oberhagemann, K. & She, Y., 2020a. Geobag stability for riverbank erosion protection structures: Physical model study. *Geotextiles and Geomembranes*, 48(1), pp. 110-119.
- Thompson, A., She, Y. & Oberhagemann, K., 2020b. Geobag stability for riverbank erosion protection structures: Numerical model study. *Geotextiles and Geomembranes*, 48(5), pp. 703-712.
- USACE, 1994. *Hydraulic Design of Flood Control Channels*, Washington: U.S. Army Corps of Engineers.
- White, K., She, Y. & Zhang, W., Submitted. A Comparison of Shear Stress Estimation Methods for a Single Geobag on a Rough Bed. *Geotextiles and Geomembranes*.
- Yang, S., Shu, Y. & Yang, X., 2008. Flume experiment and numerical analysis for bank reinforcement with geocontainer. In: *Geosynthetics in Civil and Environmental Engineering*. Berlin, Germany: Springer, pp. 639-636.
- Zellweger, H., 2007. *Geotextile bags for river erosion control in Bangladesh*, Zürich: Swiss Federal Institute of Technology.
- Zhang, L. et al., 2020. Comparison of Methods for Bed Shear Stress Estimation in Complex Flow Field of Bend. *Water*, 2753(12), pp. 1-16.
- Zhu, L. et al., 2004. Settling Distance and Incipient Motion of Sandbags in Open Channel Flows. *Journal of Waterway, Port, Coastal and Ocean Engineering*, 130(2), pp. 98-103.
- Zimmermann, A., Church, M. & Hassan, M., 2010. Step-pool stability: Testing the jammed state hypothesis. *Journal of Geophysical Research*, Volume 115.

## 4 Evaluation of Geobag Design Formulas and Stability for Erosion Protection Structures in Rivers: Physical Model Study

### 4.1 Introduction

Rivers that experience significant erosion can negatively impact infrastructure, local residents and wildlife, and developing economies (Oberhagemann and Hossain 2011; Thompson et al. 2020a; Khajenoori et al. 2021). For example, the Brahmaputra River in Bangladesh experiences lateral erosion rates of up to 1 km per year and vertical scour rates of up to 70 m per year in some locations leading to the displacement of residents and loss of agricultural land (ADB 2020; Oberhagemann and Hossain 2011). To help minimize erosion and scour, extensive geobag erosion protection structures (i.e., revetment structures) have been and are currently being installed along the Brahmaputra River. Geobags are geotextile bags filled with sand and have also been used in other sand-bed rivers (i.e., Changjiang River, Yangtze River) as primary elements to erosion protection structures because of their low-cost, material accessibility and combined filtering-protection application (Heibaum et al. 2008; Heibaum 2014; Oberhagemann and Hossain 2011; Yang et al. 2008; Zhu et al. 2004). An additional benefit to using geobags as the primary element in revetment structures is that toe-scouring causes the geobags to ‘self-launch’ to a geotechnically stable slope of 1V:2H, thus improving the scour protection at the toe (Oberhagemann and Hossain 2011). Geobags have been studied extensively for coastal applications (e.g., Grune et al. 2007; Hornsey et al. 2010; Moreira et al. 2016; Recio and Oumeraci 2009), due to the frequent use of geobags in various coastal protective structures (Hornsey et al. 2011). Coastal hydraulic loading is dominated by wave loading and differs from fluvial hydraulic loading, which is dominated by current loading (Pilarczyk 1991). Therefore, the literature focused on coastal applications may not be applicable to open channel flows.

It has previously been identified that current sizing methodologies may result in oversizing the geobag elements for use in river erosion protection structures, i.e., revetment structures (Oberhagemann and Hossain 2011; Thompson et al. 2020a). This is likely because current design methodologies do not account for the flexibility and deformability of geobags (Thompson et al. 2020a). There is an opportunity to optimize the design methodologies to improve the cost-effectiveness of river erosion protection structures, and to reduce the labor intensity of installing such projects (Oberhagemann and Hossain 2011; Thompson et al. 2020a).

Design methodologies of geobag revetment structures require information regarding the geobag element stability and therefore the conditions at which geobags undergo incipient motion. Incipient motion is broadly defined as when the element begins to move (Shields 1936) and may be characterized by a critical velocity or critical Shields parameter. The Shields parameter (see Eq. 4-1) was originally defined by Shields (1936) to characterize the incipient motion of sediment, based on a critical shear stress:

$$\psi = \frac{\tau_{cr}}{(\rho_s - \rho_w)gD} \quad \text{Eq. 4-1}$$

where,  $\psi$  is the Shields parameter,  $\tau_{cr}$  is the critical shear stress at incipient motion [Pa],  $\rho_w$  is the density of water [kg/m<sup>3</sup>],  $\rho_s$  is the density of the sediment or element [kg/m<sup>3</sup>],  $g$  is the acceleration due to gravity [m/s<sup>2</sup>], and  $D$  is the characteristic size [m].

Several studies have examined geobag stability in fluvial applications under a variety of conditions (i.e., Korkut et al. 2007; Neill et al. 2008; NHC 2010; Akter et al. 2013; Thompson et al. 2020a,b; Khajenoori et al. 2021). Korkut et al. (2007) focused on geobag erosion protection structures for bridge abutments and recommended geobag placement methods to improve stability. Neill et al. (2008) and NHC (2010) modified a common riprap design formula (see Eq.

4-2) for geobag applications, based on data from 1:20 scaled laboratory experiments. Akter et al. (2013) characterized geobag failure mechanisms with a 1:10 scaled revetment structure. They used a conveyance estimation system and depth-averaged velocity to predict bed shear stresses acting on the geobags. Thompson et al. (2020a) studied a 1:7 physical scaled model of geobags in a flume to analyze their stability, as well as the suitability of current design methodologies. Multiple geobag sizes formed unique test-sections that were placed in various sequences in the flume to consider the influence of their relative location. Thompson et al. (2020b) developed a computational fluid dynamics (CFD) model to obtain an initial estimate for a critical Shields parameter for geobags, based on the data obtained by Thompson et al. (2020a). Their results suggested that different fill ratios of sand in the geobags impacted their stability, which has also been observed by others (i.e., Pilarczyk 2000; Grune et al. 2007; Recio and Oumeraci 2009). Khajenoori et al. (2021) studied the impact of construction methods and revetment slopes on the stability of the revetment structure and found that geobag failure mechanisms were dependent on both water depth and revetment slope.

Although geobag stability has been studied in fluvial applications, there remains the issue of obtaining an appropriate sizing methodology for geobags in a revetment structure. Two design formulas have been commonly used for sizing geobag elements in a revetment structure. In the Brahmaputra River, geobags are currently sized with a modified version of the U.S. Army Corps of Engineers (USACE) design formula (USACE 1994), originally intended for rock-based riprap (Bangladesh Water Development Board 2010):

$$D_{30} = S_F C_S C_V C_T y \left[ \left( \frac{\rho_w}{\rho_s - \rho_w} \right)^{0.5} \left( \frac{V_{cr}}{\sqrt{K_s g y}} \right) \right]^{2.5} \quad \text{Eq. 4-2}$$

where,  $D_{30}$  is the rock size by which 30% is finer by weight [m],  $S_F$  is a safety factor,  $C_S$  is a stability coefficient,  $C_V$  is vertical velocity distribution coefficient,  $C_T$  is the thickness coefficient,  $y$  is the flow depth [m],  $V_{cr}$  is the depth-averaged velocity at incipient motion [m/s], and  $K_s$  is the side slope correction factor ( $= \sqrt{1 - \left(\frac{\sin^2 \theta}{\sin^2 \vartheta}\right)}$ ; where,  $\theta$  is the angle of the slope to the horizontal, and  $\vartheta$  is the angle of repose of the elements).

The USACE formula relies on the critical depth-averaged velocity at which elements undergo incipient motion to estimate the appropriate size and gradation. This formula is limited by its assumption that equal depth-averaged velocities observe the same velocity profiles, and therefore bed shear stresses (Thompson et al. 2020a; USACE 1994), which are arguably more important with respect to element stability (Shields 1936; Neill 1968). The design size is also sensitive to the depth-averaged velocity, where a 10% difference in velocity results in a ~30% difference in size.

Neill et al. (2008) modified the USACE formula for geobags, using data collected from a 1:20 scaled laboratory model. Instead of employing  $D_{30}$  as the characteristic size variable, they suggested characterizing the geobag size by the cube root of the filled geobag's volume. They estimated a stability coefficient of 0.77 for geobags (Neill et al. 2008), which is more than double the stability coefficient for rocks ( $C_S = 0.30 - 0.34$ ; USACE 1994). A greater stability coefficient means the element is less stable (USACE 1994). NHC (2010) calibrated the stability coefficient for geobags to be 0.31 based on tests from a 1:20 scaled model. The different stability coefficients estimated by Neill et al. (2008) and NHC (2010) may be due to issues in proportionally scaling the flexibility of the geobags. Thompson et al. (2020a) suggested characterizing the geobag size by the nominal thickness, as volume can be challenging to

characterize for deformable shapes. They also adjusted the stability coefficient for three different fill ratios of sand in the geobag, using data from a 1:7 scaled physical model. They found that the stability coefficient was significantly smaller than those presented in Neill et al. (2008) and NHC (2010), where their coefficient ranged from 0.07 for geobags with fill ratios of ~80% to 0.15 for geobags with fill ratios of ~60%.

Bezuijen and Vastenburb (2013) presented the Pilarczyk design formula (see Eq. 4-3) that also employs the critical depth-averaged velocity to determine the effective diameter of the design element. The Pilarczyk formula considers the effect of the position of the geobag relative to the revetment structure through a stability parameter (i.e., a geobag on the edge of the structure versus on the top-layer). A Shields parameter is also incorporated in the formula, where a smaller geobag ( $< 0.3 \text{ m}^3$ ) is assigned a Shields parameter of 0.035 and a larger geobag is assigned a Shields parameter of 0.05. These Shields parameter guidelines are the empirical values for riprap and loose, placed blocks (Pilarczyk 1990), and thus require validation for geobags.

$$\left(\frac{\rho_s - \rho_w}{\rho_w}\right) D_k \geq 0.035 \frac{\varphi K_T K_h V_{cr}^2}{\psi K_S 2g} \quad \text{Eq. 4-3}$$

where,  $D_k$  is the effective diameter of the element [m],  $\varphi$  is the stability parameter,  $\psi$  is the Shields parameter,  $K_T$  is the turbulence factor,  $K_h$  is the depth factor,  $K_S$  is the slope factor, and  $V_{cr}$  is the depth-averaged velocity at incipient motion [m/s].

Pilarczyk's formula has the potential for improvement if a Shields parameter more representative of geobags is used. Above a boundary Reynolds number of approximately 1000 ( $\text{Re} = \frac{u_{cr}^* d_n}{\nu}$ , where  $\text{Re}$  is the boundary Reynolds number,  $u_{cr}^*$  is the critical shear velocity ( $= \sqrt{\tau_{cr}/\rho_w}$ ) and  $\nu$  is the kinematic viscosity), the critical Shields parameter becomes a constant (Shields 1936).

Buffington and Montgomery (1997) compiled data from studies to define a critical Shields

parameter for gravel-bed rivers (= 0.045). Thompson et al. (2020b) provided an initial estimate of a critical Shields parameter for geobags (= 0.09) based on results from a CFD model, which they identified requires further validation. Thompson et al. (2020b) attributed the higher value for geobags to their relatively low density compared to gravel and the high drag force acting on the geobags at incipient motion. Incipient motion is an inherently statistical phenomena that depends on the random nature of turbulence and inter-granular geometry (Buffington and Montgomery 1997). Therefore, to develop a better understanding of the Shields parameter for geobags, more data is required. Different studies have used an average critical bed shear stress over the study reach, while others have employed a local critical bed shear stress (Buffington and Montgomery 1997; Recking 2009). Due to the instantaneous nature of incipient motion, a local bed shear stress may better reflect the conditions at which incipient motion occur (Neill 1968).

This study aimed at improving our understanding of the stability of geobags in fluvial applications, by investigating the effect of geobag fill ratio on stability, assessing the applicability of the existing geobag sizing methodologies, and collecting more data at incipient motion. The incipient motion of a full bed of geobags were observed in a 1:7 scaled physical model. The velocity profiles at multiple locations along the test section at incipient motion were measured. Critical shear stresses were estimated to provide additional estimates of the critical Shields parameter for geobags. The experimental data was used to establish a relationship between geobag fill ratio and stability, and such relationship was incorporated into existing design formulas. Finally, the applicability of the design formulas was investigated for the Brahmaputra River.

## 4.2 Methodology

### 4.2.1 Geobag Characteristics

Geobags were scaled from three common sizes used in the Brahmaputra River (ADB 2002; ADB 2010; ADB 2014; ADB 2020), using the Froude scaling laws for a 1:7 scale (see Table 4-1). The geobag sizes are typically categorized by the field scale mass, which correspond to specific dimensions and fill ratios. In this study, the dimensions of the geobags were scaled and the fill ratios and masses were varied. Thompson et al. (2020a) identified that scaled geobags made of a cloth material with an area weight of 80 g/m<sup>2</sup> better replicated the flexibility of prototype geobags, compared to a scaled geotextile material. Therefore, all geobags in this study were made of cloth material (80 g/m<sup>2</sup>) of three different colors (gray, green, and blue for geobag A, B, and C, respectively) to help differentiate the sizes.

Table 4-1: Summary of geobags used in the experiments.

Lab Geobag	Lab Scale Dimensions (Width x Length) [cm]	Field Scale Mass [kg]	Field Scale Dimensions (Width x Length) [cm]
A	10.0 x 15.0	125	70.0 x 105.0
B	14.0 x 18.0	250	98.0 x 126.0
C	21.0 x 29.0	800	147.0 x 203.0

The fill ratio of sand in the geobags was varied between experiment series (Table 4-2) to study the effect of fill ratio on stability. The fill ratio is defined as the actual geobag mass divided by the geobag mass when fully filled with sand. For all three lab geobags, the fill ratio corresponding to their scaled field mass was defined and tested, which is 84% for geobag A, 66% for geobag B, and 58% for geobag C, respectively. Two additional fill ratios were tested for both geobags B and C. For each fill ratio, the geobag's angle of flexibility, nominal thickness, mass, and density were measured.

Table 4-2: Summary of experiment series

Series	Bag	Slope	Fill Ratio [%]	No. of Layers	Nominal Thickness [m]	Density [kg/m <sup>3</sup> ]	Mass [kg]
1	A	Flat	84	2	0.0165	1733	0.364
2	B	Flat	84	3	0.0205	1734	0.928
3	B	Flat	84	2	0.0205	1734	0.928
4	B	Flat	66	2	0.0155	1617	0.729
5	B	Flat	33	2	0.0085	1669	0.364
6	C	Flat	84	2	0.0328	1685	3.380
7	C	Flat	66	2	0.0241	1740	2.650
8	C	Flat	58	2	0.0181	1677	2.330
9	A	1V:2H	84	2	0.0165	1733	0.364
10	B	1V:2H	66	2	0.0155	1617	0.729
11	C	1V:2H	58	2	0.0181	1677	2.330

The flexibility of geobags used in this study was compared to both the prototype geobags and the geobags used in Thompson et al. (2020a) and NHC (2010) (see Figure 4-1). The angle of flexibility was measured by hanging half the geobag from a flat surface and measuring the resulting angle to the horizontal surface. The dimensionless angle of flexibility and mass were made dimensionless by taking the ratio of the geobag variable to that of a prototype 125 kg geobag (Thompson et al. 2020a). For geobags with a higher fill ratio, the dimensionless angle of flexibility was more comparable to that of a prototype geobag.

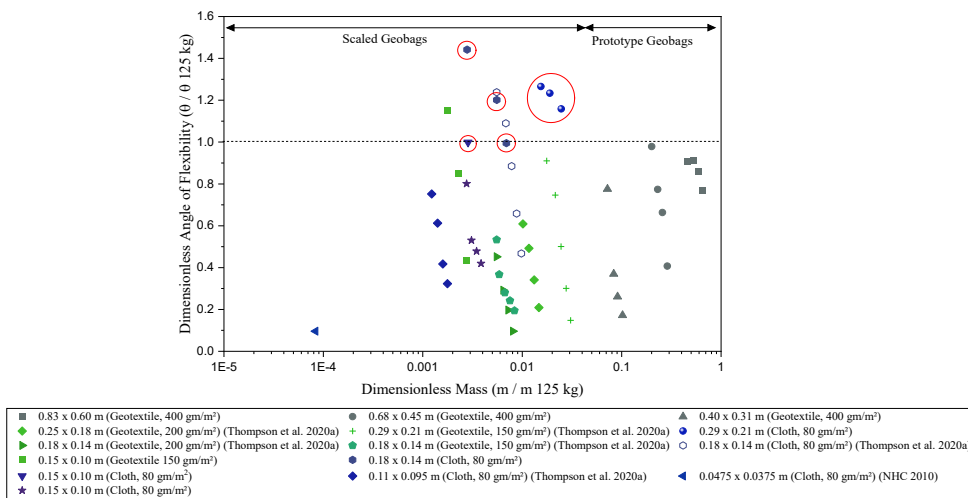


Figure 4-1: Comparison of the dimensionless angle of flexibility and mass between scaled and prototype geobags. The points circled in red correspond to the geobags used in this study.

The nominal thickness was taken as the thickness of the geobag if the filling sand was evenly distributed within the bag. The density of the geobags was measured by freezing the fully saturated geobags, then measuring the displaced water volume of the frozen geobags. The density was calculated as the ratio of the geobag mass to the displaced water volume. The average density of all geobags in this study was  $1700 \text{ kg/m}^3$ . This is comparable to the average density of geobags measured in Chapter 3 ( $1725 \text{ kg/m}^3$ ), and to values found in the literature: Zellweger (2007) measured an average density of  $1760 \text{ kg/m}^3$ , NHC (2010) measured an average density of  $1778 \text{ kg/m}^3$  and Thompson et al. (2020a) measured an average density of  $1718 \text{ kg/m}^3$ .

The geobag characteristics (i.e., fill ratio, bag dimensions) and bed configurations (i.e., number of layers, bed slope) were varied to study their impact on geobag stability (see Table 4-2). In Series 2, three layers of bags were installed on a flat bed while in Series 3, two layers of the same bags were installed. This was to study the impact of the number of bag layers on geobag stability. In Series 5, geobag B was filled to the same mass as geobag A in Series 1 to determine whether mass or fill ratio was more influential on stability. To determine the impact of the bed side slope on geobag stability, geobags A, B and C at their respective scaled field mass were studied on both a flat and 1V:2H slope, where the 1V:2H slope represents a typical revetment slope in Series 9, 10 and 11.

#### 4.2.2 Experimental Set-Up

The experiments were conducted in a recirculating flume (1.2 m x 20 m) in the Northwest Hydraulics Consultants (NHC) Laboratory in North Vancouver. Two bed configurations were studied: a flat bed and a 1V:2H sloped bed to replicate a launched slope (Figure 4-2). A 2 m rock ( $D_{50} = 64 \text{ mm}$ ) section was placed upstream of the geobag test section to help develop the

flow. A shorter rock section was placed downstream of the geobag test section to stabilize the bed. Flow was fully developed at the geobag test section for both the flat bed and 1V:2H sloped bed, verified by Acoustic Doppler Velocimeter (ADV) measurements of the velocity profiles.

The geobag test section was modified between each experimental series (see Table 4-2). For Series 2, three layers of geobags were dumped following the method by Thompson et al. (2020a), where the geobags were dropped in approximately 30 cm of water to replicate the installation method used in the field. For Series 1 and 3 – 11, two layers of geobags were dumped following the same method. The number of geobags used in each series is equal to the number required to cover the test section area if the geobags were placed side-by-side, then multiplied by the number of layers. For example, in Series 2, approximately 103 bags were required to cover the test section area if placed side-by-side, therefore 309 geobags were dumped to produce approximately 3-layers.

The flume sidewalls were made of plexiglass, and the bed substrate at the test section was made of a metal grid in both bed configurations for consistency and to prevent geobags from sliding down the 1V:2H slope. The flume slope was set to 0%. The average flow depth,  $h$ , was maintained at 0.60 m above the geobags for the flat bed configuration. Due to limitations in the flume height, the average flow depth in the 1V:2H sloped bed configuration was maintained at 0.30 m above the bag surface at the center transverse cross-section of the flume. Flow depths at the test section were measured with a point gauge with an accuracy of +/- 0.5 mm.

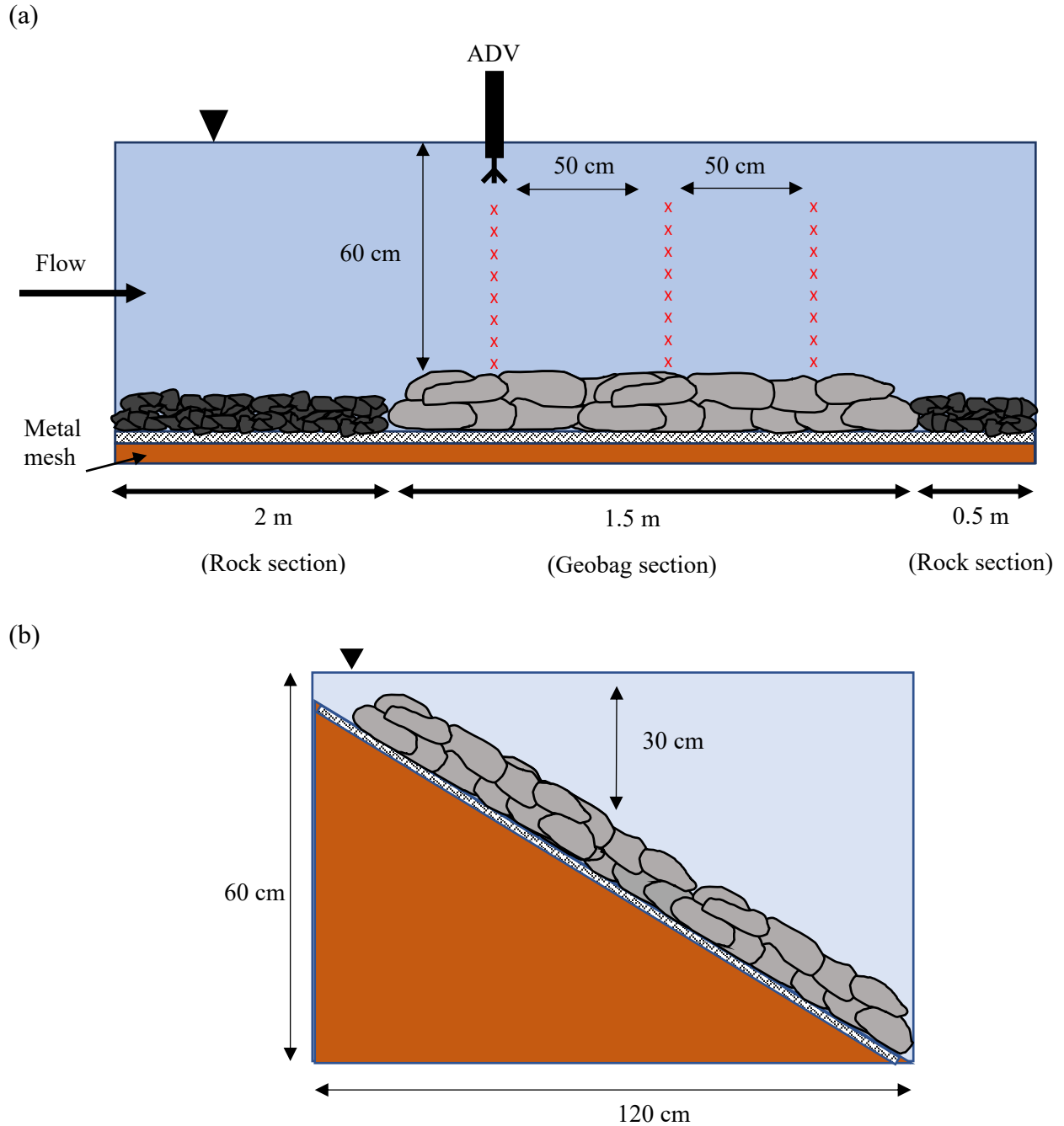


Figure 4-2: Schematic of experimental set-up of (a) sideview of the flat bed, (b) cross-sectional view of the 1V:2H sloped bed.

### 4.2.3 Experiment Procedure

For each experiment series, the geobag test section was subjected to five velocity set-points, representing typical flow velocities observed in the Brahmaputra River, where the Brahmaputra

can reach flow velocities of up to 5.1 m/s (Thompson et al., 2020a) (see Table 4-3). The lab velocity was determined using the Froude scaling laws, at a 1:7 scale. The lab velocity set-points were measured with an ADV at  $0.4h$  to confirm the depth-average velocity set-point was reached. The velocity set-points were incrementally increased until incipient motion was reached. Incipient motion was defined as when 5% of the total number of geobags had moved from one location to another, the same definition as in Thompson et al. (2020a) and NHC (2010). Local shifting, where the geobag shifts in place and/or there is internal sand movement, was not considered in the definition of incipient motion.

Between each velocity set-point, the flume was drained, and photos were taken of the test-section. The photos were processed in pix4D to develop 3-D orthographic projections and point clouds of the test-section. Differential point clouds were obtained in CloudCompare V2.12 to help determine the number of bags that failed after each velocity set-point, as well as to analyze the difference observed in the surface bed elevations between velocity set-points.

Table 4-3: Velocity set-points for each experiment series

Velocity Run	Prototype Depth-Averaged Velocity (m/s)	Lab Depth-Averaged Velocity (m/s)
1	3.0	1.13
2	3.5	1.32
3	4.0	1.51
4	4.5	1.70
5	5.0	1.89

At each velocity set-point, velocity profiles were collected with a Nortek Vectrino ADV (P 21363-1) at three cross-sections of the test-section along the centerline (see Figure 4-2) which were approximately 0.50 m apart. The first cross-section was placed approximately 0.20 m downstream of the start of the test section. The ADV measured the time-averaged velocity and

velocity fluctuations in all three directions at 100 Hz sampling rate. The data collected from the ADV was filtered to an average correlation > 70% and signal to noise ratio (SNR) > 15dB, as recommended by the manufacturer (Nortek 2018). Phase space thresholding was applied to the data as per Nikora and Goring (2000). The velocity profiles were collected by measuring the time-averaged velocity at 8-10 points along the vertical, in increments of 1-3 cm, from approximately 1 cm above the bed to half of the water depth.

Local bed shear stresses were estimated using the velocity fluctuation data collected from the ADV. As the flow conditions for this study were complex and turbulent, the turbulent kinetic energy (TKE) method was used to estimate the local bed shear stress (Biron et al. 2004; White, K. et al. Submitted).

$$\tau_b = C_1 \frac{\rho_w}{2} (\langle u'^2 \rangle + \langle v'^2 \rangle + \langle w'^2 \rangle) \quad \text{Eq. 4-4}$$

where  $C_1$  is a proportionality constant,  $u'$  is the velocity fluctuation in the streamwise direction,  $v'$  is the velocity fluctuation in the transverse direction, and  $w'$  is the velocity fluctuation in the vertical direction. In turbulent flows,  $C_1$  is commonly calibrated by relating the shear stress estimated from the TKE method to the shear stress estimated from the Reynolds stress method (Soulsby 1983; Kim et al. 2000; Biron et al. 2004; Zhang et al. 2020). The Reynolds stress (Schlichting and Gersten 2000) is defined as:

$$\tau_b = -\rho \langle u'w' \rangle \quad \text{Eq. 4-5}$$

where  $u'$  is the velocity fluctuation in the stream-wise direction and  $w'$  is the velocity fluctuation in the vertical direction. The proportionality constant was calibrated to  $C_1 = 0.23$ .

## 4.3 Results and Discussion

### 4.3.1 Incipient Motion

Figure 4-3 shows the cumulative percentage of number of geobags failed at different velocity setpoints for all test series. Notably, geobags with 84% fill ratio experienced lower rates of failure than geobags of equal dimensions with lower fill ratios, apart from one case: geobags from Series 3 (Geobag B, 84% fill ratio) and Series 4 (Geobag B, 66% fill ratio) experienced the same rate of failure at the highest velocity. At lower velocities, geobags of lower mass experienced more movement than geobags of higher mass. However, geobags with lower mass and higher fill ratios were generally more stable than geobags with higher mass and lower fill ratios, at the higher velocities. For example, the geobags from Series 8 weighed on average 2.33 kg with a 58% fill ratio, and they had higher failure rate (10.6% of geobags failed at a depth-averaged velocity of 1.82 m/s) than the geobags from Series 4 which were on average 0.73 kg with a 66% fill ratio (4.9% of geobags failed at a depth-averaged velocity of 1.84 m/s). This trend was consistent for all cases, apart from Series 10 and 11, where the geobags with a lower mass and higher fill ratio (Series 10) experienced lower stability on the 1V:2H slope. Grune et al. (2007) also observed that geotextile sand containers, or geobags, with lower mass and higher fill ratios were most stable.

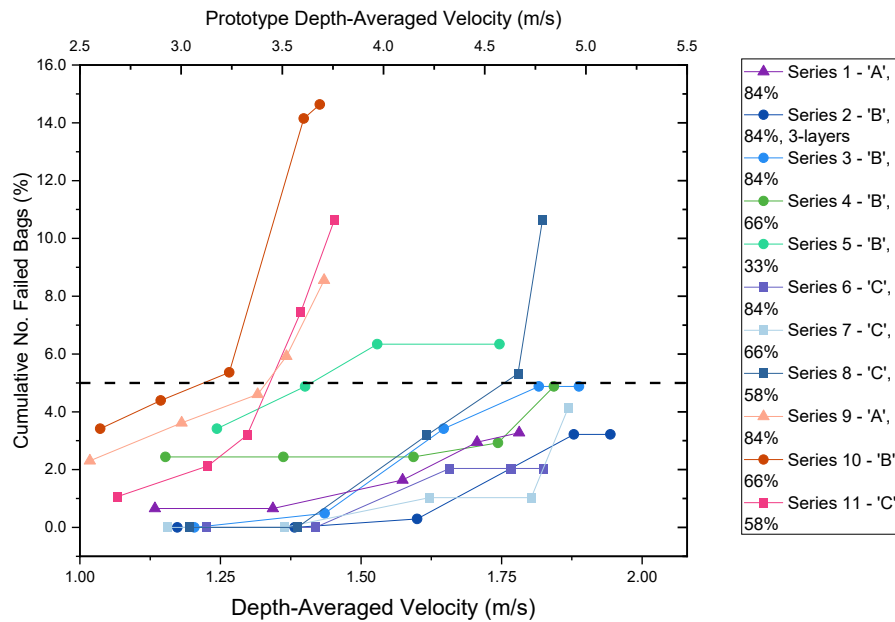


Figure 4-3: Cumulative percentage of failed bags from each series. Dashed line indicates the incipient motion threshold of 5% failed bags.

A direct comparison can be made between Series 5 (Geobag ‘B’ with 33% fill ratio) and Series 1 (Geobag ‘A’ with 84% fill ratio), as the geobags in both series had the same mass but different fill ratios due to their different dimensions. The geobags from Series 5 underwent incipient motion at a depth-averaged velocity of 1.4 m/s (prototype depth-averaged velocity of 3.7 m/s) whereas the geobags from Series 1 did not observe incipient motion even at the highest achievable depth-averaged velocity in the flume.

These findings suggest that the geobag fill ratio impacts the stability more than the mass of the geobags, and that the internal movement of sand within the geobags is critical to the incipient motion of the entire bed. This observation is supported by the literature, where Pilarczyk (2000) and Thompson et al. (2020a) suggested that geobags with higher fill ratios of ~80% were more stable than geobags with lower fill ratios regardless of size and mass. Grune et al. (2007) also observed that geobags with higher fill ratios were more stable, and their results showed a fill ratio of 100% was most stable under coastal wave-loading. Thompson et al. (2020a) noted that

under current loading, the geobags from the NHC (2010) study were less stable and were ~95% filled. They suggested that this was due to a lower contact area between geobag elements in the bed. This observation may also be explained by the smaller model scale (1:20) used in the NHC (2010) tests, compared to Thompson et al. (2020a) and this study (1:7 model scale). As indicated previously, the angle of flexibility is challenging to scale proportionally, such that a larger scale with a lighter bag material was required to maintain similarity between the model and prototype for this study. The smaller scale model geobags have a significantly lower angle of flexibility (see Figure 4-1) compared to the geobags used in Thompson et al. (2020a) and this study, which would ultimately impact the stability.

The geobag element and internal sand movements can be visualized in surface differential plots showing the change in bed elevations between velocity set-points. The geobags from Series 5 reached 5% failure between velocity set-points of 1.32 m/s and 1.51 m/s, and the differential bed elevations and corresponding photos are shown in Figure 4-4a. The differential bed elevations and corresponding bed photos for Series 1, at the same velocity set-points, are shown in Figure 4-4b. The surface differential plots show evidence of internal sand movement (differential elevation range of 0.02 m) and geobag element movement (differential elevation > 0.02 m). Pilarczyk (2000) and Thompson et al. (2020a) also observed internal sand movement within geobags at relatively low velocities of 1.5 m/s and 1.2 m/s, respectively. In Figure 4-4a, the internal sand movement is clearly observed and appears to pile within the geobags towards the downstream end of the flume, thus increasing the surface bed elevation. The dark red and blue sections shown in Figure 4-4a correspond to geobag element movement. In Figure 4-4b, the internal movement of the sand appears to press down slightly in the geobags in the upstream section of the flume, thus reducing the surface bed elevation. There also appears to be less

internal sand movement in Figure 4-4b than in Figure 4-4a. This is due to the different sizes and fill ratios of the geobags in Series 1 (Figure 4-4b) and Series 5 (Figure 4-4a), where the geobags from Series 5 had a lower fill ratio of 33% and therefore more space within the bag for internal sand movement compared to the geobags from Series 1 (fill ratio of 84%). Some of the geobags shifted in place (see the red circles in Figure 4-4b for examples), rather than moving from one location to another, and therefore did not count as a failed bag. Shifting in place may add stability to the bed, as the geobags naturally find more stable positions by increasing the contact area between geobag elements (Thompson et al. 2020a).

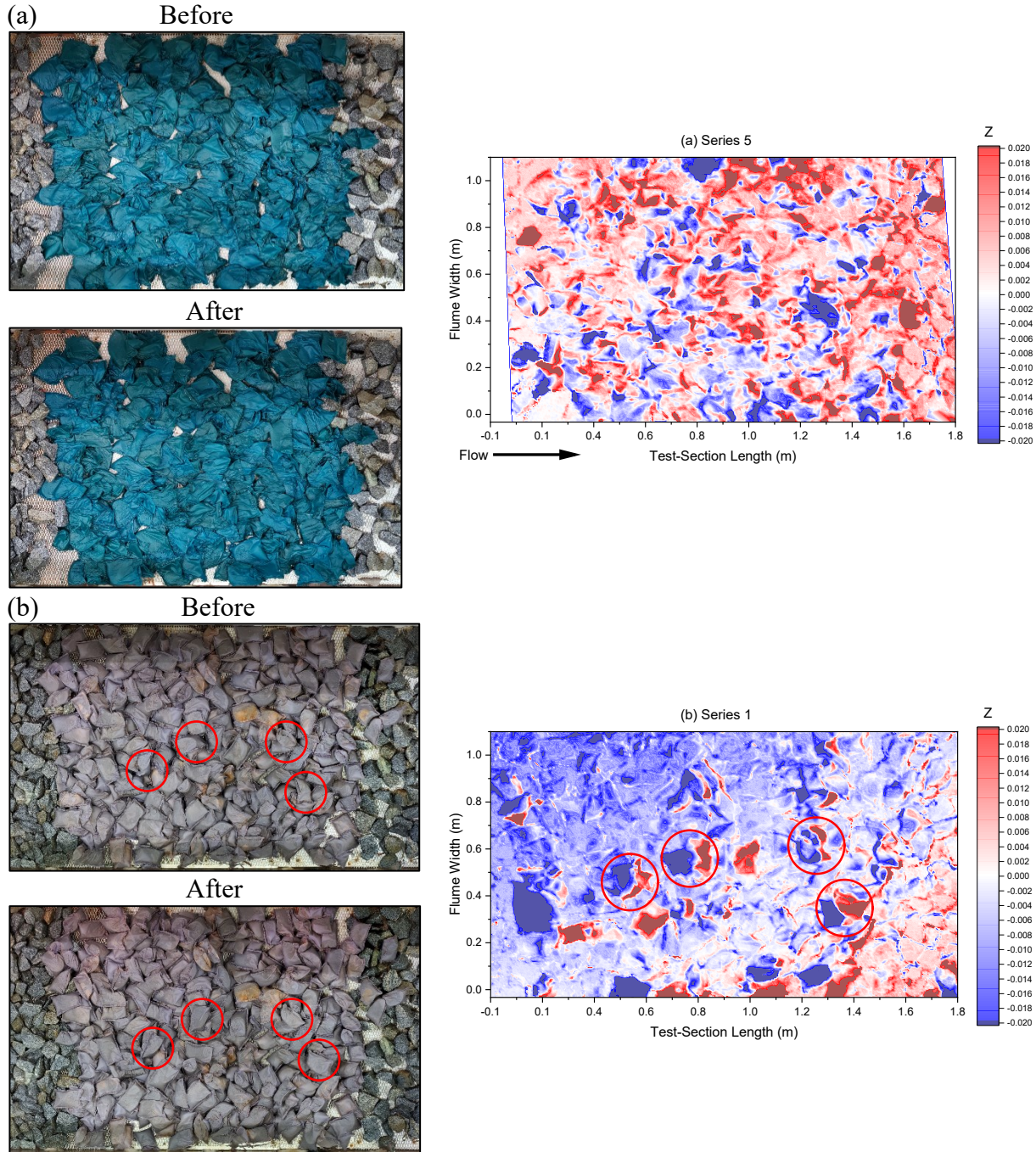


Figure 4-4: Photos of the test-section before and after velocity set-point 1.51 m/s (prototype velocity 4.0 m/s) and the corresponding contours of the differential bed elevations,  $z$ , for (a) Series 5 and (b) Series 1. Circled geobags in (b) represent geobags which shifted in place yet did not fail.

Series 9 to 11 observed higher percentages of failure at lower velocities than Series 1 to 8 (see Figure 4-3). This is due to the change in bed configuration from a flat bed (Series 1 to 8) to a

1V:2H sloped bed (Series 9 to 11), such that there is an additional gravitational force acting on the bed in the sloped bed series. From visual observations, the geobags in the sloped bed series failed by both flipping over towards the bottom (toe) of the slope and the downstream end of the flume (e.g., Series 10 in Figure 4-5b). In contrast, the geobags in the flat bed series failed by flipping over with the direction of flow (e.g., Series 4 in Figure 4-5a, using the same size and fill ratio as Series 10). The 1V:2H sloped bed configuration also had an average flow depth of 0.30 m, due to limitations with the flume height, which is half the average flow depth of the flat bed configuration. Lower average flow depths in rough flows increase the extent of turbulence (Chow 1959) and likely contributed to the higher rates of failure.

The observations for the sloped bed series agree with the results from Thompson et al. (2020a), where the failure of geobags on the 1V:2H slope was higher than on the flat bed for dumped bags. In Khajenoori et al. (2021), geobags on steeper revetment slopes were observed to be more stable than shallow slopes. This may be attributed to the different water depths tested in Khajenoori et al. (2021), where they tested lower water depths relative to the revetment height, compared to this study and Thompson et al. (2020a). It could also be due to the different placement techniques of the geobags, where in Khajenoori et al (2021) the geobags were placed side-by-side in two different methods. In this study and Thompson et al. (2020a), the geobags were dumped from water surface, creating a very different bed surface compared to Khajenoori et al. (2021). Furthermore, incipient motion data have scatter, such that more data is required to determine a statistically significant relationship between slope and bed stability.

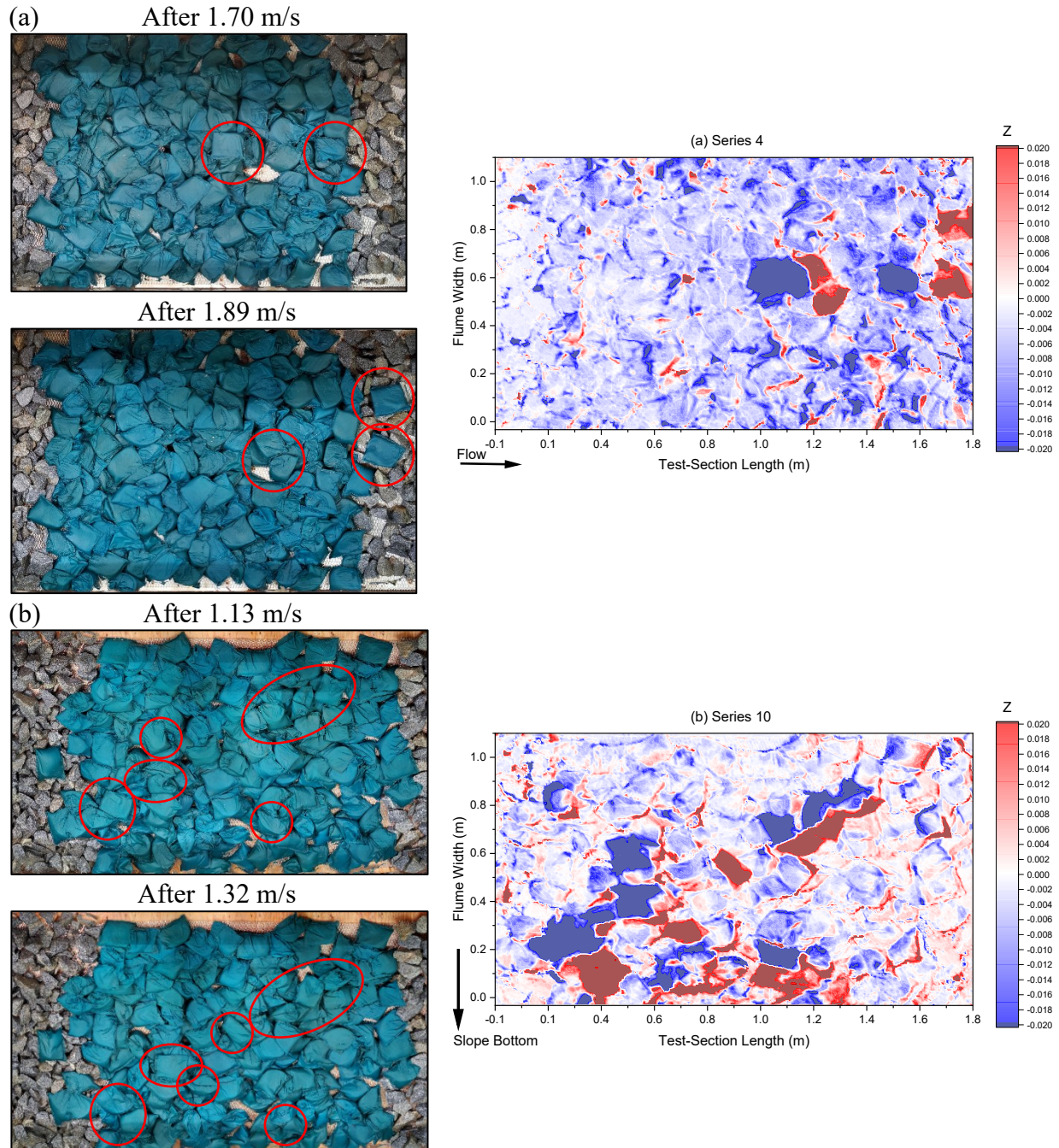


Figure 4-5: Contours of the differential bed elevations,  $z$ , between two velocity set-points (a) 1.70 m/s and 1.89 m/s for Series 4, (b) 1.13 m/s and 1.32 m/s for Series 10, and their corresponding orthographic projection photos. Geobags that moved are circled in red.

Figure 4-6 compared the incipient motion results for geobags A and B to the same geobags (material, size, and fill ratio) from Thompson et al. (2020a) for the flat bed configuration. As described above, Thompson et al. (2020a) varied the order of multiple geobag sizes in the test-

section, thus introducing an additional variable of the geobags relative location in the flume and to other geobag sizes. In Figure 4-6, the data from Thompson et al. (2020a) is categorized by the different sequences of the geobag sizes; for example, in Sequence 2 the scaled 250 kg cloth bags were placed furthest upstream with other sizes following, and in Sequence 3, the scaled 250 kg cloth bags were placed downstream of the scaled 125 kg cloth bags which were placed downstream of the scaled 800 kg geotextile bags. From Figure 4-6, utilizing multiple geobag sizes (and fill ratios) appears to result in a higher degree of failure than using a single size and fill ratio. This may be attributed to the varying bed thickness and perhaps a chain effect of geobag failure. Thompson et al. (2020a) dumped two layers of the different sized geobags using the same methodology for each size. As the geobag size and thickness differed, the bed thickness was also different for each geobag section, thus creating a less uniform bed topography and more complex flow condition compared to this study. Thompson et al. (2020a) also observed that geobags tended to fail in long sections, suggesting that upstream geobag failures incurred failures directly downstream. This may be because when upstream geobags failed, they exposed the geobags downstream. This effect would likely be more drastic when larger geobags were placed in the upstream sections, as they effectively block the flow from smaller geobags downstream of them. This chain effect of failure was not so clearly observed in this study.

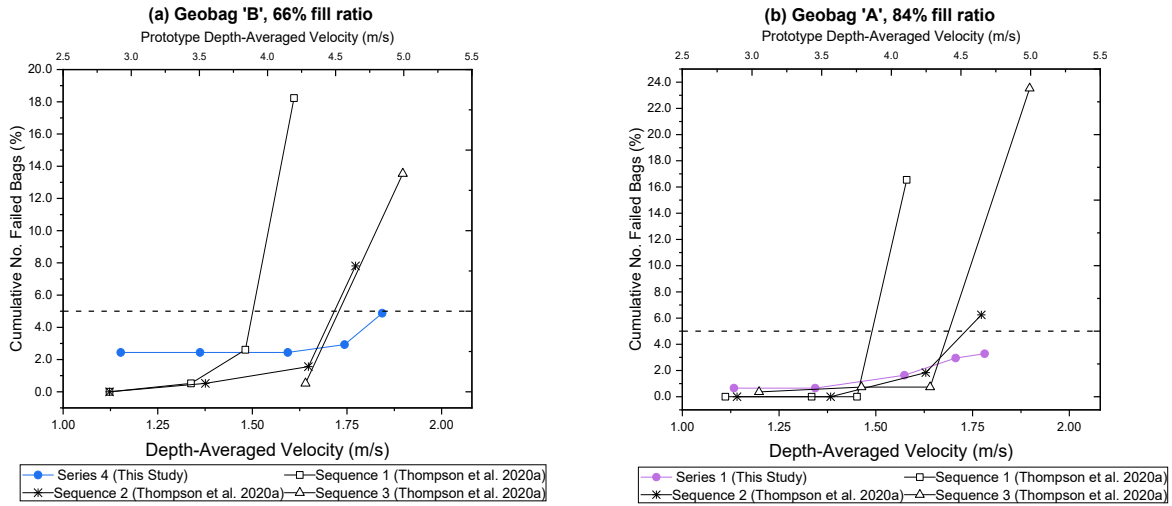


Figure 4-6: Comparison of incipient motion between this study and Thompson et al. (2020a) for (a) geobag B with a 66% fill ratio (250 kg prototype size), and (b) geobag A with an 84% fill ratio (125 kg prototype size).

### 4.3.2 Critical Shields Parameter

The critical Shields parameters at incipient motion were estimated for all series and ranged from 0.09 to 0.22, with an overall average value of 0.16. The results are presented in Table 4-4 for the flat bed series and Table 4-5 for the sloped bed series. Note that the Shields parameter was estimated using the average critical local bed shear stress of the three measurement cross-sections. In Figure 4-7, the critical Shields parameters from this study are plotted against the boundary Reynolds numbers.

The range in Shields parameters estimated in this study may be explained by using the critical local bed shear stress rather than an average bed shear stress in Eq. 4-1. Local bed shear stresses may better represent the instantaneous nature of incipient motion and can often be much higher than the average bed shear stress over the study reach (Neill 1968). Furthermore, critical Shields parameters are an inherently statistical problem, such that variation in their values is expected (Buffington and Montgomery 1997).

Table 4-4: Summary of critical Shields parameters for all bags from the flat bed experiments. The dash (–) means that no test was performed.

Geobag	Critical Shields Parameter			
	Fill Ratio: 84%	Fill Ratio: 66%	Fill Ratio: 58%	Fill Ratio: 33%
A	No failure	–	–	–
B	$0.09^* \pm 0.03$	$0.22 \pm 0.07$	–	$0.19^* \pm 0.07$
C	No failure	No failure	$0.17 \pm 0.07$	–

\* 4.9% of bags failed (just under the incipient motion cut off)

Table 4-5: Summary of critical Shields parameters for all bags from the 1V:2H bed experiments. The dash (–) means that no test was performed.

Geobag	Critical Shields Parameter		
	Fill Ratio: 84%	Fill Ratio: 66%	Fill Ratio: 58%
A	$0.11 \pm 0.03$	–	–
B	–	$0.18 \pm 0.05$	–
C	–	–	$0.13 \pm 0.06$

Thompson et al. (2020b) observed that bags with lower fill ratios tended to fail at lower critical velocities and lower average total shear stresses. They attributed this to the higher potential for internal sand movement in geobags with lower fill ratios. Similarly, the bags in this study with lower fill ratios failed at lower critical velocities; however, the local bed shear stress values, and consequently the average bed shear stresses and critical Shields parameters, did not necessarily reflect the same trend (see Figure 4-7). This is explained by how widely local bed shear stress values can vary, which is due to the local variations in surface bed elevation and random nature of turbulence (Neill 1968; Buffington and Montgomery 1997; Biron et al. 2004).

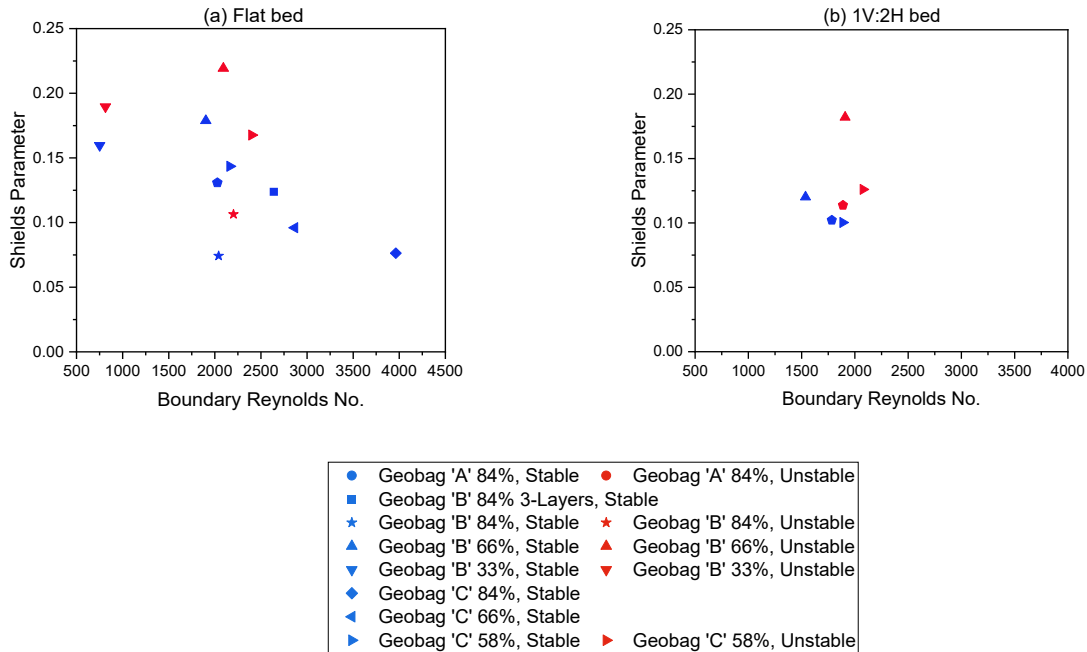


Figure 4-7: Shield parameters of the stable and unstable conditions for (a) flat bed series, and (b) 1V:2H series.

Figure 4-8 shows the stable and unstable Shields parameters estimated from this study and Thompson et al. (2020b). The range of critical Shields parameters estimated by Thompson et al. (2020b) are between 0.09 and 0.16, which are on average slightly lower than the estimates obtained in this study. This is expected as the geobags in Thompson et al. (2020b) experienced higher rates of failure and thus lower stability. It may, however, be difficult to compare the critical Shields parameters and boundary Reynolds numbers directly with the results from Thompson et al. (2020b) because of the different bed configurations and different estimation methods for critical shear stress, shear velocity and geobag thickness. As stated previously, one of the main differences between Thompson et al. (2020b)'s study and this study is the bed configuration. In Thompson et al. (2020b), multiple geobag sizes made up the test-section, whereas in this study only one geobag size made up the test-section. This difference not only impacts the range in bed roughness but also the flow development at the test-section, such that in

Thompson et al. (2020b) the flow may be more complex from the varying geobag sizes. Additionally, in Thompson et al. (2020b), the critical shear stress was estimated by dividing the total force by the geobag area, where the forces were determined from their CFD model. These values were validated with the total shear stress estimated by the energy grade line method (Thompson et al. 2020b). As noted in the literature, different shear stress estimation methods can result in different values for the same flow and bed conditions (Biron et al. 2004; Zhang et al. 2020; White et al. Submitted). In this study the TKE method was used to estimate the local bed shear stress at three cross-sections, since the TKE method has previously been identified as a more suitable option for complex flow regimes (Biron et al. 2004; White et al. Submitted). It also appears that a near-bed velocity was used to estimate the boundary Reynolds number in Thompson et al. (2020b) rather than the square root of the bed shear stress (i.e.,  $u_{cr}^* = \sqrt{\tau_{cr}/\rho}$ ) that was used in this study. In much of the literature the square root of the bed shear stress is used to estimate the shear velocity (e.g., Shields 1936; Buffington and Montgomery 1997; Gogus and Defne 2005; Recking 2009). Finally, the thickness of the geobags was used as the characteristic diameter in both studies; however, it is likely that the geobag thickness measured in Thompson et al. (2020b) was a maximum rather than a nominal thickness. Despite the differences between the two studies, the lower bound of the critical Shields parameter estimated by Thompson et al. (2020b) is at the lower end of the range of results from this study and lends support to the initial estimate provided by Thompson et al. (2020b).

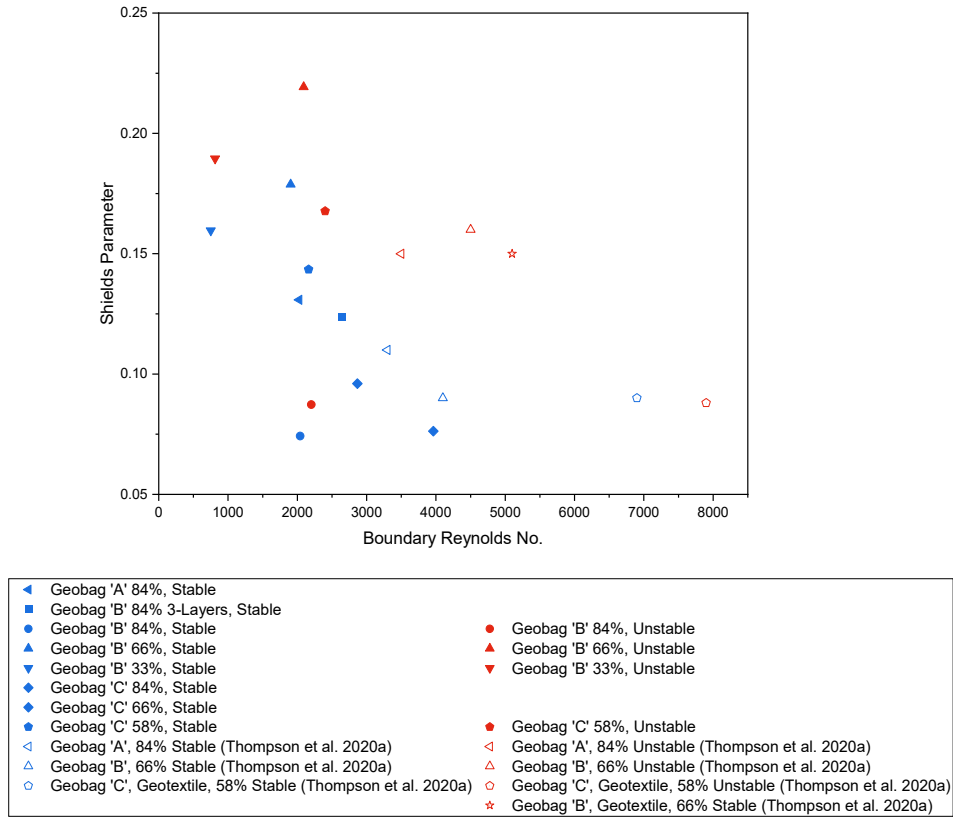


Figure 4-8: Comparison of Shields parameters between this study and the results from Thompson et al. (2020b) for the flat bed configuration.

In Chapter 3, a shape factor (see Eq. 4-6) was introduced to minimize the effects of bag shape, fill ratio, and flexibility on the critical Shields parameter. This shape factor was applied to the critical Shields parameters for the unstable conditions in this study, which is plotted in Figure 4-9.

$$SF_G = FR^3 \cdot \phi^{0.6} \cdot \left(\frac{a+b}{2c}\right) \cdot \left(\frac{V}{abc}\right)^{\frac{1}{3}} \quad \text{Eq. 4-6}$$

Where,  $SF_G$  is the geobag shape factor, FR is the fill ratio of the geobag (i.e., 54 %, 69 % or 84 %),  $\phi$  is the dimensionless angle of flexibility,  $a$  is the width of the geobag,  $b$  is the nominal

thickness of the geobag,  $c$  is the geobag length and  $V$  is the average measured volume of the geobag.

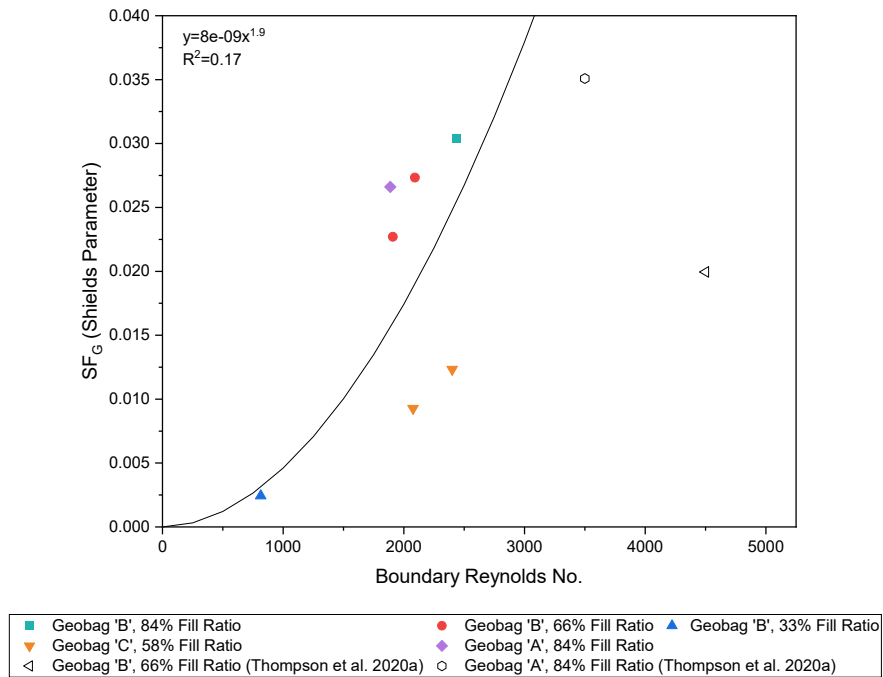


Figure 4-9: Relationship between Shields parameter, corrected for the shape factor, with the boundary Reynolds number for unstable conditions.

With the applied shape factor, a clearer trend is observed between the Shields parameter and boundary Reynolds number, though with a relatively weak correlation ( $R^2 = 0.17$ ). If the relative length and volume terms are omitted from the shape factor, and the fill ratio and angle of flexibility re-calibrated, the trend obtains a better fit (see Figure 4-10,  $R^2 = 0.52$ ). This suggests that the applicability of design sizing formulas could be improved by simply including the angle of flexibility and the fill ratio. Existing design formulas were therefore modified to include the fill ratio and angle of flexibility terms in the proceeding sections to improve their applicability for geobags.

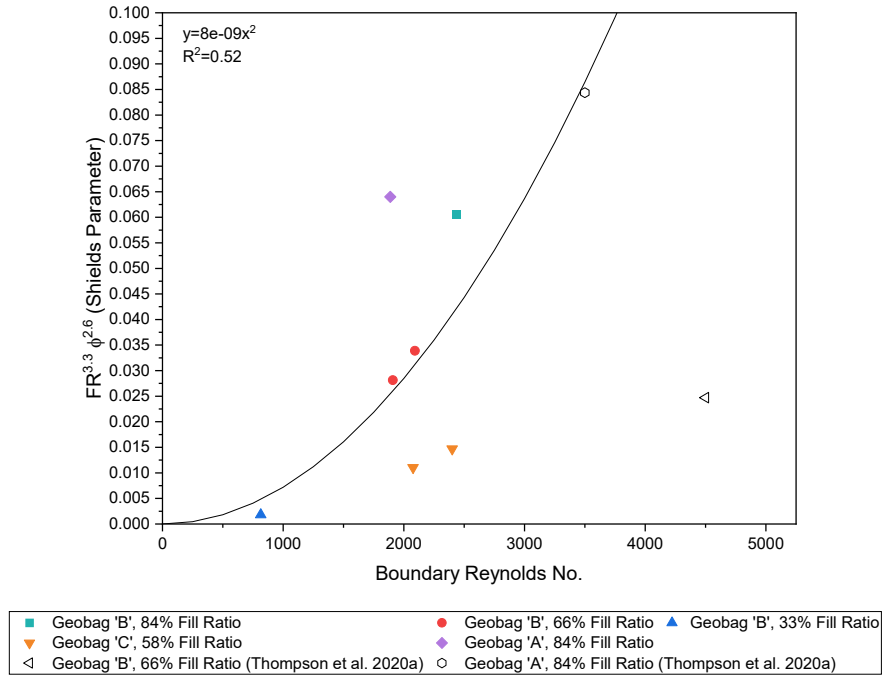


Figure 4-10: Relationship between critical Shields parameter, corrected with a modified shape factor ( $SF_G = FR^{3.3} \phi^{2.6}$ ), and the boundary Reynolds number for unstable conditions.

### 4.3.3 USACE Design Formula

The USACE formula was modified to incorporate the fill ratio and angle of flexibility due to their importance on geobag stability.

$$\frac{t}{y} = S_F C_S C_V C_T \frac{(FR)^c}{(\phi)^d} \left[ \left( \frac{\rho_w}{\rho_s - \rho_w} \right)^{0.5} \left( \frac{V_{cr}}{\sqrt{K_S g y}} \right) \right]^{2.5} \quad \text{Eq. 4-7}$$

where,  $FR$  is the fill ratio of the geobag and is raised to a power  $c$ ;  $\phi$  is the dimensionless angle of flexibility with respect to the 125 kg prototype size and is raised to a power  $d$ .  $c$  and  $d$  were calibrated using the data from this study and Thompson et al. (2020a) for the flat bed case (Figure 4-11) and the 1V:2H slope bed case (Figure 4-12), respectively. The safety factor ( $S_F$ ), vertical velocity distribution coefficient ( $C_V$ ), and the thickness coefficient ( $C_T$ ) were set to 1.1,

1.0 and 1.0, respectively, as recommended by USACE (1994). The modified USACE formula was compared to the original formula in both figures. Note that the curves in the figures represent the original or modified USACE formula. Ideally, the unstable conditions would fall below the line and the stable conditions above the line. The stable conditions correspond to the velocity set-point 0.19 m/s below the failure velocity.

As previously mentioned, the reported thickness of the geobags tested in Thompson et al. (2020a) likely corresponds to a maximum rather than a nominal thickness. To ensure the design formula predicts consistent sizes for the data from both this study and Thompson et al. (2020a), the thickness data from Thompson et al. (2020a) was converted to a nominal thickness. The geobag dimensions and mass of the geobags from Thompson et al. (2020a) are equal to the dimensions and mass of Geobag ‘A’ with an 84% fill ratio, Geobag ‘B’ with a 66% fill ratio, and Geobag ‘C’ with a 58% fill ratio. Therefore, the nominal thickness was assumed to be the same for the corresponding geobags.

For the flat bed series,  $FR$  was raised to the power of 0.1 and  $\phi$  was raised to the power of 0.2. For all geobags from this study, a single stability coefficient of  $C_S = 0.06$  can be used to describe the flat bed series using the modified USACE formula. The results from Thompson et al. (2020a) are also well described by this formula and stability coefficient (see Figure 4-11). In Figure 4-11a, the original USACE formula with  $C_S = 0.06$  separates only three cases of the stable conditions, which reside above the line. The unstable conditions of the geobags from NHC (2010) are also poorly described by the USACE formula with  $C_S = 0.06$ . In contrast, the modified USACE formula separates more of the stable and unstable conditions, where eight of fourteen cases of the stable condition reside above the line, and all the unstable conditions reside below the line.

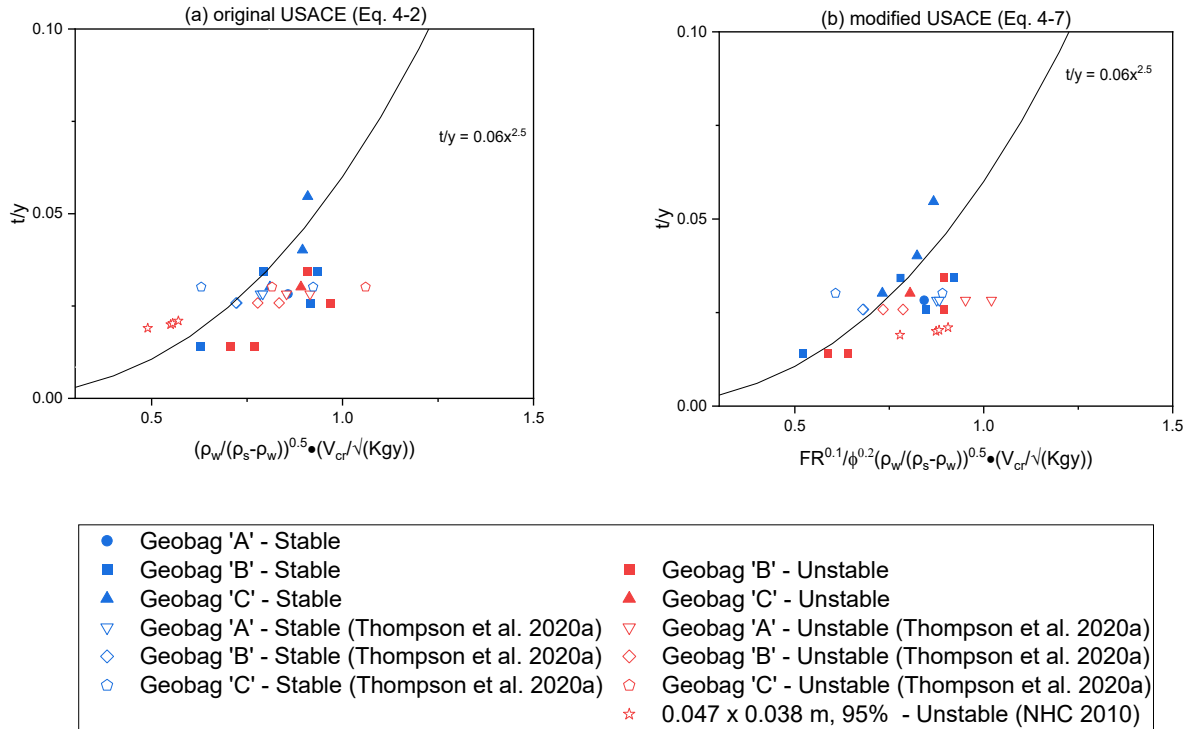


Figure 4-11: Application of the (a) original USACE formula, and (b) modified USACE formula with for the flat bed case.

For the sloped bed series, both  $FR$  and  $\phi$  were raised to the power of 0.1. For all geobags used in this study, and the geobags from Thompson et al. (2020a), a single stability coefficient of  $C_S = 0.05$  can be used to describe the sloped bed series with the modified USACE formula. However, most of the stable conditions from Thompson et al. (2020a) reside well below the line, suggesting that the formula would predict larger sizes than necessary for these cases. In Figure 4-12a, the stability coefficient of  $C_S = 0.05$  does not separate the stable and unstable cases well, as most of the cases reside below the line.

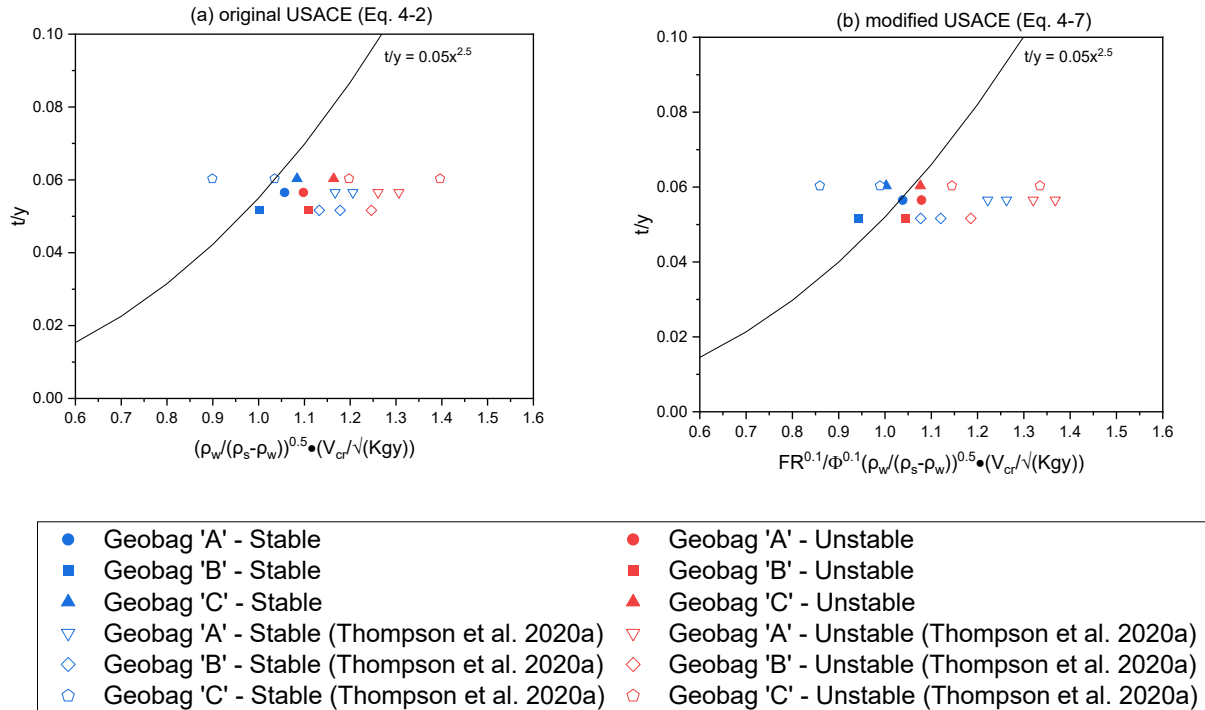


Figure 4-12: Application of the (a) original USACE formula, and (b) modified USACE formula with for the 1V:2H slope bed case.

In both flat and sloped bed series the modified formula performs better than the original formula by encompassing more cases and indicating a clearer separation between the unstable and stable conditions. However, the USACE formula generally does not describe the geobag stability well because it assumes that equal depth-averaged velocities with equal flow depths should have the same design characteristics. This assumption does not consider the near-bed velocities and shear stresses, which are crucial to the stability of the bed (e.g. Neil 1968; Buffington and Montgomery 1997). Furthermore, the modification to the USACE formula in Eq. 4-7 does not minimize the issue of predicting unrealistically small geobag sizes for sections of the Brahmaputra that are extremely deep (> 70 m).

#### 4.3.4 Pilarczyk Design Formula

The Pilarczyk formula was applied to the results from this study for both stable and unstable conditions (see Figure 4-13) to determine its applicability. Data from Thompson et al. (2020b)

was also plotted in Figure 4-13 for comparison. The original formula (Eq. 4-3) employs an effective diameter which is equal to the cube root of the volume. In this study, the effective diameter was taken as the nominal thickness of the geobag for consistency.

In Figure 4-13, the line represents the Pilarczyk formula, where the slope is the inverse Shields parameter. Similar to the USACE formula, the unstable conditions should lie below the line and stable conditions above the line. It is, however, more important that the unstable conditions lie below the line to ensure a safe design. Note that the stable conditions correspond to the velocity set-point 0.19 m/s below the failure velocity (or 0.50 m/s prototype velocity).

The Shields parameter that best fit the data from this study was 0.10, which is close to the lower bound of the Shields parameters for geobags determined from this study and Thompson et al. (2020b). Bezuijen and Vastenburg (2013) suggested using values of 0.035 for geobags < 0.3m<sup>3</sup> and 0.05 for larger geobags, which correspond to Shields parameters for riprap and loose placed blocks, respectively. If these values were used, the geobag sizes would be greatly overestimated.

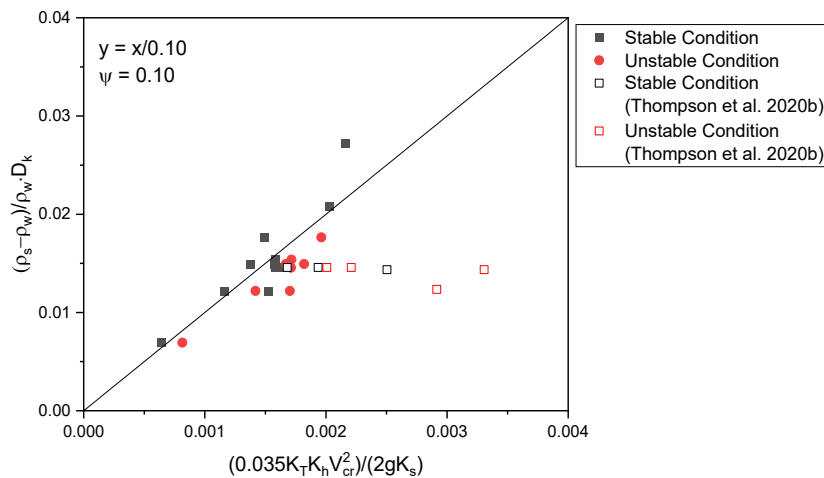


Figure 4-13: Application of the Pilarczyk formula on the results from this study, with a Shields parameter of 0.10. The slope of fitted line is the inverse of the Shields parameter.

There is a fair amount of scatter among the data from Thompson et al. (2020b), such that some stable cases lay well below the line. To improve the fit for both this study and Thompson et al. (2020b)'s study, a modification to the Pilarczyk formula was proposed:

$$\left(\frac{\rho_s - \rho_w}{\rho_w}\right) D_k \geq 0.035 \frac{\phi K_T K_h V_{cr}^2}{\psi K_s 2g\phi FR^{0.3}} \quad \text{Eq. 4-8}$$

The fill ratio (FR) and dimensionless angle of flexibility ( $\phi$ ) indirectly represents the flexibility and deformability of geobags, which has not been previously considered in the design formula. The introduction of these two terms improves the fit of the Pilarczyk formula, using a Shields parameter of 0.10, to the data from both this study and Thompson et al. (2020b) (see Figure 4-14). The modified Pilarczyk formula separates more stable cases and unstable cases than the original formula and reduces the potential for oversizing geobags.

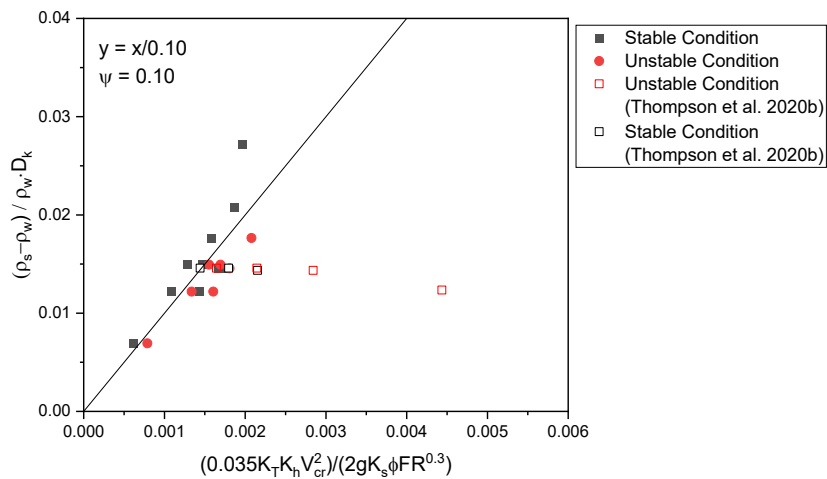


Figure 4-14: Application of the modified Pilarczyk formula on the results from this study, with a Shields parameter of 0.10.

#### 4.3.5 Applications in the Brahmaputra River

In the Brahmaputra River, surface velocities of 3.4 m/s were observed over stable revetment structures made of prototype 125 kg geobags (corresponding to the

model scale Geobag ‘A’ with 84% fill ratio in this study) (Thompson et al. 2020a). Failure velocities have not been observed for the prototype geobag; however, based on the results from the scaled model presented in this study a prototype failure velocity would be  $> 5.0$  m/s for the prototype 125 kg geobag filled to 84%. When the design formulas are applied to a typical prototype 125 kg geobag, they each predict different failure velocities (see Table 4-6). Note that the thickness of the prototype geobag was assumed to be 19 cm, according to Neill et al. (2008), and the flow depth 5 m (Thompson et al. 2020a).

Table 4-6: Application of design formulas to a prototype 125 kg geobag.

	USACE (Thompson et al. 2020a)	Modified USACE	Original Pilarczyk (Bezuijen and Vastenburger 2013)	Modified Pilarczyk
$\psi$ ; Shields Parameter	N/A	N/A	0.035	0.10
$V_{cr}$	3.7 m/s	7.2 m/s	3.25 m/s	5.50 m/s

In Table 4-6, both the original USACE and Pilarczyk formulas predict conservative estimates of the expected failure velocities: 3.7 m/s and 3.25 m/s, respectively. The modified formulas all predict a failure velocity  $> 5.0$  m/s, which coincides with the results from this study; however, as the failure velocity is not known for either the prototype or model geobags, it would be unwise to select any of the failure velocities from the modified equations in case they overestimate this value. Additionally, the depth-averaged velocities in the Brahmaputra only reach 5.1 m/s in locations such as the Padma Bridge (ADB 2010), yet these velocities are less likely in other reaches. The results from this study suggest that a 125 kg prototype geobag filled to 84% would remain stable in the Brahmaputra River, even at the Padma Bridge. As with any scaled physical model, there were practical limitations (i.e., upstream rock section to develop the flow, metal grid substrate to prevent geobags from sliding off plywood floor) which may impact the results.

It is therefore advisable to conduct further tests on a larger scale, perhaps in the field, to validate these results. At the Padma Bridge, 125 kg prototype geobags were installed as a filter element (ADB 2020). Diving explorations at this location may provide better insight as to the performance of the 125 kg geobags at high flow velocities in the field. Finally, it would be beneficial to test the model scale 125 kg geobags (Geobag ‘A’ with 84% fill ratio) until they reach incipient motion to improve the confidence in the modified formulas; however, reaching such velocities in the physical model scale would require a larger pump capacity which may be challenging to achieve. Alternatively, the data from this study may also be used to validate a CFD model, which can be used to investigate the performance of the modified design formulas under various flow conditions.

Another component to consider in the Brahmaputra River is the variation in depths, where in some locations the river depth can reach 70 m. It was previously identified that the original USACE formula recommends unreasonably small geobag sizes for such flow depths (Thompson et al. 2020a). This is because the depth term in the formula (Eq. 4-2) is inversely proportional to the size of the element (USACE 1994). The Pilarczyk formula does not indicate the element size is inversely proportional to the depth, and the flow depth is only considered in the depth factor,  $K_h$  (see Eq. 4-3). The depth factor in the formula translates the depth-averaged velocity into a near-bed velocity by assuming a logarithmic velocity profile for fully developed flow. At a 70 m flow depth, the geobag size predicted by the Pilarczyk formula is twice the size as predicted by the USACE formula. Although both sizes are still relatively small (less than 6 cm thickness), the Pilarczyk formula may predict more reasonable design sizes for deeper sections compared to the USACE formula.

Previous studies have recommended modifications to design formulas for geobag applications based on physical scaled models of the Brahmaputra River (i.e., Neill et al. 2008; NHC 2010; Thompson et al. 2020a). Table 4-7 summarizes the observed critical velocities, recommended design formulas and maximum design velocities from these studies. The model scale differs between the studies, where in both Neill et al. (2008) and NHC (2010) the model scale was 1:20 and in Thompson et al. (2020a) and this study, the model scale was 1:7. As previously mentioned, the smaller 1:20 model scale may not accurately depict the behaviour of the geobags due to the challenge of proportionally scaling the flexibility of the geobags. The geobag sizes and critical velocities were converted to the prototype scale to enable direct comparisons. Note that the characteristic diameter employed in the design formulas from Thompson et al. (2020a) and this study were the prototype scale of the nominal thickness for the corresponding geobag size, mass, and fill ratio. In Neill et al. (2008) and NHC (2010), the cube root of the geobag's volume was employed as the characteristic diameter, as per their recommendations. To ensure a stable design, the design velocity should be equal to or less than the observed critical velocity. To reduce the potential for oversizing geobags, the difference between the design velocity and the observed critical velocity should be relatively minimal. The modified design formulas presented in this study meet the criteria, and the modified Pilarczyk formula presents values closest to the observed critical velocities.

Table 4-7: Summary of recommended design formulas, observed critical velocities and design velocities for the prototype scale

Study	Design Formula	Geobag Size (Prototype)	Observed $V_{cr}$ (Prototype) [m/s]	Design $V_{cr}$ (Prototype) [m/s]
Neill et al. (2008)	USACE (Eq. 4-2) $C_s = 0.77$	125 kg 1.03 x 0.70 m	2.6 – 2.9	2.5
NHC (2010)	USACE (Eq. 4-2) $C_s = 0.31$	125 kg 1.03 x 0.70 m	4.2	3.5
Thompson et al. (2020a)	USACE (Eq. 4-2) $C_s = 0.07$	125 kg 1.03 x 0.70 m	4.8	3.8
		250 kg	4.8	2.7
	USACE (Eq. 4-2) $C_s = 0.15$	1.25 x 1.00 m 800 kg	4.6	2.9
		2.10 x 1.50 m		
This Study	USACE (Eq. 4-7) $C_s = 0.06$	125 kg 1.03 x 0.70 m	> 5.0	4.1
		250 kg 1.25 x 1.0 m	4.9	4.0
		800 kg 2.10 x 1.50 m	4.7	4.3
	Pilarczyk (Eq. 4-8) $\psi = 0.10$	125 kg 1.03 x 0.70 m	> 5.0	4.8
		250 kg 1.25 x 1.0 m	4.9	4.7
		800 kg 2.10 x 1.50 m	4.7	4.3

#### 4.4 Conclusion

A scaled physical model of geobag revetment structures was studied to evaluate stability and the applicability of existing design formulas. Three different geobag sizes were evaluated, representing typical field scale geobags used in erosion protection structures in the Brahmaputra River. The fill ratio and side slope were varied to determine their effects on geobag stability. The following conclusions were made:

- Geobags with higher fill ratios of sand (84%) tend to be more stable than geobags with lower fill ratios of sand, regardless of the bag dimensions.

- Geobags with higher fill ratios of sand and lower mass are generally more stable than geobags with lower fill ratios and higher mass. Also, geobags with higher fill ratios are more stable than geobags of equal mass with lower fill ratios. Therefore, fill ratio is more crucial to the geobags stability than the geobag's mass.
- Critical Shields parameters for geobags have been estimated to range from 0.09 to 0.22, supporting the initial estimate from previous studies.
- Modifications were made to both the USACE and Pilarczyk formulas to incorporate the geobag's angle of flexibility and fill ratio, which improved the prediction of stable geobag sizes. The nominal thickness was used as the characteristic diameter in the formulas, where the nominal thickness is the thickness of the geobag when the internal sand is evenly distributed.
- The Pilarczyk formula was also modified to incorporate an appropriate critical Shields parameter of 0.10 for geobags, based on the results of this study.
- Based on the results from this study, the modified Pilarczyk formula is recommended to size geobags as it considers the near bed velocities, the critical Shields parameter, and the flexibility of geobags. Furthermore, it is likely more suitable for extremely large flow depths that occur in the Brahmaputra River.

In future research studying geobag stability, it is advisable to determine critical shear stresses and thus critical Shields parameters to further validate the proposed critical Shields parameters, as this is an inherently statistical phenomenon. For practical purposes, it may be beneficial to investigate the geobag fill ratio at a larger scale to understand its upper limitations. Physical scaled models that can successfully fail all geobag sizes used in this test, especially the geobags with 84% fill ratio, should be conducted to further validate the proposed modified formulas. The

applicability of the design formulas for extremely large flow depths should be investigated more thoroughly, potentially by studying a scaled physical model to determine if smaller geobags are indeed stable at these conditions. The longevity of geobag stability should also be investigated in future studies, as the sand within geobags tends to consolidate after some time and natural wear and tear may impact the geobag stability. Finally, the results of this study can be used to validate a CFD model, which can then be applied to obtain a more comprehensive picture of the hydraulic forces acting on the bed under various flow conditions, as only three measurement locations were obtained in this study.

#### 4.5 References

ADB, 2002. *Report and Recommendation of the President to the Board of Directors on a Proposed Loan to the People's Republic of Bangladesh for the Jamuna-Meghna River Erosion Mitigation Project*, s.l.: ADB.

ADB, 2010. *Facility Administration Manual: India: Multitranches Financing Facility - Assam Integrated Flood and Riverbank Erosion Risk Management Investment Program*, s.l.: ADB.

ADB, 2014. *Environmental Impact Assessment: Bangladesh: Flood and Riverbank Erosion Risk Management Investment Program*, s.l.: ADB.

ADB, 2020. *Completion Report: Bangladesh: Padma Multipurpose Bridge Design Project*, s.l.: ADB.

Akter, A., Pender, G., Wright, G. & Crapper, M., 2013. Performance of a Geobag Revetment I: Quasi-Physical Modeling. *Journal of Hydraulic Engineering*, 139(8), pp. 865-876.

Bangladesh Water Development Board, 2010. *Guidelines for Riverbank Protection. Jamuna-Meghna River Erosion Protection Project*, Bangladesh: s.n.

Bezuijen, A. & Vastenburg, E., 2013. *Geosystems. Design Rules and Applications*. 1st ed. London: Taylor & Francis Group.

Biron, P. M., Robson, C., Lapointe, M. F. & Gaskin, S. J., 2004. Comparing different methods of bed shear stress estimates in simple and complex flow fields. *Earth Surface Processes and Landforms*, Volume 29, pp. 1403-1415.

Buffington, J. M. & Montgomery, D. R., 1997. A systematic analysis of eight decades of incipient motion studies, with special reference to gravel-bedded rivers. *Water Resources Research*, 33(8), pp. 1993-2029.

Chow, V. T., 1959. *Open-Channel Hydraulics*. 1st ed. Tokyo: McGraw-Hill Book Company.

- Gogus, M. & Defne, Z., 2005. Effect of Shape on Incipient Motion of Large Solitary Particles. *Journal of Hydraulic Engineering*, 131(1), pp. 38-45.
- Grune, J. et al., 2007. *Stability tests of geotextile sand containers for monopile scour protection*. San Diego, 30th. International Conference on Coastal Engineering (ICCE 2006).
- Heibaum, M., 2014. Geosynthetics for Waterways and Flood Protection Structures- Controlling the Interaction between Water and Soil. *Geotextiles and Geomembranes*, Volume 42, pp. 374-393.
- Heibaum, M., Oberhagemann, K., Faisal, M. & Haque, S., 2008. *Geotextile bags for sole permanent bank protection*. Edinburgh, 4th European Geosynthetics Conference.
- Khajenoori, L., Wright, G. & Crapper, M., 2021. Laboratory Investigation of Geobag Revetment Performance in Rivers. *Geosciences*, 11(304).
- Kim, S.-C., Friedrichs, C. T., Maa, P.-Y. & Wright, L. D., 2000. Estimating bottom stress in tidal boundary layer from acoustic doppler velocimeter data. *Journal of Hydraulic Engineering*, 126(6), pp. 399-406.
- Korkut, R. et al., 2007. Geobag Performance as Scour Countermeasure for Bridge Abutments. *Journal of Hydraulic Engineering*, 133(4), pp. 431-439.
- Neill, C., 1968. *A re-examination of the beginning of movement for coarse granular bed materials*, s.l.: Research Council of Alberta.
- Neill, C., Mannerstrom, M. & Azad, A. K., 2008. *Model tests on geobags for erosion protection*. Tokyo, Fourth International Conference on Scour and Erosion.
- Nikora, V. & Goring, D., 2000. Flow turbulence over fixed and weakly mobile gravel beds. *Journal of Hydraulic Engineering*, 126(9), pp. 679-690.
- Nortek, 2018. *The Comprehensive Manual for Velocimeters*, s.l.: s.n.
- Northwest Hydraulics Consultants (NHC), 2010. *Padma Multipurpose Bridge Design Project RT23 Geobag Flume Model Study*. s.l.:Prepared for Maunsell/AECOM and Bangladesh Bridge Authority.
- Oberhagemann, K. & Hossain, M., 2011. Geotextile bag revetments for large rivers in Bangladesh. *Geotextiles and Geomembranes*, Volume 29, pp. 402-414.
- Pilarczyk, K., 2000. *Geosynthetics and Geosystems in Hydraulic and Coastal Engineering*. Rotterdam: A. A. Balkema.
- Pilarczyk, K. W., 1991. *Coastal Protection Short Course Rijkswaterstaat*. Delft: Road and Hydraulic Engineering Division Van der Burghweg.
- Recio, J. & Oumeraci, H., 2009. Process based stability formulae for coastal structures made of geotextile sand containers. *Coastal Engineering*, Volume 56, pp. 632-658.

- Recking, A., 2009. Theoretical development on the effects of changing flow hydraulics. *Water Resources Research*, 45(W04401), pp. 1-16.
- Schlichting, H. & Gersten, K., 2000. *Boundary-Layer Theory*. 8 ed. Berlin: Springer-Verlag.
- Shields, A., 1936. *Application of similarity principles and turbulence research to bed-load movement: English translation*, Pasadena: California Institute of Technology.
- Soulsby, R. L., 1983. The Bottom Boundary Layer of Shelf Seas. In: J. B., ed. *Physical Oceanography of Coastla and Shelf Areas*. Amsterdam: Elsevier, pp. 189-266.
- Thompson, A., Oberhagemann, K. & She, Y., 2020a. Geobag stability for riverbank erosion protection structures: Physical model study. *Geotextiles and Geomembranes*, 48(1), pp. 110-119.
- Thompson, A., She, Y. & Oberhagemann, K., 2020b. Geobag stability for riverbank erosion protection structures: Numerical model study. *Geotextiles and Geomembranes*, 48(5), pp. 703-712.
- USACE, 1994. *Hydraulic Design of Flood Control Channels*, Washington: U.S. Army Corps of Engineers.
- White, K., She, Y. & Zhang, W., Submitted. A Comparison of Shear Stress Estimation Methods for a Single Geobag on a Rough Bed. *Geotextiles and Geomembranes*.
- Yang, S., Shu, Y. & Yang, X., 2008. Flume experiment and numerical analysis for bank reinforcement with geocontainer. In: *Geosynthetics in Civil and Environmental Engineering*. Berlin, Germany: Springer, pp. 639-636.
- Zellweger, H., 2007. *Geotextile bags for river erosion control in Bangladesh*, Zürich: Swiss Federal Institute of Technology.
- Zhang, L. et al., 2020. Comparison of Methods for Bed Shear Stress Estimation in Complex Flow Field of Bend. *Water*, 2753(12), pp. 1-16.
- Zhu, L. et al., 2004. Settling Distance and Incipient Motion of Sandbags in Open Channel Flows. *Journal of Waterway, Port, Coastal and Ocean Engineering*, 130(2), pp. 98-103.

## 5 Conclusions and Future Research

Geobags used as primary elements in erosion protection structures provide a cost-effective solution to riverbank/bed stability. Current methods result in the potential for over sizing, creating unnecessary labor and costs. There are opportunities to improve the design sizing methodologies for geobags as current methods do not consider the unique properties of geobags such as their deformability and flexibility. This thesis investigated geobag stability in physical scaled models. Initially, various methods to estimating critical shear stresses were investigated for geobag applications. Then, the stability of a single geobag was studied to assess the influences of geobag shape, fill ratio, bag material and bed configuration. Finally, a uniform bed of geobags was tested to simulate erosion protection structures and analyze their stability. Fill ratios, bag dimensions and bed configurations were varied to evaluate their impact on the geobag stability. Critical Shields parameters were estimated for both the study of the single geobag and the full bed. Finally, pre-existing design sizing formulas were modified to improve their applicability for geobags. The detailed conclusions of this thesis are provided in Chapters 2, 3 and 4 while a summary of the general conclusions is provided below.

The turbulent kinetic energy (TKE) local bed shear stress estimation method best represented the expected shear stresses for the complex flow condition of a single geobag on a rough bed, compared to other methods (i.e., universal law of the wall, Patel, Reynolds stress, TKE  $w'$  methods). The TKE method was therefore used to estimate the critical bed shear stress of geobags in both the single bag and full bed experiments of Chapters 3 and 4. For future research, the proportionality constants used in the TKE methods should be calibrated for varying channel geometries in fluvial applications, such that the TKE methods may be more widely applied.

In the single bag experiments, the geobag stability was quantified by both a critical Shields parameter and depth-averaged velocity. A shape factor was proposed to assess the relative influence of geobag characteristics on the stability. The geobag stability was affected by the fill ratio, geobag shape, bag material, and bed configuration. Cloth bags failed at a higher velocity than geotextile bags, by an average of 0.45 m/s, which was attributed to the different flexibility of the two bag materials. Overall, geobags with a higher fill ratio and more flexible bag material (i.e., cloth) were most stable.

In the full bed experiments, geobags with higher fill ratios and smaller masses generally resulted in better stability. Geobags on the 1V:2H sloped bed experienced lower stability than on the flat bed, which was attributed to additional gravitational forces and higher relative roughness. The critical Shields parameters were estimated to range between 0.09 and 0.22, supporting an initial lower bound estimate by Thompson et al. (2020b) of 0.09. The shape factor presented in Chapter 3 was evaluated for the full bed to assess its potential application in design sizing formulas. Pre-existing design sizing formulas were then modified to include the geobag sand fill ratio and angle of flexibility to improve their applicability for geobags. A modified Pilarczyk formula that uses a critical Shields parameter of 0.10 was recommended.

Limitations and sources of uncertainty to this study are summarized below:

- The instrumentation used to collect relevant data have sources of uncertainty, which are explained in detail in Chapter 2. The Pitot-Tube was limited by its inability to capture the effects of turbulence, and the ADV has some level of uncertainty for near-bed velocity measurements as demonstrated by the difference between the Pitot-Tube and ADV measurements.

- The bed substrate used in the experiments presented in Chapter 2, 3 and 4 varied and did not match the sand bed substrate that would be present in the field. This was due to practical limitations, including material availability and flume limitations. For example, in Chapter 3, the geobags did not undergo incipient motion when placed on the pea-gravel substrate; therefore, the asphalt substrate was used.
- The experiments were limited by the maximum achievable flow velocities, such that some geobag sizes and masses were unable to achieve incipient motion.
- In Chapter 4, a rock section was used to help develop the flow for the geobag test-section. This is not representative of erosion protection structures in the field, as there are typically no riprap sections upstream of the geobag revetments. Therefore, there is some uncertainty in how the upstream section of the geobag revetment would perform under the subjected flow conditions.
- The same geobag size, fill ratio and shape experienced incipient motion at different flow velocities, suggesting that consistent initial conditions still have variable critical conditions. This is expected as the critical Shields parameter is described as inherently statistical, and as such there will be a level of uncertainty regarding the critical condition.

Future research considerations are presented below:

- The results presented in Chapter 3 and 4 could be used to validate computational fluid dynamics (CFD) models which can provide more insight into the flow fields and forces acting on geobags on both the flat and 1V:2H sloped beds. Specifically, the CFD model would be able to quantitatively model the impacts of different bed roughness, transient flow conditions, different flow depths and/or channel geometries on the stability of erosion protection structures.

- As the critical Shields parameters are inherently statistical, future geobag stability studies should estimate critical Shields parameters to lend higher confidence to the values presented herein.
- Future geobag stability studies should consider studying the impact of flow depth on stability, to assess the application of design sizing formulas at large flow depths. The Brahmaputra River experiences significant flow depths (70 m), and current design sizing formulas estimate extremely small geobag sizes for such flow depths.
- It is suggested that future studies consider varying channel geometries and the impact of secondary and mean flows on geobag stability, for potential applications in narrow, meandering rivers. Additionally, the impact of different flow conditions (i.e., steady state flow vs transient flow) should be studied to assess the geobag stability and applicability of current design methods.
- The impacts of flooding conditions should be studied in the future to assess the geobag revetment stability, and suitability of the modified design formulas for such applications.
- In future studies, the stability of varying geobag revetment slopes should be investigated as there have been conflicting observations, where in some cases geobags are more stable on a flat bed while in others they are more stable on a slope. Furthermore, the number of layers and placement methods for geobag revetment slopes should be varied to consider the impact on stability while mimicking the different stages of revetment construction.
- The studies presented in this thesis employed fixed, rough substrates in the physical models (i.e., asphalt, metal grids). Different sub-bed materials, such as sand and gravel, should be evaluated in future studies to evaluate their impact on geobag revetment

stability. This would also allow evaluation of sand winnowing and the effect of surface coverage on the revetment stability.

- As higher fill ratios are directly related to better stability, the method of filling geobags in the field should be evaluated as this is a manual process. Future studies may also consider the impact of sand consolidation and natural wear and tear on geobag stability.
- Diving explorations in the Brahmaputra River at select locations may help to validate the results presented in Chapter 4, where some of the geobag sizes did not undergo incipient motion due to flume constraints.
- Finally, the definition of incipient motion should be revisited because it is unclear if losing 5% of the geobags in a revetment structure indicates structural failure.

## References

- Ackerman, J. D. & Hoover, T. M., 2001. Measurement of local bed shear stress in streams using a Preston-static tube. *Limnology and Oceanography*, 46(8), pp. 2080-2087.
- ADB, 2002. *Report and Recommendation of the President to the Board of Directors on a Proposed Loan to the People's Republic of Bangladesh for the Jamuna-Meghna River Erosion Mitigation Project*, s.l.: ADB.
- ADB, 2009. *Environmental Assessment Report: India: Assam Integrated Flood and Riverbank Erosion Risk Management Investment Program*, s.l.: ADB.
- ADB, 2010. *Environmental Assessment Report: BAN: Padma Multipurpose Bridge Project*, s.l.: ADB.
- ADB, 2010. *Facility Administration Manual: India: Multitranches Financing Facility - Assam Integrated Flood and Riverbank Erosion Risk Management Investment Program*, s.l.: ADB.
- ADB, 2014. *Environmental Impact Assessment: Bangladesh: Flood and Riverbank Erosion Risk Management Investment Program*, s.l.: ADB.
- ADB, 2020. *Completion Report: Bangladesh: Padma Multipurpose Bridge Design Project*, s.l.: ADB.
- Akter, A., Pender, G., Wright, G. & Crapper, M., 2013. Performance of a Geobag Revetment I: Quasi-Physical Modeling. *Journal of Hydraulic Engineering*, 139(8), pp. 865-876.
- Bangladesh Water Development Board, 2010. *Guidelines for Riverbank Protection. Jamuna-Meghna River Erosion Protection Project*, Bangladesh: s.n.
- Bezuijen, A. & Vastenburg, E., 2013. *Geosystems. Design Rules and Applications*. 1st ed. London: Taylor & Francis Group.
- Biron, P. M., Robson, C., Lapointe, M. F. & Gaskin, S. J., 2004. Comparing different methods of bed shear stress estimates in simple and complex flow fields. *Earth Surface Processes and Landforms*, Volume 29, pp. 1403-1415.
- Buffington, J. M. & Montgomery, D. R., 1997. A systematic analysis of eight decades of incipient motion studies, with special reference to gravel-bedded rivers. *Water Resources Research*, 33(8), pp. 1993-2029.
- Chow, V. T., 1959. *Open-Channel Hydraulics*. 1st ed. Tokyo: McGraw-Hill Book Company.
- Dey, S. et al., 2011. Wall-wake flows downstream of a sphere placed on a rough wall. *Journal of Hydraulic Engineering*, 137(10), pp. 1173-1189.
- Dietrich, W. E. & Whiting, P., 1989. Boundary shear stress and sediment transport in river meanders of sand and gravel. *Water Resources Monograph*, Volume 12, pp. 1 - 50.

- Fernandez, R., Best, J. & Lopez, F., 2006. Mean flow, turbulence structure, and bed form superimposition across the ripple-dune transition. *Water Resources Research*, Volume 42, pp. 1-17.
- Garcia, C. M., Cantero, M. I., Nino, Y. & Garcia, M. H., 2005. Turbulence measurements with acoustic doppler velocimeters. *Journal of Hydraulic Engineering*, 131(12), pp. 1062-1073.
- GISGeography, 2022. *Bangladesh Map*. [Online]  
Available at: <https://gisgeography.com/bangladesh-map/>  
[Accessed 2022].
- Gordon, L. & Cox, J., 2000. *Acoustic doppler velocimeter performance in a laboratory flume*, San Diego, California: NortekUSA.
- Grune, J. et al., 2007. *Stability tests of geotextile sand containers for monopile scour protection*. San Diego, 30th. International Conference on Coastal Engineering (ICCE 2006).
- Guo, J., 2015. Sidewall and non-uniformity corrections for flume experiments. *Journal of Hydraulic Research*, 53(2), pp. 218-229.
- Guo, J., 2017. Exact Procedure for Einstein-Johnson's Sidewall Correction in Open Channel Flow. *Journal of Hydraulic Engineering*, 143(4), pp. 1-6.
- Guo, J. & Julien, P. Y., 2005. Shear Stress in Smooth Rectangular Open-Channel Flows. *Journal of Hydraulic Engineering*, 131(1), pp. 30-37.
- Heibaum, M., 2014. Geosynthetics for Waterways and Flood Protection Structures- Controlling the Interaction between Water and Soil. *Geotextiles and Geomembranes*, Volume 42, pp. 374-393.
- Heibaum, M., Oberhagemann, K., Faisal, M. & Haque, S., 2008. *Geotextile bags for sole permanent bank protection*. Edinburgh, 4th European Geosynthetics Conference.
- Henderson, F. M., 1966. *Open Channel Flow*. New York: Macmillan.
- Hoover, T. M. & Ackerman, J. D., 2004. Near-bed hydrodynamic measurements above boulders in shallow torrential streams: Implications for stream biota. *Journal of Environmental Engineering*, Volume 3, pp. 365-378.
- Hornsey, W. P., Carley, J. T., Coghlan, I. R. & Cox, R. J., 2011. Geotextile sand container shoreline protection systems: Design and application. *Geotextiles and Geomembranes*, Volume 29, pp. 425 - 439.
- Khajenoori, L., Wright, G. & Crapper, M., 2021. Laboratory Investigation of Geobag Revetment Performance in Rivers. *Geosciences*, 11(304).
- Kim, S.-C., Friedrichs, C. T., Maa, P.-Y. & Wright, L. D., 2000. Estimating bottom stress in tidal boundary layer from acoustic doppler velocimeter data. *Journal of Hydraulic Engineering*, 126(6), pp. 399-406.

- Korkut, R. et al., 2007. Geobag Performance as Scour Countermeasure for Bridge Abutments. *Journal of Hydraulic Engineering*, 133(4), pp. 431-439.
- Maynard, S., 1988. *Stable Riprap Size for Open Channel Flows*, Washington: U.S. Army Corps of Engineers.
- McLelland, S. J. & Nicholas, A. P., 2000. A new method for evaluating errors in high-frequency ADV measurements. *Hydrological Processes*, Volume 14, pp. 351-366.
- Moeini, M., Kazemi, M., Khorsandi, B. & Mydlarski, L., 2019. *A laboratory study of the effect of acoustic doppler velocimeter sampling frequency and sampling volume on measurements*. Laval, CSCE Annual Conference.
- Moreira, A., Vieira, C., Neves, L. & Lopes, M., 2016. Assessment of friction properties at geotextile encapsulated-sand systems' interfaces used for coastal protection. *Geotextiles and Geomembranes*, 44(3), pp. 278-286.
- Mueller, E. R., Pitlick, J. & Nelson, J., 2005. Variation in the reference Shields stress for bed load transport in gravel-bed streams and rivers. *Water Resources Research*, Volume 41.
- Neill, C., 1968. *A re-examination of the beginning of movement for coarse granular bed materials*, s.l.: Research Council of Alberta.
- Neill, C., Mannerstrom, M. & Azad, A. K., 2008. *Model tests on geobags for erosion protection*. Tokyo, Fourth International Conference on Scour and Erosion.
- Nezu, I. & Nakagawa, H., 1993. *Turbulence in Open-Channel Flows*. 1 ed. Rotterdam: A.A.Balkema.
- NHC, 2010. *Padma Multipurpose Bridge Design Project RT23 Geobag Flume Model Study*. s.l.:Prepared for Maunsell/AECOM and Bangladesh Bridge Authority.
- Nikora, V. & Goring, D., 2000. Flow turbulence over fixed and weakly mobile gravel beds. *Journal of Hydraulic Engineering*, 126(9), pp. 679-690.
- Nikora, V. I. & Goring, D. G., 1998. ADV measurements of turbulence: Can we improve their interpretation?. *Journal of Hydraulic Engineering*, 124(6), pp. 630-634.
- Nortek, 2018. *The Comprehensive Manual for Velocimeters*, s.l.: s.n.
- Oberhagemann, K. & Hossain, M., 2011. Geotextile bag revetments for large rivers in Bangladesh. *Geotextiles and Geomembranes*, Volume 29, pp. 402-414.
- Oberhagemann, K., Stevens, M., Haque, S. & Faisal, M., 2006. *Geobags for Riverbank Protection*:. Amsterdam, Proceedings 3rd International Conference on Scour and Erosion (ICSE-3).
- Papanicolaou, A. N. et al., 2012. Effects of a fully submerged boulder within a boulder array on the mean and turbulent flow fields: Implications to bedload transport. *Acta Geophysica*, 60(6), pp. 1502-1546.

- Patel, V. C., 1965. Calibration of the Preston tube and limitations on its use in pressure gradients. *Journal of Fluid Mechanics*, 23(1), pp. 185-208.
- Pilarczyk, K., 2000. *Geosynthetics and Geosystems in Hydraulic and Coastal Engineering*. Rotterdam: A. A. Balkema.
- Pilarczyk, K. W., 1990. *Coastal Protection*. Rotterdam: A.A. Balkema.
- Pilarczyk, K. W., 1991. *Coastal Protection Short Course Rijkswaterstaat*. Delft: Road and Hydraulic Engineering Division Van der Burghweg.
- Pokrajac, D. et al., 2006. On the definition of the shear velocity in rough bed open channel flows. *Proceedings of the International Conference of Fluvial Hydraulics - River Flow*, pp. 89-98.
- Preston, J. H., 1954. The determination of turbulent skin friction by means of Pitot tubes. *Journal of the Royal Aeronautical Society*, Volume 58, pp. 109-121.
- Recio, J. & Oumeraci, H., 2009. Process based stability formulae for coastal structures made of geotextile sand containers. *Coastal Engineering*, Volume 56, pp. 632-658.
- Recking, A., 2009. Theoretical development on the effects of changing flow hydraulics. *Water Resources Research*, 45(W04401), pp. 1-16.
- Schindler, R. J. & Robert, A., 2005. Flow and turbulence structure across the ripple–dune transition: an experiment under mobile bed conditions. *Sedimentology*, Volume 52, pp. 627-649.
- Schindler, R. & Robert, A., 2004. Suspended sediment concentration and the ripple - dune transition. *Hydrological Processes*, Volume 18, pp. 3215-3227.
- Schlichting, H. & Gersten, K., 2000. *Boundary-Layer Theory*. 8 ed. Berlin: Springer-Verlag.
- Schvidchenko, A. & Pender, G., 2000. Flume study of the effect of relative depth on incipient motion of coarse uniform sediments. *Water Resources Research*, 36(2), pp. 619-628.
- Shields, A., 1936. *Application of similarity principles and turbulence research to bed-load movement: English translation*, Pasadena: California Institute of Technology.
- Soulsby, R. L., 1983. The Bottom Boundary Layer of Shelf Seas. In: J. B, ed. *Physical Oceanography of Coastla and Shelf Areas*. Amsterdam: Elsevier, pp. 189-266.
- Sutardi & Ching, C. Y., 2001. Effect of tube diameter on Preston tube calibration curves for the measurement of wall shear stress. *Experimental Thermal and Fluid Sciences*, Volume 24, pp. 93-97.
- Thompson, A., Oberhagemann, K. & She, Y., 2020a. Geobag stability for riverbank erosion protection structures: Physical model study. *Geotextiles and Geomembranes*, 48(1), pp. 110-119.
- Thompson, A., She, Y. & Oberhagemann, K., 2020b. Geobag stability for riverbank erosion protection structures: Numerical model study. *Geotextiles and Geomembranes*, 48(5), pp. 703-712.

- USACE, 1994. *Hydraulic Design of Flood Control Channels*, Washington: U.S. Army Corps of Engineers.
- Voulgaris, G. & Trowbridge, J. H., 1997. Evaluation of the Acoustic Doppler Velocimeter (ADV) for Turbulence Measurements. *Journal of Atmospheric and Oceanic Technology*, Volume 15, pp. 272-289.
- White, F. M., 1999. Chapter 7 Flow Past Immersed Bodies. In: J. P. Holman & J. Lloyd, eds. *Fluid Mechanics*. 4th ed. s.l.:McGraw-Hill, pp. 427 - 494.
- White, K., She, Y. & Zhang, W., Submitted. A Comparison of Shear Stress Estimation Methods for a Single Geobag on a Rough Bed. *Geotextiles and Geomembranes*.
- Wilcock, P. R., 1996. Estimating local bed shear stress from velocity observations. *Water Resources Research*, 32(11), pp. 3361-3366.
- Zellweger, H., 2007. *Geotextile bags for river erosion control in Bangladesh*, Zürich: Swiss Federal Institute of Technology.
- Zhang, L. et al., 2020. Comparison of Methods for Bed Shear Stress Estimation in Complex Flow Field of Bend. *Water*, 2753(12), pp. 1-16.
- Zhu, L. et al., 2004. Settling Distance and Incipient Motion of Sandbags in Open Channel Flows. *Journal of Waterway, Port, Coastal and Ocean Engineering*, 130(2), pp. 98-103.
- Zimmermann, A., Church, M. & Hassan, M., 2010. Step-pool stability: Testing the jammed state hypothesis. *Journal of Geophysical Research*, Volume 115.